Synthesis and post-treatment of hard coatings for cemented carbide cutting tools

Dipl.-Ing. Nina Schalk

being a thesis in partial fulfilment of the requirements for the degree of a

Doctor of Montanistic Sciences (Dr. mont.)

at the Montanuniversität Leoben

Leoben, July 2013

Financial support by the Austrian Federal Government (in particular from the Bundesministerium für Verkehr, Innovation und Technologie and the Bundesministerium für Wirtschaft, Familie und Jugend) and the Styrian Provincial Government, represented by Österreichische Forschungsförderungsgesellschaft mbH and by Steirische Wirtschaftsförderungsgesellschaft mbH, within the research activities of the K2 Competence Centre on "Integrated Research in Materials, Processing and Product Engineering", operated by the Materials Center Leoben Forschung GmbH in the framework of the Austrian COMET Competence Centre Programme, is gratefully acknowledged.

Affidavit

I declare in lieu of oath, that I wrote this thesis and performed the associated research myself, using only literature cited in this volume.

Leoben, July 2013

Acknowledgments

My sincerest gratitude is due to Prof. Dr. Christian Mitterer for the possibility to compose this thesis at the Chair for Functional Materials and Material Systems, for the confidence he places in me, for his supervision, advice, guidance and patience. *Thank you for letting me be part of your group!*

I would also like to thank ao. Prof. Dr. Jozef Keckes for co-supervising this work and for the valuable comments contributing to this thesis.

I am grateful to ao. Prof. Dr. Reinhold Ebner and to Dr. Richard Schanner, managing directors of the Materials Center Leoben (MCL), for giving me the opportunity to carry out my thesis within an MCL project. I am also thankful to the MCL staff and the co-workers for their support. Special thanks to Bernhard Sartory for his exceptional work on the REM-FIB.

I would like to express my gratitude to MSc Marianne Penoy and DI Claude Michotte from CERATIZIT Luxembourg and to DI Christoph Czettl from CERATIZIT Austria for their experimental and analytical support and the fruitful discussions. *Thank you!*

I appreciate the contribution of Dr. Ilse Letofsky-Papst from the Research Institute for Electron Microscopy of the Graz University of Technology. *You did great work on the TEM!*

Special thanks to my co-workers, DI (FH) Angelika Riedl, Marina Gruber, Maximilian Siller and Christian Saringer. *Your work is an important part of this thesis!*

I also would like to express my sincerest gratitude to my colleagues of the “Thin Film Group” for valuable discussions in all matters. Thanks to my colleagues DI Doris Sonnleitner and DI Stephan Grasser for cheering me up during one or two entertaining coffee breaks. Special thanks go to my office mate DI Michael Tkadletz for the pleasurable working atmosphere. *Sharing an office with you was great fun!*

I am deeply grateful to my parents for their love and support.

Furthermore, I would like to say “Thank you!” to my brother Patrick, just for being the person he is.

Last but not least, I want to thank the most important person in my life, my husband Peter. *Thank you for your countless encouragements, the support in every possible way, the trust you place in me, your endless patience and above all, for your love!*

Contents

1. Introduction

Coated cemented carbide cutting tools are widely used for different machining applications. During the last decades, economical demands and environmental considerations of the machining industry for still higher cutting speeds and feed rates as well as for the reduction of the use of harmful coolants and lubricants have promoted significant progress in the coating industry [1-3]. The synthesis of these coatings is realized via condensation from the vapor phase by either physical vapor deposition (PVD) or chemical vapor deposition (CVD) techniques [4]. Using PVD, the vapor is generated from solid sources utilizing physical methods, while for CVD the vapor is provided by gaseous precursors, which are introduced into the deposition chamber [5].

$Ti_{1-x}Al_xN$ is an important representative for wear resistant coatings synthesized by PVD. The properties of $Ti_{1-x}Al_xN$ can be further enhanced by the addition of different alloying elements [2, 6, 7-11]. Alloying with e.g. Ta has beneficial effects on the mechanical and tribological properties of the coatings and increases the oxidation resistance compared to $Ti_{1-x}Al_xN$ [2, 7, 8].

Typical coatings grown by CVD are e.g. α- and κ-Al_2O_3. Al_2O_3 exhibits high temperature hardness, chemical inertness and low thermal conductivity, which makes it a very suitable coating for cutting tools. It has several crystallographic modifications, where the metastable orthorhombic κ-phase and the stable rhombohedral α-phase are predominating for coatings on cutting tools [12-14].

However, there is further potential for improvement of these hard coatings by applying suitable post-deposition treatments. These treatments can be divided into two major groups; *(i)* mechanical and *(ii)* thermal methods. Using mechanical methods, like wet- or dry-blasting, not only an improvement of the surface topography can be achieved but also tailoring of the residual stresses is possible [15]. Thermal treatments can be used to improve the microstructure and to modify the surface in order to reduce the friction between work-piece and coating.

The present work comprises an attempt to optimize both, the deposition process and the hard coatings. In order to make coating synthesis efficient, targets with high sputtering or evaporations rates are required. Thus, the influence of two different sputter target types (i.e. powder metallurgically produced compound targets and cast mosaic targets) on the deposition process as well as on the structure and properties of the obtained coatings was investigated in detail. For further optimization of the sputter deposited $Ti_{1-x}Al_xN$ coatings, a series of coatings with stresses ranging from tensile to compressive was synthesized using different bias voltages. The samples were vacuum annealed and the influence of the residual

stresses and the grain size on the spinodal decomposition of the metastable coatings was illuminated. Coating optimization by post-treatment was also investigated on other PVD and CVD hard coatings. Arc evaporated TiAlTaN coatings were thermally post-treated in methane in order to improve the friction behavior, while the effect of dry-blasting using different blasting materials and pressures was investigated on α- and κ-Al_2O_3 CVD hard coatings.

2. Coating Deposition

2.1. Physical Vapor Deposition

Physical vapor deposition (PVD) processes can basically be described by three main steps; *(i)* Formation of vapor, *(ii)* Transportation of the vapor from its source to the substrate and *(iii)* Film growth on the substrate. Depending on the physical method used for transferring a solid material, called *target*, into vapor phase, PVD processes can be classified into sputtering and evaporation [5].

The outstanding qualities of these processes are the versatility of both, potential substrate and coating materials. Using PVD it is possible to deposit nearly every kind of material; metals, alloys and compounds as well as several organic materials [5]. PVD processes also offer the option of reactive deposition. In this case a reactive gas is injected into the vacuum chamber, which forms a chemical compound with the evaporated or sputtered material [16]. The substrate temperatures can be varied within a wide range, allowing also the use of temperature sensitive substrates [5].

2.1.1. Cathodic Arc Evaporation

Using cathodic arc evaporation, the vapor is produced by an arc - a high current, low voltage electrical discharge - between two electrodes in a vacuum chamber, where the target forms the cathode (Fig. 1a) [17]. The point of high current density (10^6 to 10^{12} A/m²), where the arc meets the target, is called cathode spot. The cathode spot moves randomly and rapidly over the cathode surface. The high current density concentrated on the small spot (10^{-8} to 10^{-4} m) leads to a fast heating of the surface, resulting in an explosive evaporation. The ionization rates are depending on the material and can be up to 100 %. The plasma produced at the cathode spots contains multiply ionized atoms and expands quickly into the vacuum [19-21]. A main disadvantage of cathodic arc evaporation is the emission of droplets of molten target material from the cathode spot [21]. These droplets are incorporated as defects into the growing film, acting as renucleation sites leading to voids and microstructural coarsenings (Fig. 1b). The developing structures on the one hand provide high diffusivity paths and on the other hand represent mechanically weak spots [23]. Additionally, the droplets are responsible for the high surface roughness of arc evaporated coatings. An approach to prevent droplets is to separate them from the flux of ions by magnetic filtering [21].

The main benefits of cathodic arc evaporation are the high degree of plasma ionization and the high ion energies reached, resulting in very dense coatings with increased wear resistance [24, 25].

(a) (b)

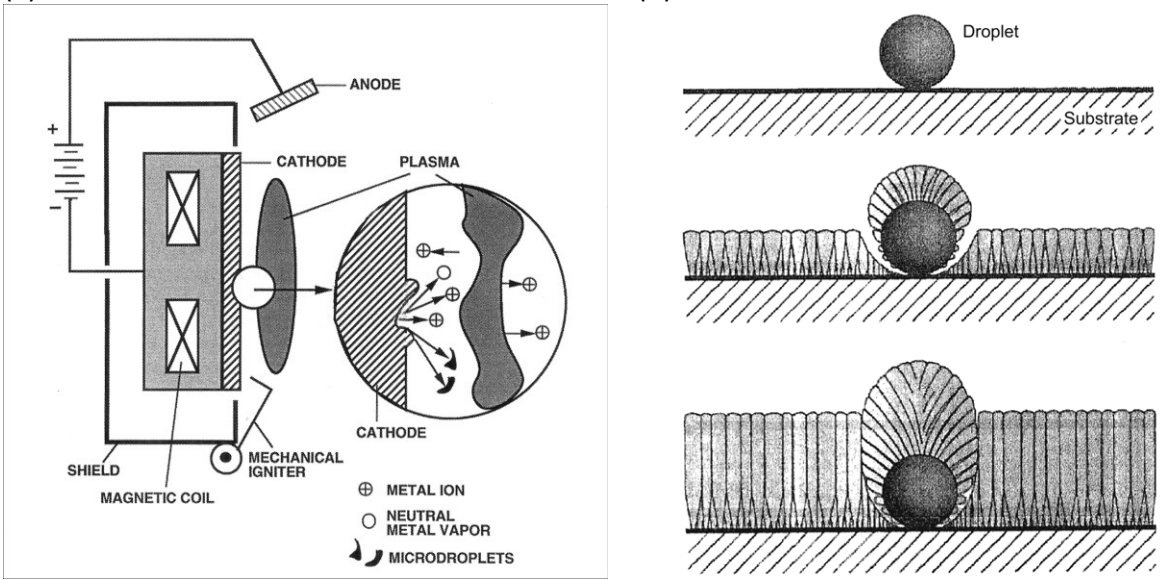

Fig. 1: (a) Illustration of a cathodic arc source and the cathode spot [18]. (b) Droplet and its effect on coating growth [22].

2.1.2. Sputter Deposition

Using sputter deposition, the transfer of the solid deposition material into the vapor phase is achieved by bombarding the target surface with energetic ions. The process is based on energy and momentum transfer from the impinging ions to the surface atoms of the target. This results either in direct ejection of surface atoms or in a collision cascade finally leading to ejection of surface atoms (Fig. 2), if the energy of the scattered atoms is higher than the surface binding energy. The ejected particles are mainly neutrals. In order to provide the ion bombardment, an inert working gas (e.g. Ar) is introduced into the vacuum chamber. By applying a voltage between target (cathode) and substrate holder (anode), a glow discharge is ignited, resulting in the ionization of the working gas. The ionized working gas is called plasma [5, 19].

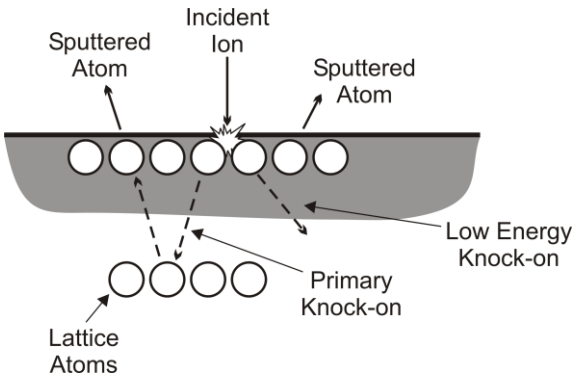

Fig. 2: Illustration of the basic momentum transfer processes during sputtering [5].

The main advantages of sputter deposition compared to arc evaporation are the smooth coating surface and the fact that the formation of vapor is realized by momentum transfer and not thermally, thus even materials with high melting points can be sputter deposited [18].

2.2. Chemical Vapor Deposition

Using chemical vapor deposition (CVD), gaseous precursors are introduced into a reaction chamber, where the coating is deposited. The main steps of a CVD process are illustrated in Fig. 3. Dissociation and chemical surface reactions of the precursors, which are required for deposition of the coatings, are mainly thermally activated, e.g. by high temperatures or by laser-assistance. Nevertheless, there are also less stable precursor materials, which react at lower temperatures, but these are mostly metal-organic compounds. Another possibility is the kinetic activation using plasma. In this case, the term plasma assisted chemical vapor deposition (PACVD) is used [26, 27]. The CVD reactor can be either a hot-wall reactor, where the substrate is placed into a heated furnace for indirect heating, or a cold wall reactor, where only the substrate is heated (either inductively or resistively). Another important process parameter is the deposition pressure, as the internal gas stream velocities and thus, the residence time and the reactant diffusion to the substrate surface are depending on the pressure [27].

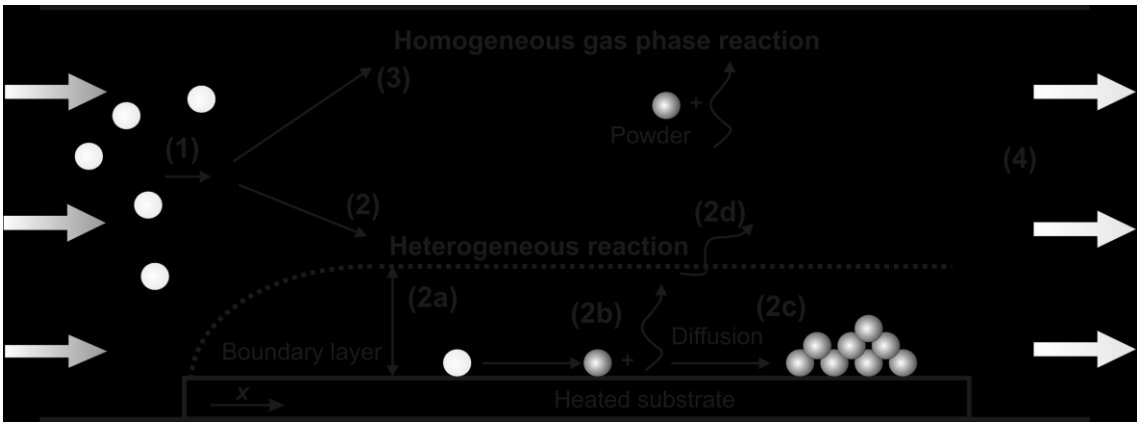

Fig. 3: Illustration of the main process steps during CVD. (1) Gas feed, (2) heterogeneous reaction, comprising (2a) the transport of the reactants through the boundary layer and adsorption, (2b) chemical reactions at the substrate surface, (2c) nucleation and growth and (2d) desorption of by-products. (3) Homogeneous gas phase reaction, (4) gas exhaust [27].

A main advantage of CVD is the high *throwing power*, which describes the ability to coat substrate regions which are not in the line-of-sight and consequently, the ability to coat also irregularly shaped substrates [5]. Further advantages are the possibility to coat great quantities of substrates and to achieve high coating thicknesses.

3. Thin Film Growth

After the species from the vapor phase, produced by physical methods (PVD) or provided by gaseous precursors (CVD), impinge on the substrate surface, they are either reflected or, if they lose enough energy to the substrate lattice, they become loosely bonded. These loosely bonded species diffuse over the surface until they are either desorbed or they reach other loosely bonded species and build stable nuclei or condense at already existing nuclei. Nuclei are preferably formed at low energy sites, like lattice defects, atomic steps or scratches in the surface. The mobility of the species on the surface depends on their kinetic energy, the substrate temperature and the intensity of interactions between species and substrate. The nuclei density and the nuclei growth mode determine the contact area between coating and substrate and thus, the adhesion. After nucleation, the nuclei grow and coalesce, resulting in a continuous layer [5, 16].

The film formation occurs according to one of the three basic growth modes shown in Fig. 4: *(i)* Island (Volmer-Weber) growth occurs when the binding energy between the deposited species is stronger than between the species and the substrate. *(ii)* Layer-by-layer (Frank-van der Merwe) growth takes place when the opposite is the case; the deposited species are more strongly bound to the substrate than to each other. *(iii)* Mixed layer-island (Stranski-Krastanov) growth is a combination of the two other modes, where first one or more mono-layers are formed, but then further layer growth becomes unfavorable and island growth occurs [18].

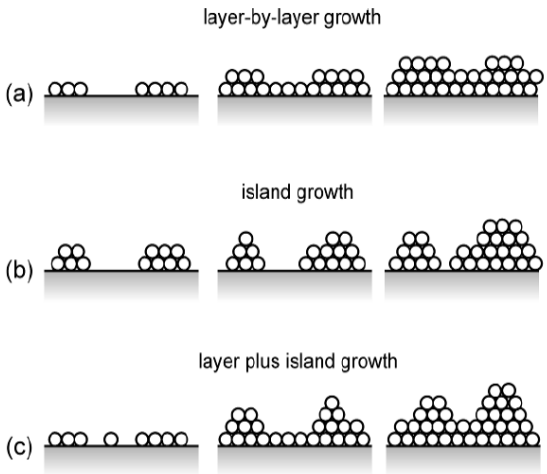

Fig. 4: Thin film growth modes: (a) layer-by-layer, (b) island and (c) mixed layer-island growth [18].

The nucleation and growth kinetics are strongly influenced by the deposition parameters and determine the coating structure and consequently, also the properties of the coating. Movchan and Demchishin [28] were the first to propose a structure zone model (SZM), which associates the observed structure and the growth parameters. They investigated thick coatings grown by thermal evaporation and related their structure to the homologous temperature (T_s/T_m), where T_s is the substrate temperature and T_m is the melting temperature. They distinguished three characteristic zones [28]. Thornton [29] adapted their model by considering the inert sputtering gas pressure and introduced a fourth zone, the so called transition zone T, which is formed between zone 1 and 2. Zone 1 is characterized by small surface mobility of the condensed species; thus the growth is significantly affected by shadowing effects, resulting in a porous columnar structure. In zone T the surface diffusion is more pronounced and competitive growth develops, leading to a denser and fibrous structure. In zone 2 surface diffusion is dominating, leading to a dense film consisting of columnar crystals expanding from bottom to top of the film. Zone 3 is determined by bulk diffusion, resulting in a recrystallized structure with equiaxed grains and further densification of the film [5, 29, 30]. Messier *et al.* [31] modified Thornton's SZM, by introducing the substrate bias potential instead of the inert sputtering gas pressure. Anders [32] recently proposed an extended SZM, illustrated in Fig. 5a, based still on the original three structure zones and zone T. Additionally, this SZM includes energetic deposition, characterized by a large flux of ions. There, the structure is related to the generalized temperature T*, the normalized energy flux E* and the net film thickness t*. T* is defined as the homologous temperature plus the characteristic temperature of a heated region caused by the potential energy of particles arriving on the coating surface. E* is a measure for displacement and heating effects caused by the kinetic energy of the arriving particles on the coating surface. There are two "non-accessible regions" in the diagram. One is at very low T* and high E*, since all energy forms brought to the surface by impinging particles lead to heating of the film and thus, shift the working point to a higher temperature. The second region is at very low E*, because the ions from the plasma have a certain velocity and consequently also a certain energy.

The three typical structures of CVD coatings are shown in Fig. 5b. In zone 1 the film consists of columnar grains with dome-like caps. This structure occurs at high deposition temperatures and is a result of high surface diffusion and uninterrupted grain growth. The structure in zone 2 is also columnar, but due to lower diffusion and/or higher supersaturation the grains are more faceted and angular. In zone 3 the film consists of fine equiaxed grains. This structure is achieved at high supersaturations and low temperatures as well as low pressures, minimizing the diffusion processes [33].

(a) (b)

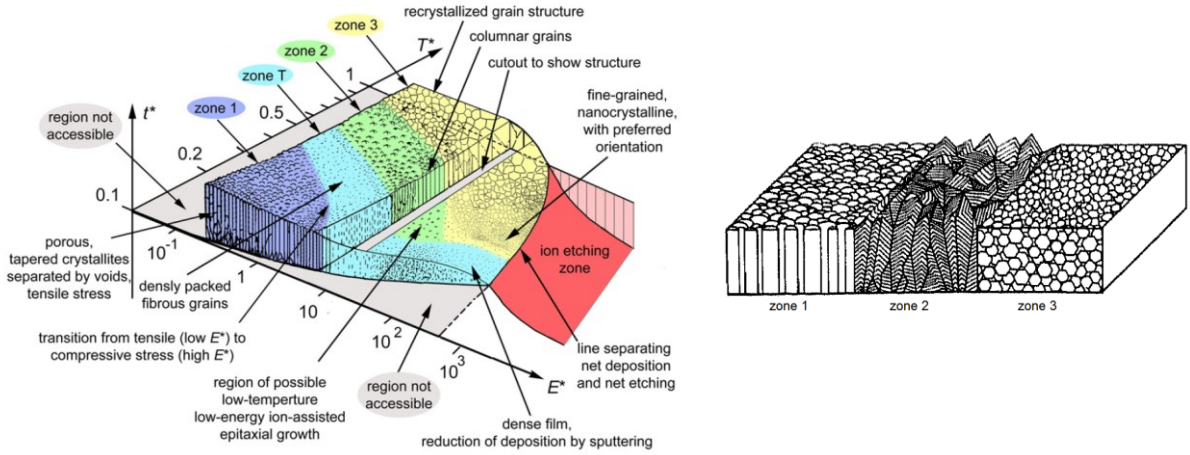

Fig. 5: Structure zone models proposed by (a) Anders [32] and (b) Pierson [33].

4. Hard Coatings

4.1. $Ti_{1-x}Al_xN$ Coatings

$Ti_{1-x}Al_xN$ coatings are mainly deposited by PVD processes. Since these are thermodynamically non-equilibrium processes, the composition range is basically not limited and metastable solid solutions can be synthesized [34, 35]. TiN crystallizes in the face centered cubic (fcc) structure, while the stable form of AlN is the wurtzite (w) structure [34, 36, 37]. The formation of metastable $Ti_{1-x}Al_xN$ is based on the substitution of Ti by Al atoms in the fcc-TiN lattice. Single-phase fcc-$Ti_{1-x}Al_xN$ is formed up to Al contents of $x \sim 0.67$ (Fig. 6). Further increasing of the Al content yields a dual-phase structure followed by a single-phase wurtzite structure, where the Ti atoms substitute for the Al atoms in the w-AlN lattice [39-42]. Within the cubic regime, alloying of Al to the TiN system leads to enhanced mechanical properties such as hardness and wear resistance. Also the oxidation resistance remarkably increases with increasing Al content, due to the formation of a stable oxidation barrier of Al_2O_3 at the surface [36, 43, 44]. However, when the wurtzite structure is formed, these properties deteriorate [41-45].

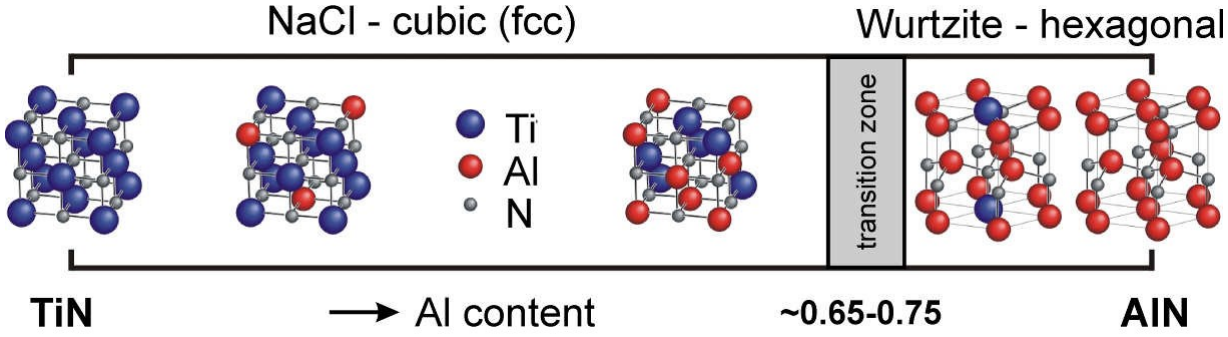

Fig. 6: Structural development of $Ti_{1-x}Al_xN$ with increasing Al content [38].

At elevated temperatures (≥ 800 °C) the metastable $Ti_{1-x}Al_xN$ solid solution decomposes into fcc-TiN and fcc-AlN domains, leading to age hardening due to coherency strains between the matrix and the formed small coherent domains. This behavior is known as spinodal decomposition. Further increasing of the temperature leads to the transformation of the metastable fcc-AlN into the stable w-AlN, resulting in a hardness loss [41, 42, 46].

In the recent years, the deposition of $Ti_{1-x}Al_xN$ coatings by CVD has gained increasing interest. The development of a suitable deposition process was a challenging task, since conventional thermal CVD is not possible due to the high necessary process temperatures, which would lead to decomposition of the $Ti_{1-x}Al_xN$ coating. Nowadays, CVD processes for the deposition of $Ti_{1-x}Al_xN$ coatings are available, which are in general based on low pressures

(~100 mbar) and moderate deposition temperatures (800 – 900 °C) [47-50]. Using CVD, the deposition of $Ti_{1-x}Al_xN$ coatings with x-values up to 0.9, showing remarkable results in cutting tests, is possible. These coatings exhibit a dual-phase structure or more precisely, the structure consists of alternating fcc-$Ti_{1-x}Al_xN$ and w-AlN lamellae [50]. Nevertheless, deposition of $Ti_{1-x}Al_xN$ by PVD is still predominant and was also used within the present work.

4.1.1. TiAlTaN

The properties of the $Ti_{1-x}Al_xN$ coating system can be further improved by the addition of different alloying elements [2, 7, 8]. Alloying with Ta has beneficial effects on the mechanical and tribological properties, as it fosters the formation of the fcc phase at the expense of the wurtzite phase [7]. At elevated temperatures, the metastable fcc-TiAlTaN solid solution decomposes, in analogy to $Ti_{1-x}Al_xN$, into fcc-$Ti_{1-z}Ta_zN$-enriched and fcc-AlN-enriched domains. Nevertheless, the addition of small amounts of Ta (up to 10 at.-%) to the $Ti_{1-x}Al_xN$ system leads to an increase of the onset temperature for the formation of w-AlN by up to 300 °C, depending on the Ta amount. Since the hardness maximum, due to age hardening, is generally observed ~100 °C prior the formation of w-AlN and since the Ta containing coatings show significantly higher hardness values in as-deposited state, compared to $Ti_{1-x}Al_xN$, higher hardness values are obtained up to higher temperatures [51]. Further, a significantly improved tribological behavior at temperatures exceeding 900 °C can be observed for TiAlTaN coatings. This is due to a higher oxidation resistance compared to $Ti_{1-x}Al_xN$. The formed oxide scale contains α-Al_2O_3, rutile-type TiO_2 and anatase-type TiO_2. The oxide scale is divided in an Al-rich top-layer and a Ti-Ta-rich sublayer, where the Ta is incorporated in the TiO_2 lattice. In the rutile-type TiO_2 the Ti^{4+} is replaced by Ta^{5+}, leading to a reduced amount of O-vacancies and thus, a decreased mass transport of O in rutile to the oxide-nitride interface and consequently to a slower oxidation of Ti [2, 8].

4.2. Al_2O_3 Coatings

Due to its unique combination of properties, such as high hot hardness, chemical inertness and low thermal conductivity, Al_2O_3 is a common coating material for cemented carbide cutting tools [12-14]. In addition to the stable α-phase, Al_2O_3 exists in several metastable polymorphs (γ, η, δ, θ, χ and κ) [52]. Al_2O_3 coatings are mainly deposited using CVD, where the α- and the κ-phase are prevalent. However, using CVD the deposition temperatures are in the range of ~1000 °C, limiting the choice of substrate materials. Thus, the synthesis of Al_2O_3 by PVD is an interesting alternative which is, due to the electrically insulating nature of

Al_2O_3, still a challenge [53]. Using PVD, temperatures between 350 and 550 °C are necessary to grow crystalline γ-Al_2O_3. Coatings deposited at lower temperatures are reported to be X-ray amorphous [54-57]. For the deposition of the desired stable α-Al_2O_3, deposition temperatures of ~700 °C are required [58, 59]. Sputter deposited γ-Al_2O_3 coatings have a high thermal stability, without any phase transformation up to 1000 °C [53]. Nevertheless, CVD is still the dominating method for synthesis of Al_2O_3 coatings and was also used for the deposition of the Al_2O_3 coatings within the present thesis.

4.2.1. α-Al_2O_3

α-Al_2O_3 belongs to the trigonal crystal system and has a rhombohedrally centered hexagonal lattice. The crystal structure of α-Al_2O_3 is often described as an approximately hexagonal close-packed (ABAB…) oxygen superlattice, where the Al atoms occupy two thirds of the octahedral interstices [60, 61]. In general, Al_2O_3 coatings are grown on intermediate layers of Ti(C,N), which favors the nucleation of κ-Al_2O_3 [60-63]. Thus, a nucleation (oxidation) step is necessary, after deposition of this Ti(C,N) interlayer, in order to nucleate and grow α-Al_2O_3 in a controlled way [61]. This nucleation step is of crucial importance for the microstructure and wear properties of the α-Al_2O_3 coating [61]. In older publications [12, 60, 63, 64] it is often stated that α-Al_2O_3 exhibits a quite large grain size and rather high porosity. This is due to the fact, that in earlier attempts to deposit α-Al_2O_3, the coating nucleated as κ-Al_2O_3 and the obtained and investigated α-Al_2O_3 coatings were a result of $\kappa \rightarrow \alpha$ transformation [61, 62]. Optimized nucleation of α-Al_2O_3 results in small grains without porosity and considerably improved wear properties [61].

4.2.2. κ-Al_2O_3

The crystallographic structure of κ-Al_2O_3 is primitive orthorhombic with an ABAC… stacking sequence of almost close-packed oxygen planes [12, 60, 62, 63]. At elevated temperatures, e.g. during the deposition process, thermal post-treatments or metal cutting, the metastable κ-phase transforms into the stable α-phase. This $\kappa \rightarrow \alpha$ transformation occurs by a nucleation and growth process, where existing thermal cracks (due to a misfit between the thermal expansion coefficient of the coating and the substrate) act as nucleation sites. The $\kappa \rightarrow \alpha$ transformation is accompanied by a volume shrinkage of ~7 %, leading to a secondary crack network, consequently deteriorating coating performance [60, 61, 64]. If the $\kappa \rightarrow \alpha$ transformation can be avoided, the κ-phase exhibits advantages compared to the α-phase, e.g. lower thermal conductivity resulting in a more efficient thermal barrier during high speed

cutting [12]. The $\kappa \rightarrow \alpha$ transformation is mainly influenced by the deposition temperature, the deposition time and the contamination of the precursor gas mixture, but also mechanical activation and stresses introduced during cutting can initiate the transformation. Doping with elements like B or Ti retards the transformation [14, 65].

5. Post-deposition Treatment

Further improvement of hard coatings can be achieved by post-deposition treatments, where mechanical and thermal methods can be distinguished. Mechanical treatments enable to enhance the surface topography and to tailor the residual stresses [15, 66-70]. For example, it is beneficial to smoothen the rather rough surface of arc evaporated coatings (compare subsection 2.1.1.) or to introduce compressive stresses into CVD coatings, as they, in general, exhibit tensile stresses after deposition, which is unfavorable during application. Mechanical post-treatments can be e.g. polishing or brushing with abrasive media or blasting processes, where the coating surface is bombarded by granulate material (Fig. 7). This can be done in dry or wet environment [15, 66-70].

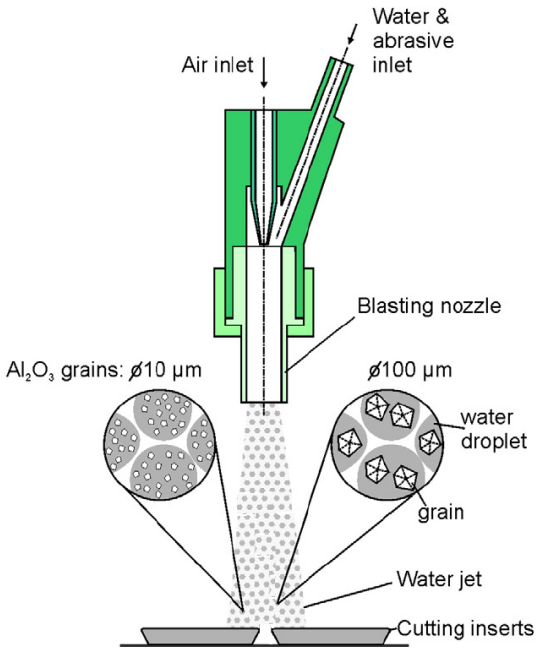

Fig. 7: Illustration of wet-blasting process [modified 69].

Bouzakis *et al.* [66-70] comprehensively investigated the influence of both, wet- and dry-blasting on the mechanical properties and on the wear during milling of PVD coatings. They reported on a significant increase of tool life due to dry-blasting with Al_2O_3 particles [66-68]. Investigations on samples wet-blasted using different pressures and sharp-edged Al_2O_3 particles with two different grain sizes revealed, that the coarser blasting material or a higher blasting pressure lead to higher compressive stresses [69]. Further, they investigated the effect of dry-blasting with sharp-edged Al_2O_3 and spherical ZrO_2 particles on the wear behavior. Due to the smooth spherical surface of the ZrO_2, the abrasion was less intense and the coating material deformation higher compared to the treatment with the sharp-edged Al_2O_3,

resulting in decreased film ductility and consequently deteriorating cutting performance [70]. Barbatti *et al.* [15] investigated the influence of wet-blasting with Al_2O_3 particles on the microstructure and residual stresses of CVD κ-Al_2O_3 coatings. No $\kappa \rightarrow \alpha$ transformation induced by the blasting treatment could be observed. The effects of the blasting treatment were confined to the top layer, where crack formation and propagation due to the treatment could be detected. The tensile as-deposited residual stresses were not affected by the blasting treatment. Additionally, there are also a few reports available dealing with the depth-resolved determination of the compressive stresses introduced by blasting treatments [71-73]. However, in conclusion it is difficult to compare results of different blasting treatments, since they strongly depend on a variety of parameters, e.g. wet- or dry-blasting, blasting material (grain size, shape, hardness, …), number of nozzles, working angle, blasting time and blasting pressure.

Thermal post-deposition treatments can be used to improve the microstructure and to modify the surface, e.g. by annealing in different atmospheres, in order to reduce the friction between work-piece and coating. Besides annealing in inert or vacuum environments to study thermal stability of metastable hard coatings like $Ti_{1-x}Al_xN$ (compare subsection 4.1), no detailed reports on modifying the surface of hard coatings by thermal treatments in controlled reactive atmospheres are available.

6. Summary and Conclusion

The aim of the present thesis is to improve the efficiency of coating deposition and to optimize the hard coatings for more economic cutting processes. In order to improve the efficiency of coating synthesis, the sputter targets play a crucial role. Thus, the influence of two different sputter target types (i.e. powder metallurgically produced compound TiAl targets and mosaic TiAl targets prepared by casting) on the deposition process as well as on the structure, the mechanical and tribological properties of the synthesized $Ti_{1-x}Al_xN$ coatings was investigated. While the decomposition of metastable $Ti_{1-x}Al_xN$ coatings at elevated temperatures is well known, all coatings discussed in literature exhibit compressive residual stresses in the as-deposited state. Thus, a series of coatings with stresses ranging from tensile to compressive was successfully synthesized using different bias voltages. The influence of these residual stresses on the spinodal decomposition was investigated by vacuum annealing treatments and subsequent X-ray diffraction measurements. Another approach to improve the cutting performance is based on low-friction surfaces, where an alternative to existing complex and consequently quite expensive deposition processes for low-friction coatings was developed. Arc evaporated TiAlTaN coatings were thermally treated in methane, which resulted in formation of a carbon deposit on the coating surface. This carbon deposit is expected to positively affect the friction behavior. A different possibility to enhance the coating performance is based on blasting treatments. The relaxation of the compressive stresses, introduced by dry-blasting of α- and κ-Al_2O_3 CVD hard coatings using different blasting pressures and materials, at elevated temperatures was investigated as well as the effects of these dry-blasting treatments on the friction behavior.

Using compound targets, a ~44 % higher deposition rate than for the mosaic targets could be obtained. Additionally, the $Ti_{1-x}Al_xN$ coatings grown from the compound targets showed reduced friction and higher wear resistance compared to the mosaic targets. The differences can be related to a different sputtering behavior of the targets. For metastable $Ti_{1-x}Al_xN$ solid solutions, spinodal decomposition at elevated temperatures leads to enhanced coating performance due to age hardening, while the onset of the formation of w-AlN results in the degradation of the coating performance. Tensile residual stresses promote the formation of more volume consuming fcc-TiN domains during decomposition, whereas compressive stresses foster the formation of smaller fcc-AlN domains. Smaller grain sizes were found to cause earlier precipitation of w-AlN. In a next step, commercial TiAlTaN coatings were thermally treated in methane at 900 °C to combine the beneficial effects of both, age hardening and friction reduction due to the formation of a carbon deposit on top. As a result, friction coefficients comparable to values for DLC and MoS_2, tested under similar conditions, could

be obtained. For dry-blasted α- and κ-Al_2O_3 CVD coatings the degradation of the introduced compressive stresses during high-temperature exposure plays a decisive role for the coating performance. The stress relaxation strongly depends on the blasting medium. For α-Al_2O_3 dry-blasted using a globular medium, a complete stress relaxation could already be observed after annealing at 500 °C, while for α-Al_2O_3 dry-blasted using an edged medium as well as for κ-Al_2O_3 an annealing temperature of 900 °C was necessary for stress relaxation. A drop of the friction coefficient at ~700 °C could be observed, which was due to softening of the blasting material transferred to the coating surface.

While this thesis presents several attempts to establishing the basis for further optimization of hard coatings, it also allows to point out several areas of possible future work. Within the present theses, the residual stresses were determined utilizing a conventional X-ray diffractometer and the $\sin^2\psi$ method and thus, are average stress values. Especially for the thick dry-blasted α- and κ-Al_2O_3 CVD coatings, it would be interesting to obtain information about the stress gradient over the coating thickness. Possibilities for the depth-resolved determination of stresses exist. However, up to now they have not been sufficiently used and they have also not been accessible within the present work. Additionally, for coating optimization there is a need to correlate the basic findings on coating microstructure and properties as well as their degradation with the evaluation of the coating performance in cutting tests.

7. References

[1] V. Derflinger, H. Brändle, H. Zimmermann, Surf. Coat. Technol. 113 (1999) 286.

[2] M. Pfeiler, C. Scheu, H. Hutter, J. Schnöller, C. Michotte, C. Mitterer, M. Kathrein, J. Vac. Sci. Technol. A27 (2009) 554.

[3] M. Kathrein, C. Michotte, M. Penoy, P. Polcik, C. Mitterer, Surf. Coat. Technol. 200 (2005) 1867.

[4] P.H. Mayrhofer, C. Mitterer, L. Hultman, H. Clemens, Progr. Mater. Sci. 51 (2006) 1032.

[5] R.F. Bunshah, Deposition Technologies for Films and Coatings, Noyes Publications, New Jersey, 1982.

[6] I. Petrov, P.B. Barna, L. Hultman, J.E. Greene, J. Vac. Sci. Technol. A 21 (2003) 117.

[7] K. Kutschej, P.H. Mayrhofer, M. Kathrein, C. Michotte, P. Polcik, C. Mitterer, in: G. Kneringer. P. Roedhammer, H. Wildner (eds.) Proceedings of the 16th International Plansee Seminar 2005, vol. 2, pp. 774-778. Plansee Holding AG, Reutte, Tyrol, Austria (2005).

[8] M. Pfeiler, G.A. Fontalvo, J. Wagner, K. Kutschej, M. Penoy, C. Michotte, C. Mitterer, M. Kathrein, Tribol. Lett. 30 (2) (2008) 91.

[9] K. Kutschej, P.H. Mayrhofer, M. Kathrein, P. Polcik, C. Mitterer, Surf. Coat. Technol. 188-189 (2004) 358.

[10] F. Vaz, L. Rebouta, M. Andritschky, M.F. da Silva, J.C. Soares, Surf. Coat. Technol. 98 (1998) 912.

[11] K. Kutschej, N. Fateh, P.H. Mayrhofer, M. Kathrein, P. Polcik, C. Mitterer, Surf. Coat. Technol. 200 (2005) 113.

[12] S. Ruppi, J. Phys. IV France 11 (2001) 847.

[13] A. Osada, E. Nakamura, H. Homma, T. Hayahi, T. Oshika, Int. J. Refract. Met. H. 24 (2006) 387.

[14] D. Hochauer, C. Mitterer, M. Penoy, C. Michotte, H.P. Martinz, M. Kathrein, Surf. Coat. Technol. 204 (2010) 3713.

[15] C. Barbatti, J. Garcia, R. Pitonak, H. Pinto, A. Kostka, A. Di Prinzio, M.H. Staia, A.R. Pyzalla, Surf. Coat. Technol. 203 (2009) 3708.

[16] R.A. Haefer, Oberflächen- und Dünnschicht-Technologie, Teil I, Beschichtungen von Oberflächen, Springer Verlag, Berlin, Heidlberg, 1987.

[17] J.M. Lafferty in: R.L. Boxman, D.M. Sanders, P.J. Martin (eds.) Handbook of vacuum arc science and technology, Noyes Publication, New Jersey, 1995.

[18] M. Ohring, The materials science oft hin films – deposition and structure, Academic Press, San Diego, Second edition, 2002.

[19] B. Rother, J. Vetter, Plasmabeschichtungsverfahren und Hartstoffschichten, Deutscher Verlag für Grundstoffindustrie, Leipzig, 1992.

[20] P.C. Johnson in: J.L. Vossen, W. Kern (eds.) Thin film processes II, Academic Press, San Diego, 1991.

[21] D.M. Sanders. A. Anders, Surf. Coat. Technol. 133-134 (2000) 78.

[22] I. Petrov, P. Losbichler, D. Bergstrom, J.E. Greene, W.-D. Münz, T. Hurkmans, T. Trinh, Thin Solid Films 302 (1997) 179.

[23] A. Hörling, L. Hultman, M. Odén, J. Sjölén, L. Karlsson, J. Vac. Sci. Technol. A 20 (2002) 1815.

[24] A. Anders, Cathodic arcs, From fractal spots to energetic condensation, Springer, New York, 2008.

[25] P.J. Marti in: R.L. Boxman, P.J. Martin, D.M. Sanders (eds.) Handbook of vacuum arc science and technology, Noyes Publication, New Jersey, 1995.

[26] H. Frey, Vakuumbeschichtung 1, Plasmaphysik – Plasmadiagnostik – Analytik, VDI Verlag, Düsseldorf, 1995.

[27] K.L. Choy, Prog. Mater. Sci. 48 (2003) 57.

[28] B.A. Movchan, A.V. Demchishin, Phys. Met. Metallogr. 28 (1969) 653.

[29] J.A. Thornton, J. Vac. Sci. Technol. 11(4) (1974) 666.

[30] P.B. Barna, M. Adamik, Thin Solid Films 317 (1998) 27.

[31] R. Messier, A.P. Giri, R.A. Roy, J. Vac. Sci. Technol. A 2 (2) (1984) 500.

[32] A. Anders, Thin Solid Films 518 (2010) 4087.

[33] H.O. Pierson, Handbook of chemical vapour deposition, Noyes Publications, Park Ridge, 1999.

[34] H.A. Jehn, B. Rother, Int. J. Refract. Metals Hard Mater. 14 (1996) 87.

[35] J. Kohlscheen, H.-R. Stock, P. Mayr, Surf. Coat. Technol. 120-121 (1999) 740.

[36] S. PalDey, S.C. Deevi, Mat. Sci. Eng. 342 (2003) 58.

[37] M. Durandurdu, J. Phys. Chem. Solids. 69 (11) (2008) 2894.

[38] M. Kawate, A. Kimura, T. Suzuki, J. Vac. Sci. Technol. A20(2) (2002) 569.

[39] R. Cremer, M. Witthaut, D. Neuschütz, in: W.D. Cho, H.Y. Sohn (eds.), Value-addition metallurgy, the Minerals, Metals & Materials Society, Warrendale, 1998.

[40] A. Kimura, H. Hasegawa, K. Yamada, T. Suzuki, Surf. Coat. Technol. 120-121 (1999) 438.

[41] A. Hörling, L. Hultman, M. Odén, J. Sjölén, L. Karlsson, J. Vac. Sci. Technol. A20 (5) (2002) 1815.

[42] A. Hörling, L. Hultman, M. Odén, J. Sjölén, L. Karlsson, Surf. Coat. Technol. 191 (2005) 384.

[43] I.-W. Park, D.S. Kang, J.J. Moore, S.C. Kwon, J.J. Rha, K.H. Kim, Surf. Coat. Technol. 201 (2007) 5223.

[44] E. Spain, J.C. Avelar-Batista, M. Letch, J. Housden, B. Lerga, Surf. Coat. Technol. 200 (2005) 1507.

[45] K. Kutschej, P.H. Mayrhofer, M. Kathrein, P. Polcik, R. Tessadri, C. Mitterer, Surf. Coat. Technol. 200 (2005) 2358.

[46] P.H. Mayrhofer, A. Hörling, L. Karlsson, J. Sjölén, T. Larsson, C. Mitterer, L. Hultman, Appl. Phys. Lett. 83 (10) (2003) 2049.

[47] D. Heim, R. Hochreiter, Surf. Coat. Technol. 98 (1998) 1553.

[48] I. Endler, M. Höhn, M. Herrmann, R. Pitonak, S. Ruppi. M. Schneider, H. van den Berg, H. Westphal, Surf. Coat. Technol. 203 (2008) 530.

[49] I. Endler, M. Höhn, M. Herrmann, H. Holzschuh, R. Pitonak, S. Ruppi, H. van den Berg, H. Westphal, L. Wilde, Surf. Coat. Technol. 205 (2010) 1307.

[50] R. Pitonak, A. Köpf, R. Weißenbacher, J. Keckes, M. Stefenelli, J. Todt, I. Endler, M. Höhn, in: H. Kestler, L.S. Sigl, D. Széchényi, J. Wagner (eds.) Proceedings of the 18th International Plansee Seminar 2013, HM 37. Plansee Holding AG, Reutte, Tyrol, Austria (2013).

[51] R. Rachbauer, D. Holec, P.H. Mayrhofer, Surf. Coat. Technol. 211 (2012) 98.

[52] I. Levi, D. Brandon, J. Am. Ceram. Soc. 81 (1998) 1995.

[53] V. Edlmayr, M. Moser, C. Walter, C. Mitterer, Surf. Coat. Technol. 204 (2010) 1576.

[54] A. Schütze, D.T. Quinto, Surf. Coat. Technol. 162 (2003) 174.

[55] R. Cremer, M. Witthaut, D. Neuschütz, G. Erkens, T. Leydendecker, M. Feldhege, Surf. Coat. Techno. 120 (1999) 213.

[56] T.C. Chou, D. Adamson, J. Mardinly, T.G. Nieh, Thin Solid Films 205 (1991) 131.

[57] A. Astrand, T.I. Selinder, F. Fietzke, H. Klostermann, Surf. Coat. Technol. 188-189 (2004) 186.

[58] O. Zywitzki, G. Hoetzsch. Surf. Coat. Technol. 94-95 (1997) 303.

[59] T. Kohara, H. Tamagaki, Y. Ikari, H. Fujii, Surf. Coat. Technol. 185 (2004) 166.

[60] S. Vuorinen, L. Karlsson, Thin Solid Films 214 (1992) 132.

[61] S. Ruppi, Int. J. Refract. Met. H 23 (2005) 306.

[62] S. Ruppi, A. Larsson, A. Flink, Thin Solid Films 516 (2008) 5959.

[63] S. Ruppi, A. Larsson, Thin Solid Films 388 (2001) 50.

[64] J. Skogsmo, M. Halvarsson, S. Vuorinen, Surf. Coat. Technol. 54-55 (19952) 186.

[65] M. Kathrein, W. Schintlmeister, W. Wallgram, U. Schleinkofer, Surf. Coat. Technol. 163-164 (2003) 181.

[66] K.-D. Bouzakis, G. Skordaris, I. Mirisidis, N. Michailidis, G. Mesomeris, E. Pavlidou, G. Erkens, Surf. Coat. Technol. 200 (2005) 1879.

[67] K.-D. Bouzakis, G. Skordaris, N. Michailidis, A. Asimakopoulos, G. Erkens, Surf. Coat. Technol. 200 (2005) 128.

[68] K.-D. Bouzakis, S. Gerardis, G. Skordaris, G. Katirtzoglou, S. Makrimallakis, F. Klocke, E. Bouzakis, Surf. Coat. Technol. 204 (2009) 1081.

[69] K.-D. Bouzakis, E. Bouzakis, G. Skordaris, S. Makrimmallakis, A. Tsouknidas, G. Katirtzoglou, S. Gerardis, Surf. Coat. Technol. 205 (2011) S128.

[70] K.-D. Bouzakis, F. Klocke, G. Skordaris, E. Bouzakis, S. Gerardis, G. Katirtzoglou, S. Makrimmallakis, Wear 271 (2011) 783.

[71] M. Klaus, Ch. Genzel, H. Holzschuh, Thin Solid Films 517 (2008) 1172.

[72] M. Klaus, Ch. Genzel, Adv. Eng. Mater. 8 (2011) 845.

[73] M. Bartosik, R. Pitonak, J. Keckes, Adv. Eng. Mater. 13 (2011).

8. Publications

8.1. List of Included Publications

I. A comparative study on $Ti_{1-x}Al_xN$ coatings reactively sputtered from compound and from mosaic targets

N. Schalk, T. Weirather, C. Polzer, P. Polcik, C. Mitterer

Surface and Coatings Technology 205 (2011) 4705-4710.

II. Influence of residual stresses and grain size on the spinodal decomposition of metastable $Ti_{1-x}Al_xN$ coatings

N. Schalk, C. Mitterer, J. Keckes, M. Penoy, C. Michotte

Surface and Coatings Technology 209 (2012) 190-196.

III. Friction reduction by thermal treatment of arc evaporated TiAlTaN coatings in methane

N. Schalk, C. Mitterer, I. Letofsky-Papst, C. Czettl, B. Sartory, M. Penoy, C. Michotte

Accepted for publication in Tribology International.

IV. Dry-blasting of α- and κ-Al_2O_3 CVD hard coatings: Friction behaviour and thermal stress relaxation

N. Schalk, C. Mitterer, C. Czettl, B. Sartory, M. Penoy, C. Michotte

Submitted for publication.

8.2. Publications Related to this Work

V. Tribological properties of Al_2O_3 hard coatings modified by mechanical blasting and polishing post-treatment

A. Riedl, N. Schalk, C. Czettl, B. Sartory, C. Mitterer

Wear 289 (2012) 9-16.

8.3. My Contribution to the Included Publications

	Conception and planning	Experiments	Analysis and interpretation	Manuscript preparation
Publication I	100	100	100	100
Publication II	100	95	95	95
Publication III	100	30	100	100
Publication IV	100	10	100	100

Supervision not included!

Publication I

A comparative study on $Ti_{1-x}Al_xN$ coatings reactively sputtered from compound and from mosaic targets

N. Schalk, T. Weirather, C. Polzer, P. Polcik, C. Mitterer

Surface and Coatings Technology 205 (2011) 4705-4710

A comparative study on $Ti_{1-x}Al_xN$ coatings reactively sputtered from compound and from mosaic targets

N. Schalk[a,b], T. Weirather[a], C. Polzer[c], P. Polcik[c], C. Mitterer[a]

[a] *Department of Physical Metallurgy and Materials Testing, Montanuniversität, Franz-Josef-Straße 18, A-8700 Leoben, Austria*

[b] *Materials Center Leoben Forschung GmbH, Rosegger Straße 12, A-8700 Leoben, Austria*

[c] *PLANSEE Composite Materials GmbH, Siebenbürgerstraße 23, D-86983 Lechbruck am See, Germany*

Abstract

The aim of this work is to illuminate the influence of two widely applied target types, i.e. TiAl compound targets produced by powder metallurgy and mosaic TiAl targets, on the sputter deposition process as well as structure and properties of the obtained coatings. After development of a sputter process for the compound targets by optimization of cathode power and nitrogen partial pressure, this process was compared to the commercially applied mosaic target process by taking into account the sputter yields of Ti and Al and the respective deposition rates. The deposition rate achieved with the compound targets was ~ 44 % higher than that obtained for the mosaic targets. The Al content in the coatings deposited from the compound targets was slightly higher and the domain size of the formed cubic $Ti_{1-x}Al_xN$ solid solution considerably larger than for the coatings deposited from the mosaic targets. The coatings grown from the compound targets showed, in contrast to those synthesized from the mosaic targets, tensile stresses. While the hardness of the coatings sputtered from the compound targets was slightly below that of the coatings synthesized from the mosaic targets, both their friction and wear behavior was slightly improved. In summary, it could be shown that using compound TiAl targets manufactured by powder metallurgy, $Ti_{1-x}Al_xN$ coatings with mechanical and tribological properties comparable to those grown from commercially applied mosaic targets can be deposited at significantly higher growth rates.

Keywords: Sputtering, TiAlN coatings, sputter target, structure, properties

1. Introduction

High-performance cutting tools contribute to the reduction of machining costs by their longer lifetime and higher cutting speeds [1]. Transition metal nitride based hard coatings like $Ti_{1-x}Al_xN$ or $Cr_{1-x}Al_xN$ have enabled significant progress in this field, where the quest for new and improved coating materials is one of the major driving forces for the coating community [2]. On the other hand, coating synthesis has to be done efficiently to reduce deposition time, where target manufacturers have to provide targets with high sputtering or evaporation rates which are able to withstand the imposed high thermal loads. Various types of targets for sputter processes are available, which can be manufactured by different processing techniques. Alloy or dual-phase targets are, for example, made by casting or powder metallurgical techniques. Other possibilities are mosaic targets, e.g. with holes filled by additional elements, enabling to vary coating composition through the number and position of holes [3].

Very limited reports are available in literature on the performance of sputter target types, although they may affect the sputtering behavior as well as the structure and properties of the synthesized coatings. To illuminate the role of the target type in a sputter process under industrial conditions, we studied within this work the effect of macroscopically homogeneous compound TiAl targets manufactured by powder metallurgical methods as well as mosaic TiAl targets prepared by casting on deposition process characteristics as well as structure and mechanical/tribological properties of the obtained $Ti_{1-x}Al_xN$ hard coatings.

2. Experimental Details

2.1 Coating Deposition

Two different types of TiAl targets were used for the present work: powder metallurgical compound targets produced by PLANSEE Composite Materials in Lechbruck, Germany, referred to as PM targets in the following, and ingot metallurgically produced mosaic targets provided by CemeCon in Würselen, Germany, referred to as CC targets. Both types of targets have a size of 500 × 88 mm^2 and a total thickness of 10 mm. In case of the mosaic targets of CemeCon type TiAl48GM, the target matrix material is Ti and 48 holes positioned in the center of the erosion track are filled with Al inserts. This mosaic target is 6 mm thick and bonded to a 4 mm thick copper backing plate. The PM compound targets contain 60 at.-% Al and 40 at.-% Ti and are on a macroscopic scale homogeneous, but consist microscopically of two phases, where Ti grains are embedded into an Al matrix [4]. The usable depth of the erosion

track may be close to 10 mm, thus providing a longer target lifetime compared to the mosaic targets.

All coatings for the present work were deposited by reactive unbalanced magnetron sputtering using an industrial-scale CemeCon CC800/9MLT sputtering system equipped with either four mosaic or four PM targets. The substrates used were ground and polished powder metallurgically produced high-speed steel (HSS) disks (Ø 30 × 10 mm) of type HS14-3-5-11 (S290PM grade supplied by Böhler Edelstahl, Kapfenberg, Austria). Additionally, Si (100) sheets with the dimensions 7 × 21 × 0.38 mm^3 were coated. Prior to deposition, the substrates were ultrasonically cleaned in acetone and ethanol. After mounting them on the carousel and evacuating the chamber to a base pressure of ≤ 4 mPa, the substrates were cleaned through a heating step and subsequently by Ar^+ ion etching for 30 min. A unipolarily pulsed bias voltage of -650 V with a pulse frequency of 250 kHz and a reversal time of 1.6 µs was used. The argon flow was set to 200 sccm and the temperature was approximately 450 °C.

For coating deposition, the nitrogen fraction in the process gas was added to a constant argon flow; thus, the process-controlled total pressure is directly related to the nitrogen partial pressure. For the mosaic targets a standard process was available, where the unipolarily pulsed d.c. bias voltage was set to -50 V, the pulse frequency to 350 kHz and the reversal time to 1 µs. Each pair of cathodes was bipolarily pulsed at a frequency of 20 kHz with a duty cycle of 50 % and a cathode power of 7 kW per target. The argon flow was 200 sccm and the total pressure was set to 580 mPa. For the PM targets, each pair of cathodes was bipolarily pulsed at a frequency of 35 kHz with a duty cycle of 50 %; the cathode power and the total pressure were systematically optimized to find an efficient parameter combination with respect to stable process conditions. The flow of the argon working gas was held constant at 230 sccm. The bias voltage was set to -40 V, using the same pulse frequency and reversal time as for the mosaic targets. For both targets, the substrate temperature was 525 … 550 °C, as measured by the softening of quenched steel samples after deposition. While for the mosaic targets a deposition time of 2.5 h was chosen, it had to be reduced to 1.5 h for the PM targets to obtain coating thicknesses in the range of 2.5 – 3.8 µm.

2.2 Coating Characterization

The coating thickness was determined by means of the ball cratering technique using a CSM CaloTest. Energy-dispersive X-ray emission spectroscopy (EDX) utilizing an Oxford Instruments INCA extension in a Zeiss EVO 50 scanning electron microscope (SEM) was used to

determine the coating composition. The crystallographic structure was investigated by X-ray diffraction (XRD) using Cu Kα radiation in Bragg-Brentano as well as grazing incidence (GIXRD) configuration. The investigations were carried out with a Siemens D500 diffractometer. For the GIXRD measurements, an angle of incidence of 2° was chosen. Domain size and strain were determined by the single-line method for analysis of XRD peak broadening using the Pseudo-Voigt function [5]. Film adhesion was determined by Rockwell C indentation adhesion tests according to the VDI guideline [6] utilizing a Mitutoyo DT-10 hardness tester. Hardness and Young's modulus were determined with a UMIS Nanoindenter (Ultra Micro Indentation System) from Fischer-Cripps Laboratories, which is equipped with a Berkovich tip. A plateau test was carried out with maximum and minimum forces of 40 and 2 mN, respectively, with an increment of 2 mN. To measure the biaxial residual stresses, the coated Si substrates were examined by the wafer curvature method using the modified Stoney equation [7, 8]. The tribological investigations were carried out using a CSM ball-on-disk tribometer. All samples were investigated at room temperature; the humidity was 27 ± 1 %. A wear track radius of 7 mm, a sliding distance of 300 m and a normal load of 5 N were chosen. The linear speed was 10 cm/s. 6-mm-diameter Al_2O_3 balls were used as counterparts. Following the ball-on-disk test, the resulting wear tracks were examined by optical profilometry using a Veeco Wyko NT1000 white light interferometer in vertical scanning interferometry mode. The surface roughness was determined using a NanoFocus µSurf confocal white light interferometer.

3. Results and Discussion

3.1 Process Optimization

The optimization of the cathode power and total pressure for the deposition process with the PM targets was done stepwise, starting at 4.5 kW per target through 6 up to 7 kW, while for each level the total pressure (i.e., the nitrogen partial pressure, since the argon flow was held constant) was varied. At cathode power levels of 4.5 and 6 kW, the increase of the cathode voltage versus deposition time was much more pronounced with less nitrogen, while more nitrogen resulted in a less marked increase. Additionally, the absolute values of the bipolarily pulsed cathode voltage decreased with increasing total pressure. Depla *et al.* observed such a decrease of the cathode voltage for nitrogen mole fractions lower than the critical one for target poisoning [9]. They attributed it to a modification of the plasma conditions, defined as the "gas or plasma effect". Thus, taking also into account the measured deposition rates (see below), we have to conclude that the selected nitrogen fractions are below the onset for target poisoning.

At 7 kW, only a slight increase of the cathode voltage versus time could be observed for a total pressure of 580 mPa. Also some arcs could be identified [10]. At 600 mPa, the cathode voltage was already constant versus time and at 620 mPa also no arcs could be detected anymore. Fig. 1(a) shows the cathode voltage of one representative cathode following the ramp to avoid overloading, versus time of the process run at a cathode power of 7 kW and a total pressure of 620 mPa. There, the process characteristics are comparable to the run with the mosaic targets (see Fig. 1(b)) with respect to the arcing behavior and the constant cathode voltage. However, it has to be mentioned that the average level of the cathode voltage is significantly higher for the PM targets compared to the mosaic targets. This can be explained by the different target types, where the copper backing plate might result in a higher average electrical conductivity of the mosaic targets.

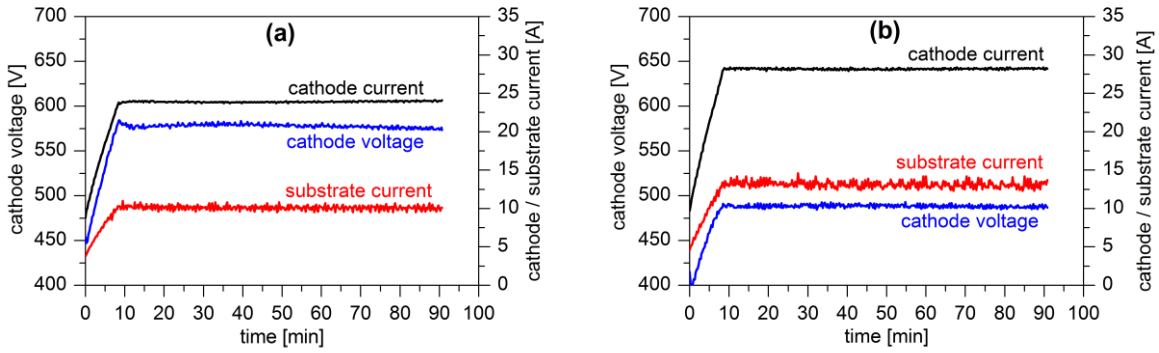

Fig. 1: Cathode voltage, cathode current and substrate current evolution for the (a) PM target process (cathode power: 7 kW, total pressure: 620 mPa, bias voltage: -40 V) and (b) the mosaic target process (cathode power: 7 kW, total pressure: 580 mPa, bias voltage: -50 V).

These stable conditions reached for the PM targets are also expressed by the evolution of the cathode current versus time (compare Figs. 1(a) and (b)). Due to the higher cathode voltage, significantly lower cathode current levels are obtained for the PM targets. Also a higher substrate current was found for the mosaic targets, as shown in Fig. 1, which can in part be explained by the higher bias voltage of the process applied for the mosaic targets. However, it should also be related to the by ~ 17 % higher cathode current [11], where the higher target ion flux density should also provide more ions being attracted by the substrate bias voltage.

The development of the deposition rate versus the total pressure is shown in Fig. 2. Basically, it can be seen that at constant cathode power the deposition rate slightly decreases with increasing total pressure. In general, such a smooth decrease in deposition rate at high total pressures, which corresponds to an increased nitrogen partial pressure in the sputtering system used, can be related to an increasing number of collisions and scattering effects of the

sputtered species [12]. Besides, it is obvious that the deposition rate determined for the mosaic target process is significantly lower than those obtained for the deposition runs with PM targets. The process, which was done with the PM targets at the same cathode power and total pressure, shows a ~ 60 % higher deposition rate. Even the deposition rate of the process optimized according to Fig. 1(a), which was run at an increased total pressure of 620 mPa, was ~ 44 % higher. The significantly higher deposition rate should be connected to a higher sputtering rate. As a result of the higher bias voltage used for the process with mosaic targets and the higher substrate current (see Fig. 1(b)), re-sputtering of film-forming species from the film surface might also play a role, reducing the deposition rate [13]. A contribution of collisions and scattering effects in the transport phase can be widely excluded since both deposition runs are done at the same total pressure [14].

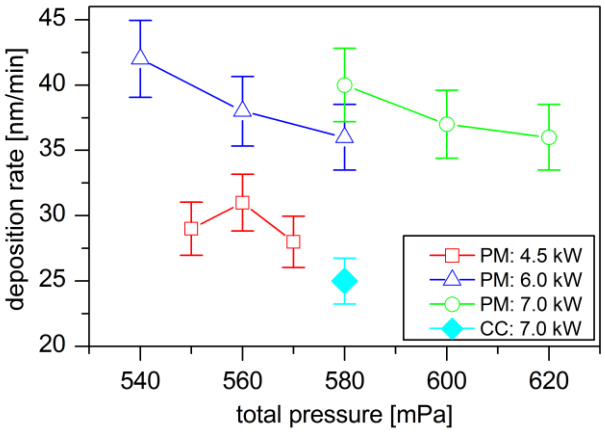

Fig. 2: Evolution of the deposition rate versus total pressure at different cathode powers for PM targets and for the process using the mosaic (CC) targets.

To illuminate contributions from the different sputtering behavior, the SRIM (Stopping and Range of Ions in Matter) code [15] was applied to calculate the sputtering yields for the different target materials as a function of ion energy. Assuming single-charged ions, their kinetic energy when bombarding the target surface corresponds to the difference between cathode voltage and plasma potential [16]. The values obtained by SRIM represent number and energy of the sputtered atoms leaving the target surface, but do not consider energy losses due to scattering processes and differences in adsorption at the substrate. At a cathode power of 7 kW, the argon/nitrogen partial pressure ratio variation done for the depositions with the PM targets corresponds to values between 70:30 and 60:40, while it was held constant for the mosaic targets at 60:40. To ensure comparison, the following calculations have been done for a constant argon/nitrogen pressure ratio of 60:40. The cathode voltage for the PM targets was in average -600 V during negative pulsing, while the cathode voltage for

the mosaic targets was approximately -500 V (see Fig. 1). Neglecting the plasma potential, the sputtering yield calculated for an ion energy of -500 eV is for Al ~ 37 % higher than for Ti; at -600 eV it is even 49 % higher (see Fig. 3). As the PM target has a composition of 60 at.-% Al and 40 at.-% Ti, it consists on a microscopic scale of an Al matrix with Ti grains embedded, while the mosaic target represents a Ti matrix with Al inserts. Thus, the significantly higher sputtering yield of Al can be assumed to be responsible for the higher deposition rate obtained for the PM targets, which overbalances the lower cathode current shown in Fig. 1. Furthermore, contributions from different secondary electron emission of Ti and Al, both in metallic and nitride state, might play a role.

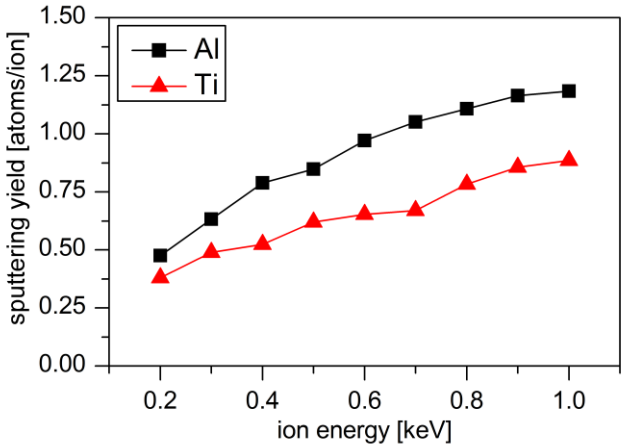

Fig. 3: Sputtering yield calculated by SRIM [15] as a function of the kinetic energy of a mixture of Ar/N ions of 60:40 sputtering Al and Ti targets.

3.2 Coating Microstructure

Those three coatings deposited at a cathode power of 7 kW from the PM targets were examined by EDX and had basically the same composition. They contained ~ 50 at.-% N, ~ 31.5 at.-% Al and ~ 18.5 at.-% Ti, corresponding to an Al/Ti atomic ratio of 63:37 and a composition of $Ti_{0.37}Al_{0.63}N$. The Al/Ti atomic ratio of the coatings is thus slightly higher than the target ratio, which is in agreement with earlier publications on sputtered $Ti_{1-x}Al_xN$ coatings [17, 18] and attributed to the higher sputtering yield of Al compared to Ti (see Fig. 3). The chemical composition of the coating grown with the mosaic targets was ~ 51 at.-% N, ~ 27.2 at.-% Al and ~ 21.4 at.-% Ti. Hence, the Al/Ti atomic ratio of this coating is 56:44 and the composition is $Ti_{0.44}Al_{0.56}N$. Establishing a correlation to the target composition is not possible due to the unknown effect of the arrangement of the Al inserts and the increasing erosion depth on the sputtering behavior. In summary, all investigated coatings showed compositions close to stoichiometry. The coatings deposited with the PM targets contain more Al than those

grown with the mosaic targets. This difference might be an effect of the higher cathode voltage of the PM targets (-600 V) compared to the mosaic targets (-500 V), which results according to Fig. 3 in preferred sputtering of Al compared to Ti atoms. The higher Al content might have a significant and positive effect on mechanical and tribological properties as well as on the oxidation behavior [3, 17].

Fig. 4 shows the XRD patterns of the coatings deposited at 7 kW using the PM targets at total pressures of 580, 600 and 620 mPa and by the process run with the mosaic targets, again at 7 kW and 580 mPa. The peak positions for face-centered cubic (fcc) TiN (JCPDS 00-038-1420) and fcc AlN (JCPDS 00-025-1495) are plotted as dashed lines. All coatings consist of the single-phase cubic $Ti_{1-x}Al_xN$ solid solution, as there are no peaks of the hexagonal phase [17]. For the coatings deposited from the PM targets, the intensity of the (111) peak derived from investigations in Bragg-Brentano geometry, increases with increasing total pressure. Comparing the pattern of the coating grown using the mosaic targets with those synthesized using the PM targets, it is evident that the (111) peak of the mosaic target process is less pronounced than for the PM processes, while the (200) peak is predominant. Furthermore, the peaks of the coating grown in the mosaic target process are slightly shifted to lower diffraction angles compared to the PM process. Such a peak shift to the left indicates compressive stress within the coating. Besides, the coating deposited in the mosaic target process contains less Al, which also explains the peak shift towards the TiN position [17, 19, 20]. The difference in microstructure evolution of the coatings deposited with PM targets or mosaic targets, respectively, can be attributed to the different target types and their different properties and, thus, to different growth conditions. These are strongly influenced by the substrate ion energy and the substrate ion/atom flux ratio. Petrov *et al.* [21] observed for $Ti_{0.5}Al_{0.5}N$ a change from (111) to (200) orientation by increasing one or both of these variables. This trend corresponds well to the findings described above, where the higher bias voltage and the higher substrate current observed for the mosaic compared to the PM target process, as already shown in Fig. 1, fosters growth in (200) direction.

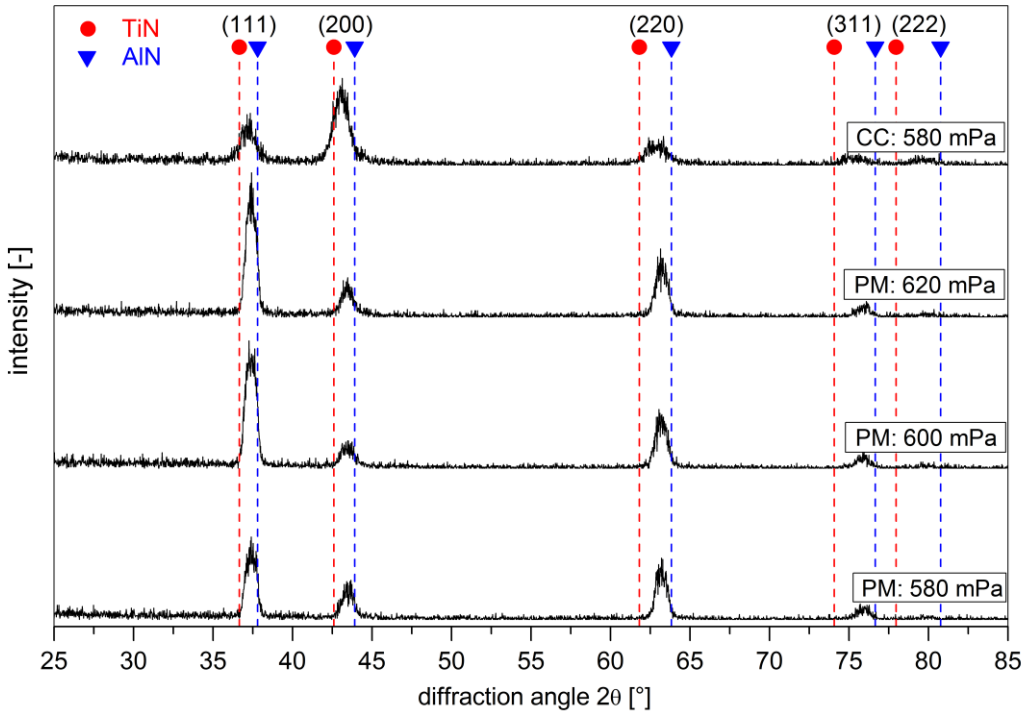

Fig. 4: GIXRD patterns of the coatings deposited using the PM targets at different total pressures and the process run with the mosaic (CC) targets. In all cases the cathode power was 7 kW.

Fig. 5 summarizes the domain sizes calculated by applying Pseudo-Voigt single-line analysis to the $Ti_{1-x}Al_xN$ peaks. Basically, it can be seen that with increasing total pressure the domain size decreases. For the coating grown using the mosaic targets the domain size was three times lower than for the coating deposited from the PM targets. This should again be related to the higher bias voltage and higher substrate current used for the mosaic targets and corresponds well to literature [22].

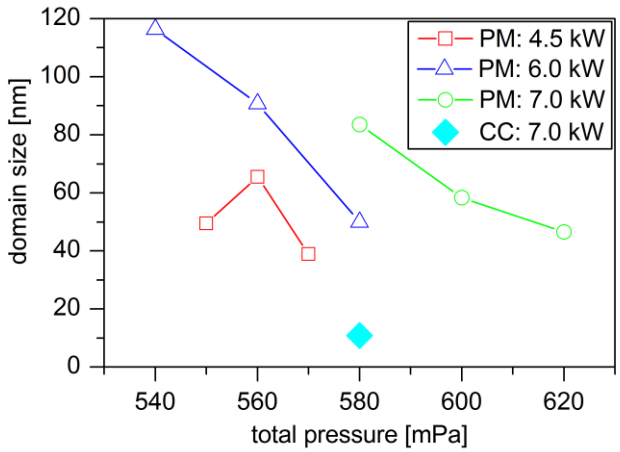

Fig. 5: Comparison of domain sizes obtained for the coatings grown at different cathode powers from the PM targets at different total pressures and the process run with the mosaic (CC) targets.

3.3 Coating Properties

The coating adhesion was excellent for all coatings deposited from the PM targets, as adhesion classes according to the VDI Rockwell C test between HF1 and HF3 could be obtained. No significant trends for the different total pressures used for deposition could be observed. The adhesion of the coatings deposited from mosaic targets was also excellent; an adhesion of class HF1 was found.

For the coatings deposited using the PM targets, tensile stresses in the range of 300 to 850 MPa were determined. For the coating grown from the mosaic targets, compressive stresses of -950 MPa were measured, corroborating the XRD peak shift observed in Fig. 4. The formation of these compressive stresses is caused by the higher bias voltage and substrate current used for the mosaic targets, which results in higher defect density and a densification of the coating microstructure [22]. Obviously, the lower substrate current observed for the PM targets (Fig. 1(a)) is not high enough to result in an ion peening effect sufficient for the generation of compressive stresses [23].

The values for hardness and Young's modulus were determined for the coatings of the 7 kW cathode power series deposited with the PM targets and for the mosaic target reference process. The hardness (Fig. 6(a)) as well as the Young's modulus (Fig. 6(b)) of the coatings deposited from the PM targets decrease slightly with increasing total pressure, although it has to be mentioned that the decrease is in the range of the standard deviation and, hence, probably not very significant. The highest hardness of 35.3 ± 1.5 GPa was measured for the

coating deposited in the process using the mosaic targets. According to Fig. 5, the domain size of the $Ti_{1-x}Al_xN$ phase is significantly smaller than that of the PM series coatings, which indicates that the Hall-Petch effect [2, 24] might play a role. Furthermore, as already mentioned, for the coating deposited from the mosaic targets, compressive residual stresses were determined, while for the PM coatings tensile stresses were detected. Coatings with compressive residual stresses commonly show increased hardness values compared to coatings with tensile stresses [2, 24-26]. Besides, the (111) orientation of TiN has been reported to show slightly lower hardness values than the (100) orientation [27], which might also contribute to the observed hardness difference.

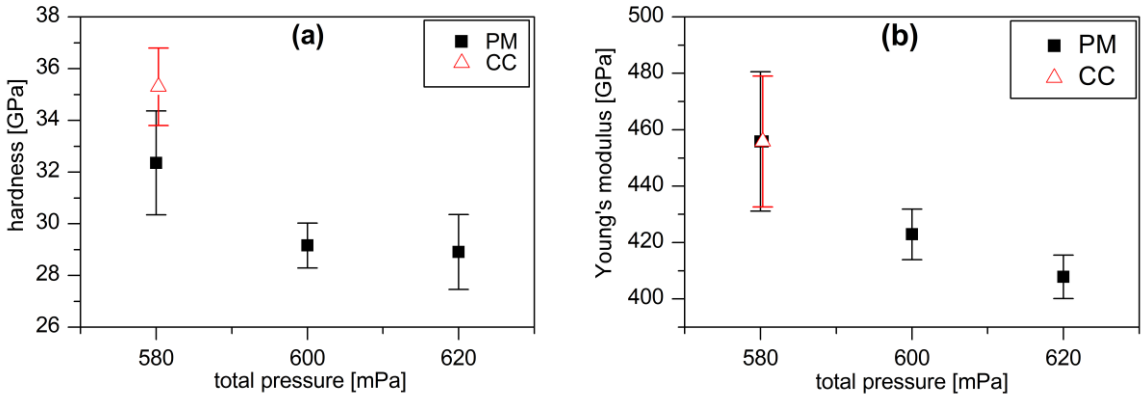

Fig. 6: Evolution of (a) hardness and (b) Young's modulus versus total pressure for the PM target processes run at 7 kW and the mosaic (CC) target process.

The friction coefficients summarized in Fig. 7(a) are the mean values and standard deviations determined by the CSM InstrumX software of the used tribometer. The friction coefficient shows a slight increase with total pressure for those coatings deposited from the PM targets. However, here it should be mentioned again that this increase is in the same range as its standard deviation and, thus, probably not very significant. The friction coefficient obtained for the coating deposited from the mosaic targets is slightly higher than those values obtained for the PM targets. The wear coefficients shown in Fig 7(b) increase with increasing total pressure for those coatings deposited using the PM targets, which agrees well to the observed hardness decrease (see Fig. 6(a)). The value obtained for the coating deposited from the mosaic targets is slightly higher than those obtained for the coatings grown from the PM targets. In general, both the friction and the wear coefficients correspond well to literature [17, 28-31].

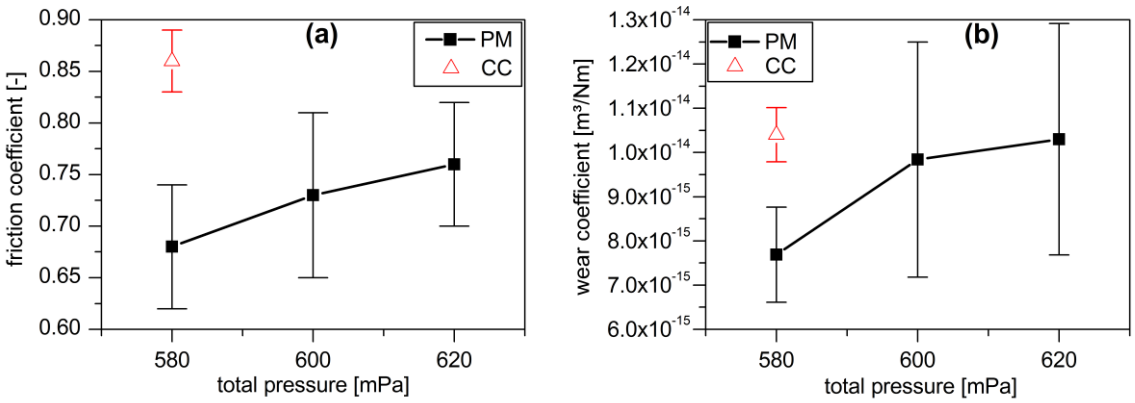

Fig. 7: Evolution of the (a) friction coefficient and (b) wear coefficient versus total pressure for the PM target processes run at 7 kW and the mosaic (CC) target process.

SEM micrographs of the surface of the coatings deposited from the PM targets at 7 kW and 620 mPa (Fig. 8(a)) and the mosaic targets at 7 kW and 580 mPa (Fig. 8(b)) were taken to further explain the differences in their tribological properties. Here it should be noted, that the thicknesses of both coatings are quite comparable (3.2 µm for the PM and 3.7 µm for the mosaic target coating). Fig. 8 shows that the surface of the coating deposited from the PM targets is rougher (Ra = 100 nm) than the one of the coating deposited from the mosaic targets (Ra = 17 nm). This can be explained by the higher bias voltage and higher substrate current used for the process run with the mosaic targets. Both result in more and higher energetic ions bombarding the film surface which in turn is well known to result in smaller domain sizes (see Fig. 5 and refs. [22, 32]). The slightly worse tribological behavior of the coating deposited from the mosaic targets may be related to the smoother surface and thus, the larger real contact area between coating and counterpart [33, 34].

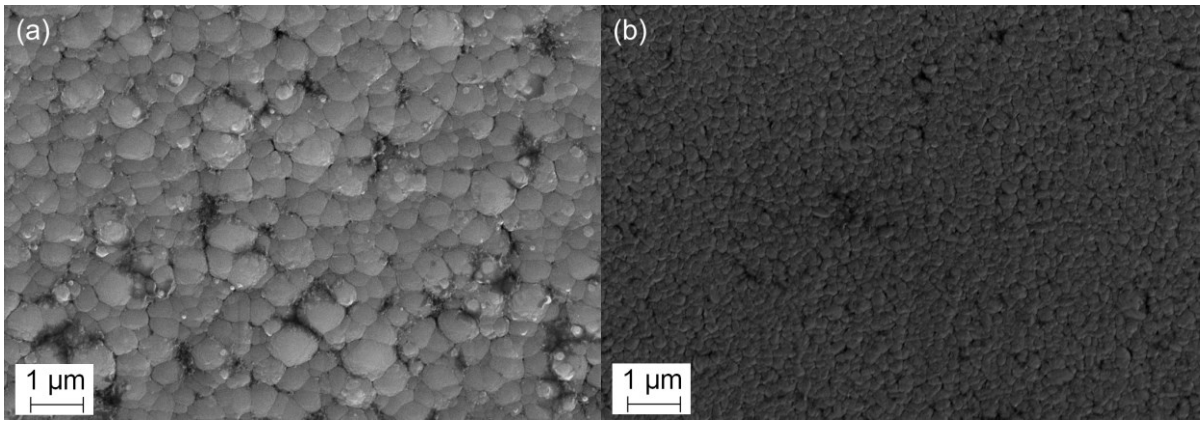

Fig. 8: SEM micrograph of the surface of (a) the coating deposited with the PM targets (cathode power: 7 kW, total pressure: 620 mPa) and (b) the coating deposited with the mosaic targets (cathode power: 7 kW, total pressure: 580 mPa).

4. Conclusions

$Ti_{1-x}Al_xN$ coatings were deposited on high-speed steel and silicon (100) substrates from two different types of targets, i.e. powder metallurgically prepared compound as well as mosaic TiAl targets, to elucidate the effect of different target types on deposition as well as structure and properties of the coatings. After optimization of cathode power and nitrogen partial pressure, the deposition rate obtained with the compound targets was ~ 44 % higher than for the mosaic targets, which is explained by the higher sputtering yield of the aluminum matrix of the compound targets compared to the titanium matrix of the mosaic targets.

All coatings showed a single-phase cubic $Ti_{1-x}Al_xN$ solid solution, with slightly lower aluminum content for the coatings deposited from the mosaic targets. A more pronounced (200) orientation of the $Ti_{1-x}Al_xN$ phase was found for the coatings grown from the mosaic targets, whereas those coatings deposited from the compound targets exhibit a (111) preferred orientation. The hardness of the coating deposited with the mosaic targets was slightly higher than that of the coatings synthesized with the compound targets, which is directly related to its lower domain size and to the change in preferred orientation. While for the coating deposited with the mosaic targets compressive stresses were determined, tensile stresses were obtained for the coatings grown from the compound targets. The differences in preferred orientation, domain size and stress could be related to the higher bias voltage and considerably higher substrate ion current used for the mosaic targets process. However, both the friction coefficients and the wear coefficients were slightly lower for the coatings deposited with the compound targets.

In summary, it could be shown that using compound TiAl targets manufactured by powder metallurgy, $Ti_{1-x}Al_xN$ coatings with mechanical and tribological properties comparable to those grown from commercially applied mosaic targets can be deposited at significantly higher growth rates.

Acknowledgements

Paul J. Rudnik (PLANSEE USA LLC) is acknowledged for helpful discussions on sputter deposition of PM targets. This work was done within the Research Studio Austria Surface Engineering, with financial support from the Österreichische Forschungsförderungsgesellschaft mbH and the Bundesministerium für Wirtschaft, Familie und Jugend. Part of this work was also supported by the Austrian Federal Government (in particular from the Bundesministerium

für Verkehr, Innovation und Technologie and the Bundesministerium für Wirtschaft, Familie und Jugend) and the Styrian Provincial Government, represented by Österreichische Forschungsförderungsgesellschaft mbH and by Steirische Wirtschaftsförderungsgesellschaft mbH, within the research activities of the K2 Competence Centre on "Integrated Research in Materials, Processing and Product Engineering", operated by the Materials Center Leoben Forschung GmbH in the framework of the Austrian COMET Competence Centre Programme.

References

[1] K. Bobzin, N. Bagcivan, P. Immich, S. Bolz, R. Cremer, T. Leyendecker, Thin Solid Films 517 (2008) 1251-1256.

[2] P.H. Mayrhofer, C. Mitterer, L. Hultman, H. Clemens, Progr. Mater. Sci. 51 (2006) 1032-1114.

[3] S. PalDey, S.C. Deevi, Mater. Sci. Eng. A 342 (2003) 58-79.

[4] D. Rafaja, T. Merkewitz, C. Polzer, V. Klemm, G. Schreiber, P. Polcik, M. Kathrein, 17th Plansee Seminar 2 (2009) HM38.

[5] Th.H. De Keijser, J.I. Langford, E.J. Mittemeijer, A.B.P. Vogels, J. Appl. Cryst. 15 (1982) 308-314.

[6] H.-R. Stock, A. Schulz, W. Ensinger, J. Güttler, E. Fromm, D. Müller, W.D. Busch, H. Grützner, in: H. Jehn, G. Reiners, N. Siegel (Eds.), DIN-Fachbericht 39: Charakterisierung dünner Schichten, 1. Auflage, Beuth Verlag, Berlin, 1993, pp 212-213.

[7] G.G. Stoney, Proc. R. Soc. Lond. A 82 (1909) 172-175.

[8] G.C.A.M. Janssen, M.M. Abdalla, F. van Keulen, B.R. Pujada, B. van Venrooy, Thin Solid Films 517 (2009) 1858-1867.

[9] D. Depla. A. Colpaert, K. Eufinger, A. Segers, J. Haemers, R. De Gryse, Vacuum 66 (2002) 9-17.

[10] C. Mitterer, O. Heuzè, V.-H. Derflinger, Surf. Coat. Technol. 89 (1997) 233-238.

[11] C. Mitterer, P.H. Mayrhofer, E. Kelesoglu, R. Wiedemann, H. Oettel, Z. Metallkde. 90 (1999) 602-607.

[12] R. Wuherer, W.Y. Yeung, Scripta Mater. 50 (2004) 1461-1466.

[13] I. Petrov, L. Hultman, J.-E. Sundgren, J.E. Greene, J. Vac. Sci. Technol. A 10 (1992) 265-272.

[14] I. Petrov, W. Orlinov, I. Ivanov, J. Kourtev, Contrib. Plasma Phys. 28 (1988) 265-273.

[15] J.F. Ziegler, M.D. Ziegler, J.P. Biersack, SRIM – The Stopping and Range of Ions in Matter, version SRIM-2008.04, www.SRIM.org.

[16] I. Petrov, F. Adibi, J.E. Greene, W.D. Sproul, W.-D. Münz, J. Vac. Sci. Technol. A 10 (1992) 3283-3287.

[17] K. Kutschej, P.H. Mayrhofer, M. Kathrein, P. Polcik, R. Tessadri, C. Mitterer, Surf. Coat. Technol. 200 (2005) 2358-2365.

[18] J.Y. Rauch, Ch. Rousselot, N. Martin, Ch. Jacquot, J. Takadoum, J. Eur. Ceram. Soc. 20 (2000) 795-799.

[19] W.D. Münz, J. Vac. Sci. Technol. A4 (6) (1986) 2717-2725..

[20] A. Kimura, H. Hasegawa, K. Yamada, T. Suzuki, Surf. Coat. Technol. 120-121 (1999) 438-441.

[21] I. Petrov, F. Adibi, J.E. Greene, L. Hultman, J.-E. Sundgren, Appl. Phys. Lett. 63 (1993) 36-38.

[22] I. Petrov, P.B. Barna, L. Hultman, J.E. Greene, J. Vac. Sci. Technol. A 21 (2003) 117–128.

[23] R. Daniel, K.J. Martinschitz, J. Keckes, C. Mitterer, Acta Mater. 58 (2010) 2621-2633.

[24] P.H. Mayrhofer, C. Mitterer, J. Musil, Surf. Coat. Technol. 174-175 (2003) 725-731.

[25] P.H. Mayrhofer, F. Kunc, J. Musil, C. Mitterer, Thin Solid Films 415 (2002) 151-159.

[26] P.H. Mayrhofer, G. Tischler, C. Mitterer, Surf. Coat. Technol. 142-144 (2001) 78-84.

[27] K. Kutschej, B. Rashkova, J. Shen, D. Edwards, C. Mitterer, G. Dehm, Thin Solid Films 516 (2007) 369.

[28] S.-Y. Yoon, J.-K. Kim, K.H. Kim, Surf. Coat. Technol. 161 (2002) 237-242.

[29] K. Katahira, Y. Watanabe, H. Ohmori, T. Kato, Int. J. Mach. Tools Manuf. 42 (2002) 1307-1313.

[30] J.L. Mo, M.H. Zhu, B. Lei, Y.X. Leng, N. Huang, Wear 263 (2007) 1423-1429.

[31] W. Grzesik, Z. Zalisz, S. Krol, P. Nieslony, Wear 261 (2006) 1191-1200.

[32] D.S. Rickerby, P.J. Burnett, Thin Solid Films 157 (1988) 195-222.

[33] K. Holmberg, A. Matthews, H. Ronkainen, Tribol. Int. 31 (1998) 107-120.

[34] B. Bhushan, Principles and Applications of Tribology, John Wiley & Sons, New York, 1999.

Publication II

Influence of residual stresses and grain size on the spinodal decomposition of metastable $Ti_{1-x}Al_xN$ coatings

N. Schalk, C. Mitterer, J. Keckes, M. Penoy, C. Michotte

Surface and Coatings Technology 209 (2012) 190-196

Influence of residual stresses and grain size on the spinodal decomposition of metastable $Ti_{1-x}Al_xN$ coatings

N. Schalk[a,*], C. Mitterer[b], J. Keckes[c], M. Penoy[d], C. Michotte[d]

[a] *Materials Center Leoben Forschung GmbH, Roseggerstrasse 12, A-8700 Leoben, Austria*

[b] *Department of Physical Metallurgy and Materials Testing, Montanuniversität Leoben, Franz-Josef-Strasse 18, A-8700 Leoben, Austria*

[c] *Department of Materials Physics, Montanuniversität Leoben, Jahnstrasse 12, A-8700 Leoben, Austria*

[d] *CERATIZIT Luxembourg S.àr.l., Route de Holzem, B.P.51, L-8201 Mamer, Luxembourg*

Abstract

At elevated temperatures, the metastable $Ti_{1-x}Al_xN$ solid solution decomposes in cubic AlN and cubic TiN. Within this work, the effect of residual stresses on the decomposition of sputtered $Ti_{1-x}Al_xN$ coatings was investigated. Using different bias voltages, a series of $Ti_{1-x}Al_xN$ coatings (x = 0.63) with stresses ranging from +630 to -2500 MPa was synthesized on Si (100) substrates. Vacuum annealing treatments and subsequent X-ray diffraction measurements showed that tensile stresses foster the formation of more volume consuming cubic TiN domains, while compressive stresses promote the formation of smaller cubic AlN domains. The influence of the grain size has been considered by investigations of free standing films using differential scanning calorimetry. Smaller grains lead to faster decomposition and earlier precipitation of wurtzite AlN.

Keywords: sputtering, $Ti_{1-x}Al_xN$ coatings, residual stresses, spinodal decomposition, grain size

1. Introduction

Metastable $Ti_{1-x}Al_xN$ coatings are widely used as hard and wear protective coatings in different machining applications. The formation of metastable $Ti_{1-x}Al_xN$ is based on the substitution of Ti by Al atoms in the fcc-TiN lattice. Single-phase cubic $Ti_{1-x}Al_xN$ is formed up to Al contents of x ~ 0.67. Higher Al contents lead to dual-phase coatings followed by a single-phase wurtzite structure, where the Ti atoms substitute for Al atoms in the wurtzite (w) AlN lattice [1-5]. Within the cubic regime increasing Al contents lead to enhanced coating properties, like higher hardness and oxidation resistance. When the wurtzite structure is formed, these properties deteriorate [3-5].

During annealing, the metastable fcc-$Ti_{1-x}Al_xN$ solid solution decomposes into fcc-TiN and fcc-AlN domains. This behavior, known as spinodal decomposition, leads to age hardening due to coherency strains between the matrix and the formed small coherent domains. If the temperature is further increased, the metastable fcc-AlN transforms into the stable w-AlN, resulting in a hardness loss [3, 4, 6].

It has been reported that the decomposition of metastable fcc-$Ti_{1-x}Al_xN$ is not only influenced by the chemical driving force but also by the elastic strain energy and the surface energy [7]. The chemical contribution has been comprehensively investigated [3, 4, 6-9] and there are several reports available dealing with the contribution of strain [7, 10-12] and compressive stress formation [13]. However, all coatings discussed in literature exhibit compressive residual stresses in the as-deposited state. Within the present work, sputtered $Ti_{1-x}Al_xN$ coatings with tensile as well as compressive residual stresses could successfully be synthesized by using different bias voltages. To illuminate the influence of the as-deposited residual stresses on the spinodal decomposition in detail, vacuum annealing treatments and subsequent X-ray diffraction measurements were conducted as well as differential scanning calorimetry investigations, where attention was also paid to the effect of the grain size of the obtained coatings.

2. Experimental Details

Five $Ti_{1-x}Al_xN$ coatings were deposited using an industrial scale CemeCon CC800/9MLT unbalanced magnetron sputtering system equipped with four powder metallurgically produced compound targets (PLANSEE Composite Materials, Germany) with a target composition of 40 at.% Ti and 60 at.% Al. A 30 min Ar^+ ion etching step was implemented prior to the depo-

sition process to clean the substrates. More detailed information on the etching process can be found in ref. [14]. During deposition, the magnetrons were bipolarily pulsed at a frequency of 35 kHz and a duty cycle of 50 %. The power was set to 7 kW per target. An asymmetric bipolarily pulsed d.c. bias voltage of -40, -50, -60, -70 and -80 V, respectively, was applied to synthesize the five different coatings. The coatings were deposited in a mixed Ar/N_2 atmosphere, where the Ar flow was held constant at 230 sccm and the process-controlled total pressure was 620 mPa. The substrate temperature was ~550 °C and the deposition time 1.5 h.

Two different substrates types were used; Si (100) platelets with the dimensions 7 x 21 x 0.5 mm^3 and mild steel foil with a thickness of 50 µm. The coated Si samples were used for coating characterization and annealing treatments. The mild steel foil was removed chemically in 10 mol.% nitric acid in order to gain a powdered coating, which was used for differential scanning calorimetric and X-ray diffraction measurements.

The coating thickness was determined by the ball-crater-technique using a CSM CaloTest. The chemical composition was investigated by means of glow discharge optical emission spectroscopy (GDOES) utilizing a Horiba Jobin-Yvon JY10000RF spectroscope. For the investigation of the crystallographic structure, a Bruker-AXS D8 Advance diffractometer was used. The X-ray diffraction (XRD) measurements were performed in Bragg-Brentano as well as in grazing incidence (GI) geometry (incidence angle 2°). To obtain information about the microstrain and the size of coherently diffracting domains, the Pseudo-Voigt function [15] was applied to all cubic peaks of the XRD patterns obtained in Bragg-Brentano geometry from the powdered samples in the measured range between 20 and 85°. Subsequently, the gained data was analyzed using the Williamson-Hall method [16]. The residual stresses were determined using the $\sin^2\psi$ method [17] utilizing a Seifert PTS-3000 diffractometer equipped with polycapillary primary optics, long Soller slits, secondary graphite monochromator and scintillation counter. Because the X-ray elastic constants (XECs) of $Ti_{1-x}Al_xN$ phases are not known, XECs of TiN [18] were used to calculate the residual stresses from the measured X-ray elastic strains. Since the XECs of $Ti_{1-x}Al_xN$ may differ from those of TiN, the stress magnitudes obtained for the different coatings demonstrate the relative differences in stresses but are only approximate on the absolute scale.

The annealing treatments were conducted in a vacuum furnace (HTM Reetz, base pressure < $5x10^{-4}$ Pa), starting at 700 °C in 50 °C steps up to 1000 °C, using a heating rate of 20 K/min, a holding time of 15 min and a cooling rate of 60 K/min. After each annealing step, the crystallographic structure of the coatings was ex-situ investigated using XRD. The (200) peak of all coatings was investigated in more detail at all annealing temperatures by applying the

Pseudo-Voigt function, in order to be able to observe any asymmetric peak broadening or formation of shoulders and thus, the onset of spinodal decomposition. Further, the cubic lattice parameter of all coatings for all annealing temperatures was calculated from the (200) fcc-$Ti_{1-x}Al_xN$ peak.

A Setaram Labsys EVO differential scanning calorimeter (DSC) was used to detect the microstructural changes in the powdered coatings during heating. As a first step, a powdered sample of every coating was heated in Ar atmosphere up to 1500 °C; the heating rate was 23 K/min and the cooling rate 50 K/min. To get a better understanding of the different partial reactions that take place, three further powder samples of every coating were annealed up to 900, 1150 and 1350 °C, respectively, in the DSC. Subsequently, the samples were investigated using XRD and compared to each other as well as to the as-deposited sample and the sample heated to 1500 °C. A virgin sample with ~30 mg mass was used for every measurement.

The coating hardness was determined using a UMIS (Ultra Micro Indentation System) Nanoindenter from Fischer-Cripps Laboratories, equipped with a Berkovich tip. A plateau test was conducted, where the load was decreased from a maximum load of 30 mN in increments of 2 mN to a minimum load of 2 mN.

3. Results and Discussion

The coating thickness was ~3 µm for all coatings; there was no detectable difference of the growth rate for the coatings deposited using different bias voltages. Also the chemical composition was the same for all coatings. They contained 18 at.% Ti, 31 at.% Al and 51 at.% N, which corresponds to an Al/Ti atomic ratio of 63/37. Thus, the Al content is slightly higher in the coating than in the target, which is in good agreement with literature [5, 19]. In Fig. 1a and b, the GI-XRD patterns of the coatings deposited using -40 and -80 V bias voltage, respectively, are shown with annealing temperature increasing from bottom to top. The respective patterns at the bottom belong to the as-deposited coatings. There, it can be seen that both coatings consist of a single-phase fcc $Ti_{1-x}Al_xN$ solid solution in the as-deposited state. In Fig. 1b, a pronounced peak at a slightly lower diffraction angle (~33°) than the position of w-AlN can be identified; this is an additional Si peak originating from the substrate which appears also in some other patterns shown in Fig. 1a and b. By comparing the two patterns of the as-deposited coatings, it can be seen that the peaks of the coating deposited at -80 V bias voltage are much lower and broader than the ones of the coating grown at -40 V bias voltage. Such a peak broadening indicates a smaller domain size and/or a larger mi-

crostrain, since the higher bias voltage results in more and higher energetic ions bombarding the film surface, which usually causes a smaller domain size and/or larger microstrain [20].

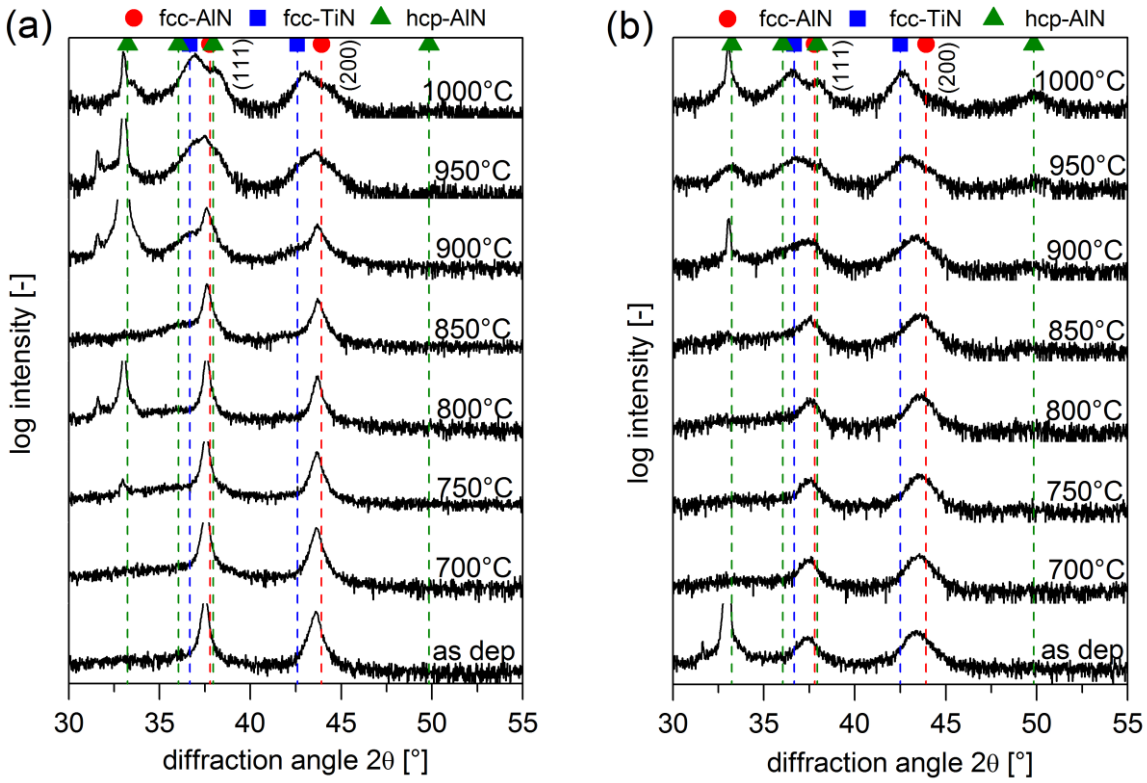

Fig. 1: XRD patterns of the coatings deposited at (a) -40 V bias voltage, showing tensile residual stresses and (b) -80 V bias voltage, showing compressive stresses for the as-deposited state and after different annealing temperatures.

In order to qualitatively assess the bias-voltage-induced relative changes of domain size and microstrain in the films, Williamson-Hall (WH) plot [21] analysis was performed on powder samples characterized in Bragg-Brentano geometry (Fig. 2). According to the assumptions from ref. [16, 21], it was supposed for simplicity that the domain size broadening does not depend on the diffraction vector length $|d^*|$ and the strain broadening does [21]. In that case the intercept on the β^* axis (of total integral breadth in the reciprocal space) corresponds usually to the inverse domain size $1/D$, whereby the microstrain is proportional to the WH plot slope (Fig. 2). The slopes $\partial\beta^* / \partial d^*$ in Fig. 2 unambiguously indicate that with increasing bias voltage the microstrain increases in the $Ti_{1-x}Al_xN$ coatings. This qualitative result documents that the higher bias voltages, with more intensive ion peening effect, result in a more pronounced formation of strains of II and III order, caused usually by nanoscale crystallographic defects. The domain size analysis in Fig. 2 results in very large unrealistic values and becomes even negative. This phenomenon can be interpreted by the known effect of partial coherence in nanocrystalline thin films reported by Rafaja et al. [22, 23]

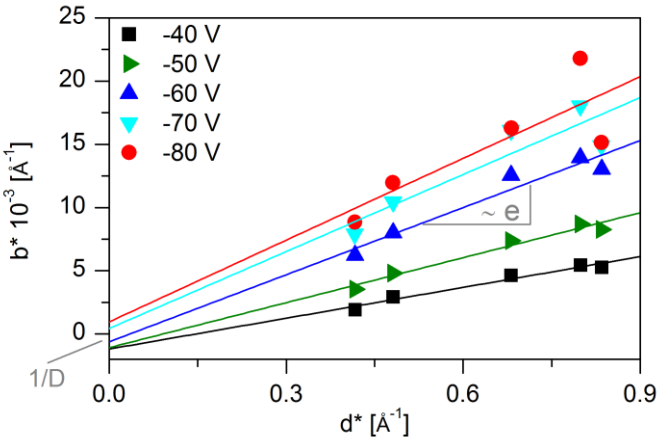

Fig. 2: Williamson-Hall plot for coatings grown at different bias voltages indicating qualitatively a decreasing domain size D and an increasing microstrain e with increasing bias voltage.

Fig. 3 indicates that the coatings deposited at bias voltages of -40 and -50 V exhibit tensile stresses, while the coatings grown at higher bias voltages show compressive stresses. Here, it has to be mentioned that the higher bias voltage also results in an increasing substrate current. Apparently, the substrate currents obtained for the coatings deposited at low bias voltages are too low to cause an ion peening effect sufficient to generate compressive stresses [24].

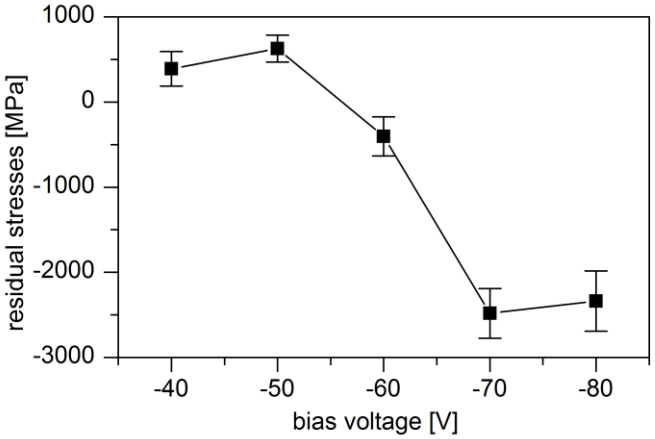

Fig. 3: Evolution of the residual stresses as a function of the bias voltage.

In addition to the GI-XRD patterns of the -40 V bias coating having tensile as-deposited stresses and the -80 V bias coating having compressive stresses, Fig. 1 shows GI-XRD patterns of these coatings annealed at different temperatures. For the coating with tensile stresses (Fig. 1a), no major changes can be identified up to ~800 °C. However, after annealing at 850 °C there is a shoulder visible on the left hand side of the $Ti_{1-x}Al_xN$ peak and also a small w-AlN peak can be observed. For the coating with compressive stresses (Fig. 1b), also a w-AlN peak can be identified after annealing at 850 °C. In addition, after annealing at 950 °C

a shoulder is evident, which is formed - in contrast to the -40 V sample - on the right hand side of the $Ti_{1-x}Al_xN$ peak. Further, it has to be noted that for the coating with compressive stresses (Fig. 1b) there is much more w-AlN present after annealing at 1000 °C than for the coating with tensile stresses (Fig. 1a); there are already peaks at higher diffraction angles visible.

To investigate the spinodal decomposition in more detail, the (200) peak was subjected to peak fitting using the Pseudo-Voigt function. In Fig. 4 the peaks of the coating with tensile (left) and compressive stresses (right) are shown, from bottom to top with increasing annealing temperature. 800 °C was chosen as first temperature, because after annealing to this temperature both coatings still do not show any evidence of spinodal decomposition. After annealing to 850 °C, the coating with the tensile stresses shows a small shoulder on the left hand side of the $Ti_{1-x}Al_xN$ peak. This indicates that for this coating the spinodal decomposition starts with formation of fcc-TiN domains. On the other hand, the coating with compressive stresses does not show any apparent sign of spinodal decomposition. After annealing to 900 °C, the shoulder on the left hand side of the $Ti_{1-x}Al_xN$ peak is more pronounced for the coating with the tensile stresses, but there is still no sign of spinodal decomposition visible for the coating with the compressive stresses. After annealing to 950 °C, there are distinct shoulders visible on both sides of the peak for the coating with tensile stresses. For the coating with compressive stresses, there is a shoulder recognizable; however, this shoulder is on the right hand side of the peak, which means that for this coating the decomposition starts with the formation of fcc-AlN domains. The different decomposition behavior can be explained by the fact, that fcc-TiN domains are more volume consuming than the fcc-$Ti_{1-x}Al_xN$ matrix, while fcc-AlN domains are smaller [6, 25]. Consequently, fcc-TiN domains form first in coatings with tensile stresses, while compressive stresses foster the formation of fcc-AlN domains. After annealing to 1000 °C, the $Ti_{1-x}Al_xN$ peak of the coating with the tensile stresses is clearly shifted to the left and there is a pronounced fcc-AlN shoulder visible. For the coating with the compressive stresses, the $Ti_{1-x}Al_xN$ peak is even more shifted to the left and there is only a very small fcc-AlN shoulder visible. The reason for this is, as already mentioned, that for the coating with the compressive stresses there is already a significant fraction of w-AlN present after annealing to 1000 °C (Fig. 1).

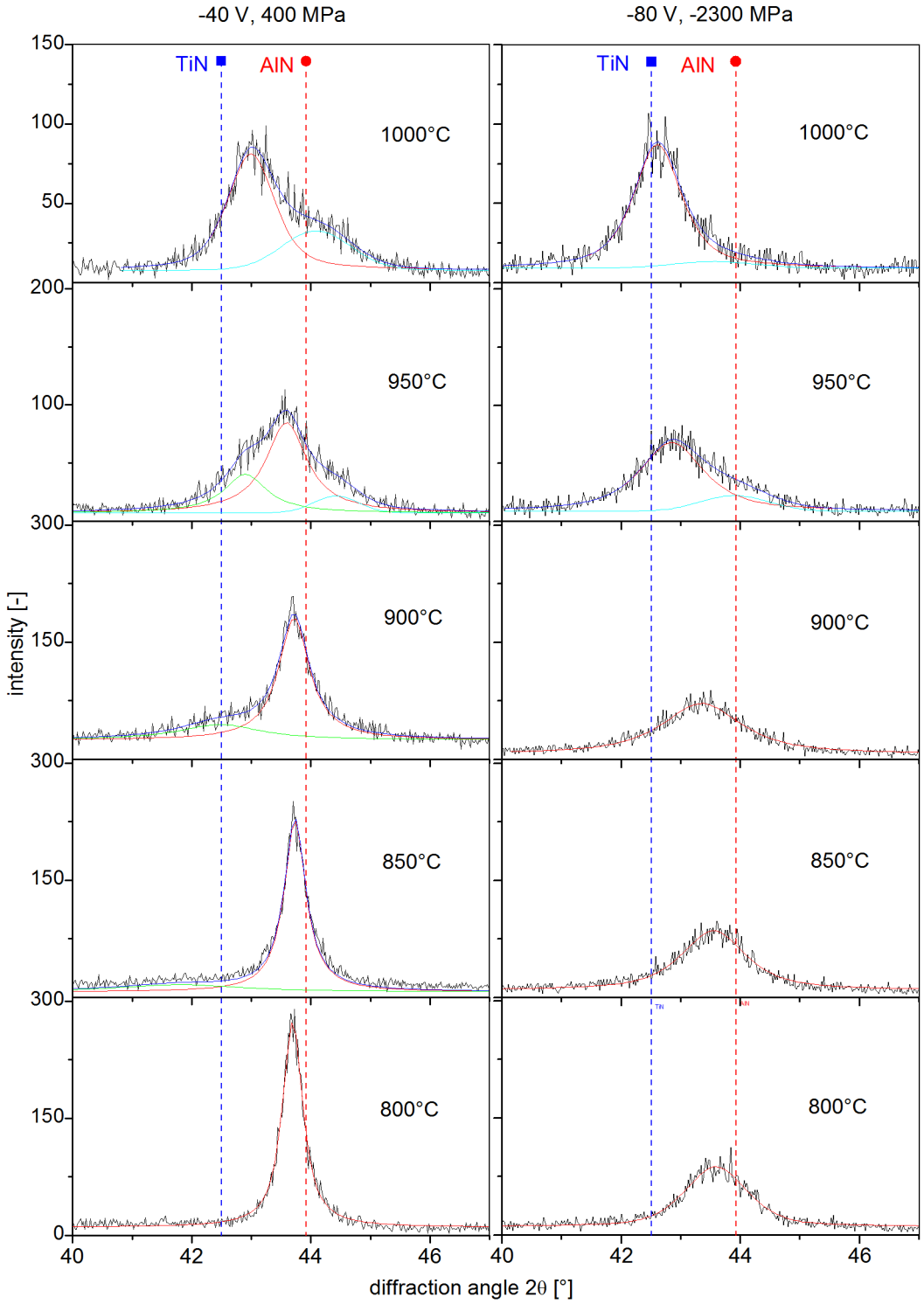

Fig. 4: Development of the (200) XRD peak with increasing temperature for a coating with tensile (left) and one with compressive residual stresses (right). The peaks were fitted using the Pseudo-Voigt function.

The out-of-plane lattice parameters of the cubic phase for all coatings and annealing temperatures are shown in Fig. 5. Additionally, the theoretical values of fcc-TiN [26], fcc-AlN [27] and the lattice parameter of $Ti_{0,37}Al_{0,63}N$ calculated assuming a Vegard-like behavior are indi-

cated. It can be seen that in the as-deposited state the lattice parameter increases with increasing bias voltage. The lattice parameter of the coatings with tensile stresses is lower than the theoretical one, while that of the coatings with compressive stresses is higher. That fits very well considering that compressive stresses result in a peak shift to lower diffraction angles in the XRD pattern, which consequently results in a larger lattice parameter of crystallographic planes oriented parallel to the substrate surface. With increasing annealing temperature, the lattice parameters slightly decrease and finally reach their minimum. According to Rachbauer *et al.* [10] this decrease of the lattice parameter cannot only be attributed to defect annihilation and recovery processes, but also to the starting spinodal decomposition and the accompanying development of microstrains. They found a strain increase of ~60 % for the annealed coatings compared to the as-deposited ones at the temperature, where the lattice parameter is at its minimum. This is also in agreement with the results from ref. [13], where at early stages of the spinodal decomposition the annealing results in the formation of tensile macrostrains and the out-of-plane lattice parameter decreases. Consequently the formation of fcc-TiN- and fcc-AlN-rich domains can be assumed to start already at lower temperatures than visible in the XRD patterns (Fig. 1 and Fig. 4).

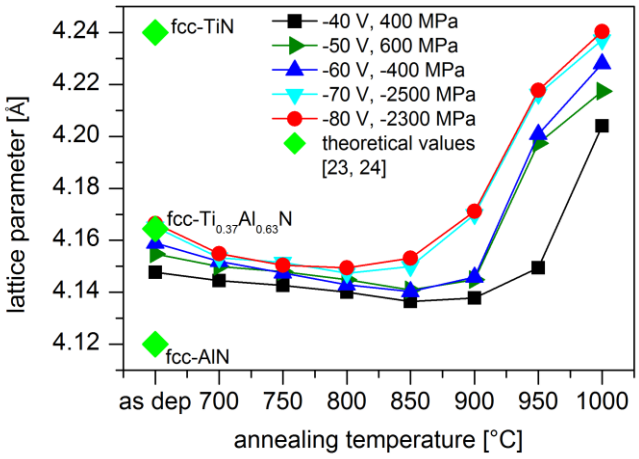

Fig. 5: Lattice parameter of the fcc-$Ti_{1-x}Al_xN$ phase for the coatings deposited on Si substrate using different bias voltages obtained from the XRD patters of the as-deposited sample and after annealing to different temperatures.

At about 850 °C, the lattice parameters start to increase. This increase is steeper for the coatings with compressive as-deposited residual stresses than for the coatings with tensile stresses. According to Fig. 4, fcc-TiN domains form first for the coatings with tensile stresses, as they are more volume consuming than the $Ti_{1-x}Al_xN$ matrix. It can be assumed that the low tensile stresses turn now into compressive [13], which slows down the following decomposition. On the other hand, smaller fcc-AlN domains form first for the coatings with compressive as-deposited residual stresses (Fig. 4). It can be assumed that tensile areas appear

around these fcc-AlN domains, fostering the following decomposition. However, the formation of these fcc-TiN and fcc-AlN domains is also superimposed by the precipitation of w-AlN, which starts when the lattice parameter is at its minimum [10]. According to Fig. 5 that is the case at about 800 – 850 °C, which is in good agreement with the first appearance of the w-AlN peak in the XRD patterns shown in Fig. 1. Besides, more w-AlN could be observed at lower temperatures for the coating with the compressive as-deposited stresses (Fig. 1). An explanation for this can be found in the fact that the lattice parameter of the coating with tensile stresses is closer to the value of fcc-AlN than that of the coating with compressive stresses (Fig. 5). This means that for the coating with compressive stresses the coherency strain and consequently the driving force for precipitation of w-AlN is higher than for the coating with the tensile stresses.

In Fig. 6 the heat flow as a function of the sample temperature is shown for all coatings. At lower temperatures the heat flows of the different coatings are quite similar, but above ~900 °C there are differences. Especially the last peak, which is very pronounced for the coatings with tensile stresses, is much less distinct for the coatings with compressive stresses. To investigate the different partial reactions and differences between the coatings in more detail, three further powder samples of every coating were annealed to 900, 1150 and 1350 °C and subsequently investigated using XRD.

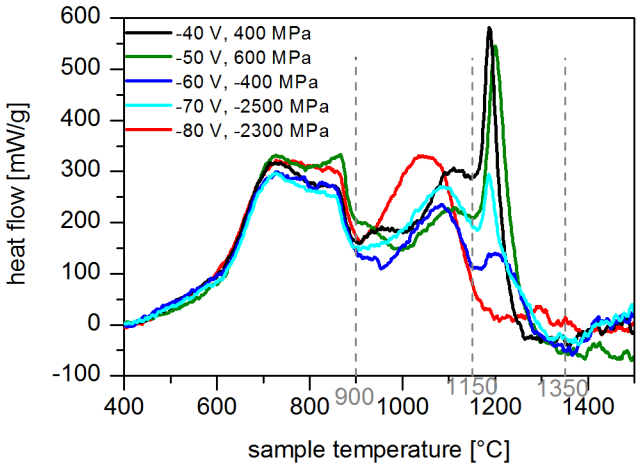

Fig. 6: Heat flow measured during DSC of $Ti_{1-x}Al_xN$. Three further powder samples of every coating were annealed in the DSC to the temperatures denoted in the diagram.

The GI-XRD patterns of the powder before and after annealing in the DSC to 900, 1150, 1350 and 1500 °C, respectively, are shown in Fig. 7 from bottom to top. Fig. 7a and b present the patterns of the coatings with tensile and compressive as-deposited stresses, respectively. Before annealing, both coatings consist of a single phase cubic $Ti_{1-x}Al_xN$ solid solution. After annealing to 900 °C, the pattern of the coating with tensile stresses (Fig. 7a) shows a pronounced shoulder on the left hand side of the $Ti_{1-x}Al_xN$ peak. After annealing to 1150 °C,

there is a shoulder on the right hand side of the $Ti_{1-x}Al_xN$ peak and for the first time a w-AlN peak is visible. After annealing to 1350 °C, there is no fcc-AlN left. For the coating with the compressive stresses (Fig. 7b), there is a small shoulder on the left hand side of the $Ti_{1-x}Al_xN$ peak visible after annealing to 900 °C, and also a w-AlN peak can already be identified. After annealing to 1150 °C, a small shoulder on the right hand side of the $Ti_{1-x}Al_xN$ peak can be observed and after 1350 °C no fcc-AlN is left. Annealing to 1500 °C leads just to sharper peaks for both coatings. However, it has to be considered that for the DSC measurements the coatings were chemically removed from substrates and thus only the intrinsic stresses of second and third order are left. Hence, it can be assumed that the high compressive stresses have relaxed, which explains the differences between these patterns and the ones shown in Fig. 1.

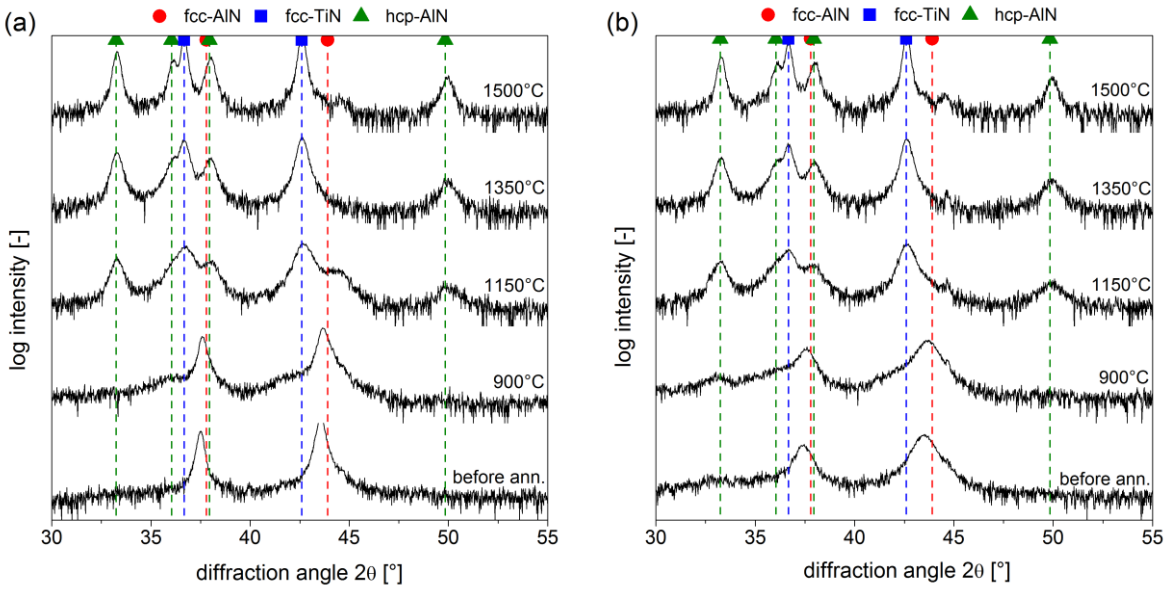

Fig. 7: XRD patterns of the powdered samples before and after annealing in the DSC to different temperatures (a) of the coating deposited at -40 V bias voltage, showing tensile as-deposited residual stresses and (b) of the coating grown at -80 V bias voltage, showing compressive stresses.

In Fig. 8 the DSC signals of the coating grown at -40 V bias voltage, having tensile as-deposited residual stresses and the coating synthesized using -80 V bias voltage, revealing compressive stresses, were fitted using the Gaussian function in order to show the different partial reactions that take place. Based on the results presented, the DSC peaks can be interpreted as follows: As up to temperatures of ~800 °C there is no apparent sign of spinodal decomposition visible in the XRD patterns (Fig. 1 and Fig. 4), the reactions below this temperature have mainly to be due to defect annihilation and recovery effects. Nevertheless, it has to be considered that the reactions overlap and that formation of small fcc-AlN and fcc-TiN enriched domains due to spinodal decomposition has also started at these temperatures

[10]. The reactions between ~850 and ~1150 °C can be attributed to the spinodal decomposition, where the influence of the different domain sizes becomes significant. Rachbauer *et al.* [28] could recently prove by three-dimensional atom probe tomography that the fcc-AlN enrichment is faster at column or grain boundaries, compared to the bulk. According to Fig. 8, the decomposition is faster for the coating with the compressive as-deposited stresses, as the fourth peak is shifted to lower temperatures compared to that of the coating with tensile stresses. This effect can be attributed to the smaller domain size of the coating with compressive stresses in relation to that with tensile stresses and the fact that a smaller domain size results in a higher grain boundary volume.

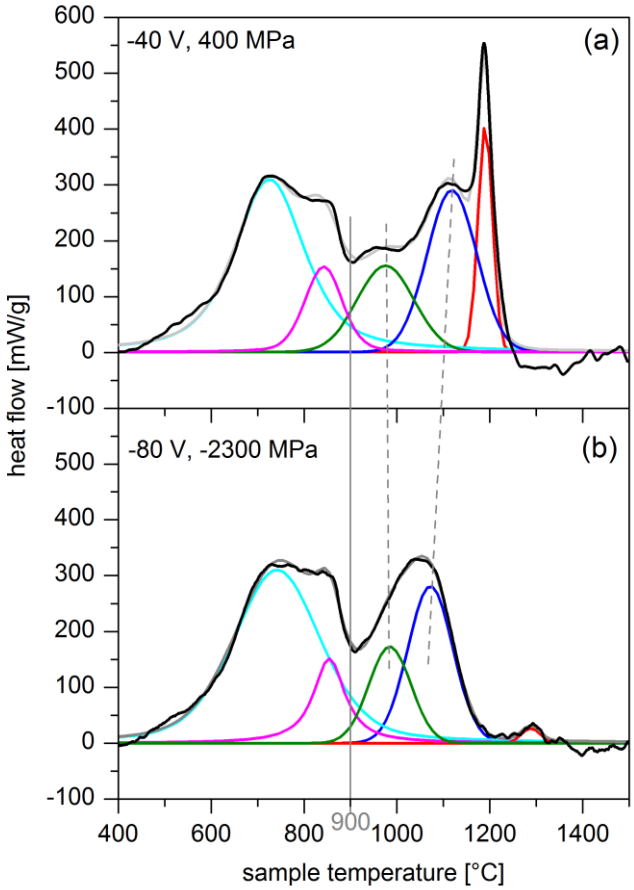

Fig. 8: DSC signal and Gaussian fit of the five exothermic partial reactions during DSC including the sum fit (indicated in grey) of (a) the coating deposited using -40 V bias voltage, showing tensile residual stresses and (b) the coating synthesized at -80 V bias voltage, having compressive stresses. The vertical solid line at 900 °C was added to simplify comparison of the two diagrams. The dashed lines show that the fourth peak is shifted to lower temperatures for (b) with respect to (a).

Further, a smaller domain size means also that there are more nucleation sites available which is, additionally to the higher lattice parameter, an explanation for the earlier precipita-

tion of w-AlN for the coatings with compressive as-deposited residual stresses. From the XRD patterns in Fig. 7b it could be seen that after annealing to 1150 °C there is only a small fcc-AlN shoulder left for the coating with the compressive as-deposited stresses. This infers that already a considerable amount of the fcc-AlN has transformed into w-AlN at this temperature. Thus, the reaction corresponding to the transformation of fcc-AlN into w-AlN has also to be included within the pronounced peak between 900 and 1150 °C for the coating with compressive stresses in Fig. 8. The small peak at temperatures above 1200 °C has to be due to grain growth as the XRD peaks become only sharper at these high temperatures. For the coating with the tensile as-deposited stresses there is still a lot of fcc-AlN present at temperatures of 1150 °C (Fig. 7a), which has to transform into w-AlN. This reaction is responsible for the pronounced peak in the DSC signal (Fig. 8) at ~1200 °C for the coating with tensile stresses.

Finally, hardness measurements of as-deposited samples and samples annealed to 1000 °C were conducted. From Fig. 9 it can be seen that the hardness of the annealed samples is higher than that of the as-deposited samples, which is in good agreement with literature [6, 10, 29]. After annealing to 1000 °C, the spinodal decomposition is already advanced and leads - as a result of coherency strains between matrix and the formed coherent small domains - to age hardening [6]. Additionally, it can be seen that the difference between as-deposited and annealed samples is more pronounced at lower bias voltages. This can be explained by the different as-deposited residual stresses. The coatings deposited at lower bias voltages showed tensile as-deposited residual stresses. In general, coatings with tensile stresses show lower hardness values compared to coatings with compressive stresses [30-33]. After annealing to 1000 °C, fcc-TiN domains and w-AlN precipitations have formed. As both are more volume consuming than the $Ti_{1-x}Al_xN$ matrix, it can be assumed that the tensile stresses turn into compressive, which has an additional positive influence on the hardness. The coatings deposited at higher bias voltages exhibit compressive as-deposited residual stresses. After annealing to 1000 °C, fcc-AlN domains and w-AlN precipitations have formed. The fcc-AlN domains are smaller but the w-AlN precipitations are more volume consuming than the $Ti_{1-x}Al_xN$ matrix. Thus, it can be assumed that the compressive stresses slightly increase, which also positively affects the hardness. However, the influence on the hardness is much more pronounced for the coatings with tensile as-deposited stresses.

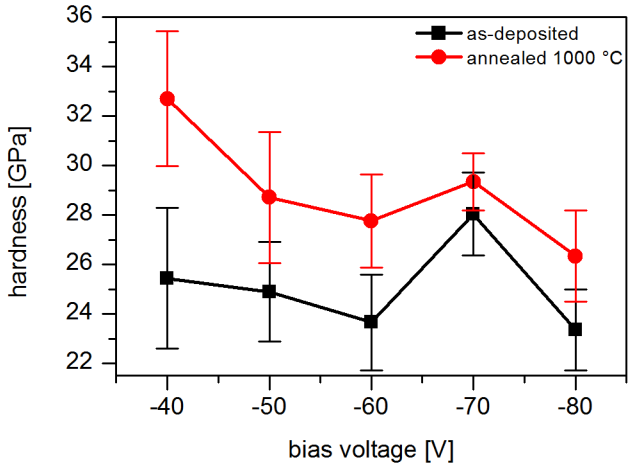

Fig. 9: Evolution of the hardness of coatings versus bias voltage measured on Si samples in as-deposited state and after annealing to 1000 °C.

4. Conclusion

Sputtered $Ti_{1-x}Al_xN$ coatings with residual stresses ranging from tensile to compressive could successfully be synthesized by using different bias voltages. It could be shown that tensile stresses promote the formation of more volume consuming fcc-TiN domains during decomposition of the metastable $Ti_{1-x}Al_xN$ solid solution, while compressive stresses foster the formation of smaller fcc-AlN domains. Emphasis was also laid on the different domains sizes obtained as a result of the different bias voltages. Smaller domain sizes were found to cause faster spinodal decomposition and earlier precipitation of w-AlN. The hardness increase due to age hardening is more pronounced for those coatings showing tensile stresses, which is attributed to the significant contribution of more volume consuming fcc-TiN domains compared to fcc-AlN.

Acknowledgements

Dr. R. Rachbauer and Prof. P.H. Mayrhofer are acknowledged for helpful discussions on spinodal decomposition of $Ti_{1-x}Al_xN$ coatings. Further, the authors are grateful to Matthias Bartosik for assisting in the Williamson-Hall analysis. Financial support by the Austrian Federal Government (in particular from the Bundesministerium für Verkehr, Innovation und Technologie and the Bundesministerium für Wirtschaft, Familie und Jugend) and the Styrian Provincial Government, represented by Österreichische Forschungsförderungsgesellschaft mbH and by Steirische Wirtschaftsförderungsgesellschaft mbH, within the research activities of the K2 Competence Centre on “Integrated Research in Materials, Processing and Product

Engineering", operated by the Materials Center Leoben Forschung GmbH in the framework of the Austrian COMET Competence Centre Programme, is gratefully acknowledged.

References

[1] R. Cremer, M. Witthaut, D. Neuschütz, in: W.D. Cho and H.Y. Sohn (Eds.), Value-Addition Metallurgy, The Minerals, Metals & Materials Society, Warrendale, 1998, pp. 249-258.

[2] A. Kimura, H. Hasegawa, K. Yamada, T. Suzuki, Surf. Coat. Technol. 120-121 (1999) 438.

[3] A. Hörling, L. Hultman, M. Odén, J. Sjölén, L. Karlsson, J. Vac. Sci Technol. A 20(5) (2002) 1815.

[4] A. Hörling, L. Hultman, M. Odén. J. Sjölén, L. Karlsson, Surf. Coat. Technol. 191 (2005) 384.

[5] K. Kutschej, P.H. Mayrhofer, M. Kathrein, P. Polcik, R. Tessadri, C. Mitterer, Surf. Coat. Technol. 200 (2005) 2358.

[6] P.H. Mayrhofer, A. Hörling, L. Karlsson, J. Sjölén, T. Larsson, C. Mitterer, L. Hultman, Appl. Phys. Lett. 83 (10) (2003) 2049.

[7] P.H. Mayrhofer, F.D. Fischer, H.J. Böhm, C. Mitterer, J.M. Schneider, Acta Mater. 55 (2007) 1441.

[8] P.H. Mayrhofer, D. Music, J.M. Schneider, Appl. Phys. Lett. 88 (2006) 071922.

[9] P.H. Mayrhofer, D. Music, J.M. Schneider, J. Appl. Phys. 100 (2006) 094906.

[10] R. Rachbauer, S. Massl, E. Stergar, D. Holec, D. Kiener, J. Keckes, J. Patscheider, M. Stiefel, H. Leitner, P.H. Mayrhofer, J. Appl. Phys. 110 (2011) 023515.

[11] L. Rogström, J. Ullbrand, J. Almer, L. Hultman, B. Jansson, M. Odén, Thin Solid Films 520 (2012) 5542.

[12] Ch. Wüstefeld, D. Rafaja, M. Dopita, M. Motylenko, C. Baehtz, C. Michotte, M. Kathrein, Surf. Coat. Technol. 206 (2011) 1727.

[13] M. Bartosik, R. Daniel, Z. Zhang, M. Deluca, W. Ecker, M. Stefenelli, M. Klaus, C. Genzel, C. Mitterer, J. Keckes, Surf. Coat. Technol. 206 (2012) 4502.

[14] N. Schalk, T. Weirather, C. Polzer, P. Polcik, C. Mitterer, Surf. Coat. Technol. 205 (2011) 4705.

[15] Th.H. De Keijser, J.I. Langford, E.J. Mittermeijer, A.B.P. Vogels, J. Appl. Cryst. 15 (1982) 308.

[16] E.J. Mittemeijer, U. Welzel. Z. Kristallogr. 223 (2008) 552.

[17] I.C. Noyan, J.B. Cohen, Residual stress: Measurement by diffraction and interpretation, Springer-Verlag, New York, 1987.

[18] J.O. Kim, J.D. Achenbach, P.B. Mirkarimi, M. Shinn, S.A. Barnett, J. Appl. Phys. 72 (1992) 1805.

[19] J.Y. Rauch, Ch. Rousselot, N. Martin, Ch. Jacquot, J. Takadoum, J. Eur. Ceram. Soc. 20 (2000) 795.

[20] I. Petrov, P.B. Barna, L. Hultman, J.E. Greene, J. Vac. Sci. Technol. A 21 (2003) 725.

[21] G.K. Williamson, W.H. Hall, Acta Mat. 1 (1953) 22.

[22] D. Rafaja, V. Klemm, G. Schreiber, M. Knapp, R. Kuzel, J. Appl. Cryst. 37 (2004) 613.

[23] D. Rafaja, M. Sima, V. Klemm, G. Schreiber, D. Heger, L. Havela, R. Kuzel, J: Alloy Compd. 378 (2004) 107.

[24] R. Daniel, K.J. Martinschitz, J. Keckes, C. Mitterer, Acta Mater. 58 (2010) 2621.

[25] R.F. Zhang, S. Veprek, Mater. Sci. Eng. A 448 (2007) 111.

[26] International Center for Diffraction Data, PDF-2/Release 2007, card number 00-038-1420.

[27] International Center for Diffraction Data, PDF-2/Release 2007, card number 00-025-1495.

[28] R. Rachbauer, J.J. Gengler, A.A. Voevodin, K. Resch, P.H. Mayrhofer, Acta Mater. 60 (2012) 2091.

[29] A. Knutsson, M.P. Johansson, L. Karlsson, M. Odén, J. Appl. Phys. 108 (2010) 044312.

[30] P.H. Mayrhofer, C. Mitterer, L. Hultman, H. Clemens, Progr. Mater. Sci. 51 (2006) 1032.

[31] P.H. Mayrhofer, C. Mitterer, J. Musil, Surf. Coat. Technol. 174-175 (2003) 725.

[32] P.H. Mayrhofer, F. Kunc, J. Musil, Thin Solid Films 415 (2002) 151.

[33] P.H. Mayrhofer, G. Tischler, C. Mitterer, Surf. Coat. Technol. 142-144 (2001) 78.

Publication III

Friction reduction by thermal treatment of arc evaporated TiAlTaN coatings in methane

N. Schalk, C. Mitterer, I. Letofsky-Papst, C. Czettl, B. Sartory, M. Penoy, C. Michotte

Accepted for publication in Tribology International

Friction reduction by thermal treatment of arc evaporated TiAlTaN coatings in methane

N. Schalk[1,*], C. Mitterer[2], I. Letofsky-Papst[3], C. Czettl[4], B. Sartory[1], M. Penoy[5], C. Michotte[5]

[1] *Materials Center Leoben Forschung GmbH, Roseggerstraße 12, A-8700 Leoben, Austria*

[2] *Department of Physical Metallurgy and Materials Testing, Montanuniversität, Franz-Josef-Straße 18, A-8700 Leoben, Austria*

[3] *Research Institute for Electron Microscopy, Graz University of Technology, Steyrergasse 17, A-8010 Graz, Austria*

[4] *CERATIZIT Austria GmbH, Metallwerk-Plansee-Straße 71, A-6600 Reutte, Austria*

[5] *CERATIZIT Luxembourg S.àr.l., Route de Holzem, B.P.51, L-8201 Mamer, Luxembourg*

Abstract

For severe cutting applications, the reduction of friction between work-piece and tool surface is of vital importance. Within this work, the surface of arc evaporated TiAlTaN coatings was modified by thermal treatment in methane. The modified coatings were investigated with respect to their weight gain, composition, microstructure and friction behaviour. The weight gain is attributed to the formation of an up to ~500 nm thick discontinuous carbon deposit, which consists of an amorphous layer adjacent to the TiAlTaN coating and a graphitic layer on top. The friction coefficient was reduced from 0.66 for the as-deposited coating to 0.25 after the treatment in methane, where the low friction behaviour is stable for sliding distances up to 1000 m.

Keywords: hard coatings, carbon, low friction, annealing

1. Introduction

Economical and ecological demands of the machining industry for still higher cutting speeds and feed rates as well as for the reduction of the use of coolants and lubricants have promoted significant progress for coatings in the metal cutting industry [1-3]. In general, there are two different approaches for tailoring coatings for cutting applications. One is based on hard and wear resistant coatings in the form of transition metal nitrides, carbides or oxides [4]. $Ti_{1-x}Al_xN$ is an important example, which has been widely used in the last years. The properties of $Ti_{1-x}Al_xN$ coatings can be further improved by alloying with different elements like Ta, V, Si or B. Ta has beneficial effects on its mechanical and tribological properties, as it fosters formation of the face-centred cubic (fcc) phase at expense of the wurtzite phase. Further, a significantly improved tribological behaviour at temperatures exceeding 900 °C can be observed, which is due to higher oxidation resistance compared to $Ti_{1-x}Al_xN$ [2, 5-9].

Another approach is based on low-friction coatings like diamond like carbon (DLC). The term DLC comprises various types of carbon based coatings which can be divided into two major groups; (i) hydrogenated (a-C:H) and (ii) hydrogen free (a-C) carbon [4, 10-13]. Drawbacks of these coatings are high compressive stresses and rather poor adhesion for coating thicknesses above 2 µm. A possibility to overcome these disadvantages are metal-containing DLC (M-C:H) coatings. These coatings contain additions like Ti, Ta, W or Nb in M/C ratios of up to ~0.3, which leads to better adhesion and lower compressive stresses [4, 14, 15]. Another example of a low-friction coating is MoS_2, which is commonly used as solid lubricant, especially in vacuum and space applications [16, 17].

Hard coatings with a thin low-friction layer on top, e.g. MoS_2 or WC/C, have been suggested to combine low friction and high wear resistance [1, 18]. Further, the co-deposition of a hard coating, e.g. TiN or TiB_2, and MoS_2 has been proposed, with the aim to achieve a hard matrix to maintain the structural integrity and to obtain solid lubrication throughout the whole coating thickness [17, 19-23]. Another alternative yielding low-friction surfaces are nanocomposite coatings, where a nanocrystalline phase (e.g. TiC or TiCN) is embedded into an a-C:H matrix [24-26].

However, the synthesis of these low-friction coating systems requires sophisticated deposition processes and is consequently quite expensive. Within the present work, an alternative to these rather complex deposition techniques is presented. Arc evaporated TiAlTaN hard coatings were thermally post-treated in methane, which results in formation of a carbon deposit on the coating surface. This carbon layer is expected to positively affect the friction behaviour, which was verified using ball-on-disc tests. To illuminate the formation of these

carbon deposits, the coatings were additionally investigated using a precision balance, X-ray diffraction, Raman spectroscopy, scanning electron microscopy, energy dispersive X-ray spectroscopy and transmission electron microscopy. The proposed process could be beneficial for low-temperature cutting applications [1, 27].

2. Experimental Methods

TiAlTaN coatings with a thickness of ~3 µm were synthesized using an industrial scale Oerlikon Balzers RCS cathodic arc evaporation plant. An additional ~300 nm thick TiN layer was used as bonding layer to enhance adhesion to the cemented carbide substrates. The TiAlTaN coatings were deposited from powder metallurgical targets with target compositions (in at. %) of $Ti_{40}Al_{60}$ and $Ti_{38}Al_{57}Ta_5$ yielding a metal content in the coating (in at. %) of $Ti_{40}Al_{60}$ and $Ti_{38.3}Al_{58.1}Ta_{3.6}$ [2]. As a result of substrate rotation, the coatings exhibit a compositionally modulated nanolayered structure [28]. The depositions were performed in pure nitrogen atmosphere at a pressure of $3.2x10^{-2}$ mbar [2]. Prior to deposition, the cemented carbide substrates (11 % cobalt, 12 % composite carbides, 77 % tungsten carbide) in SNUN geometry (according to ISO 1832), were ground and ultrasonically cleaned.

After deposition, the samples were thermally treated in methane at ambient pressure for one hour. An annealing temperature of 900 °C was chosen, considering that at this temperature the TiAlTaN coating exhibits a hardness maximum due to age hardening [29]. The treatment was conducted in a tube furnace which was flushed with argon during heating-up. The methane was introduced when reaching the desired annealing temperature of 900 °C.

The weight of the samples was determined before and after the thermal treatment using a precision balance and the mean weight change was calculated in mg/cm². The crystallographic structure of the as-deposited and the modified samples was investigated using a Bruker-AXS D8 Advance X-ray diffractometer (XRD) in grazing incidence geometry (incidence angle 2°). Information about the bonding structure of the carbon layer was gained by Raman spectroscopy utilizing a Horiba Jobin-Yvon LABRAM confocal Raman spectrometer equipped with a frequency-doubled Nd-YAG laser (λ = 532.2 nm). The diameter of the used Raman spot was ~0.7 µm. The obtained Raman spectra were subjected to peak fitting using the Gaussian function, utilizing the Origin software, in order to distinguish the existing peaks [30]. Lamellas for transmission electron microscopy (TEM) were prepared by means of an Orsay Physics Cobra Z-05 focused ion beam (FIB). The TEM investigations were conducted using a monochromated FEI Tecnai F20 TEM utilizing a Schottky cathode operated at 200 kV. For electron energy loss spectroscopy (EELS) the TEM is equipped with a high resolution Ga-

tan imaging filter. The EELS measurements were recorded in imaging mode of the TEM; the C2 aperture was 150 µm, the objective aperture 40 µm and the entrance aperture of the Gatan imaging filter 2.5 mm. The energy dispersion of the spectra is 0.3 eV/channel.

The friction behaviour was investigated by means of a CSM ball-on-disc tribometer at room temperature. A wear track radius of 3.4 and 5.0 mm, a normal load of 5 and 10 N and a sliding distance of 300 and 1000 m, respectively, were chosen. For both test sets, the linear speed was 10 cm/s and the relative humidity 37 ± 2 %. Al_2O_3 balls with a diameter of 6 mm were used as counterparts. The resulting wear tracks as well as the surface of the thermally treated samples were examined using a Zeiss Auriga field emission gun - scanning electron microscope (FEG-SEM) equipped with an Apollo 40+ extension for energy-dispersive X-ray spectroscopy (EDX).

3. Results and Discussion

After thermal treatment of the TiAlTaN coated samples in methane, a mean weight gain of 0.37 ± 0.05 mg/cm² was determined. It was obvious that the coating surface was modified as there was a dark layer visible with the bare eye. In Fig. 1a, the SEM micrograph of a fracture cross-section of a thermally treated sample is shown, where a discontinuous top layer can be seen. Using EDX, the layer could be identified as carbon, which originates from the decomposition of methane at elevated temperatures [31]. With the higher magnification used for the micrograph shown in Fig. 1b, the substrate, the TiAlTaN coating and a partial area of the discontinuous carbon layer on top can clearly be distinguished. It can be assumed that high internal stresses within the carbon layer cause delamination between the coating and the carbon layer and are, thus, responsible for its discontinuous structure [32, 33].

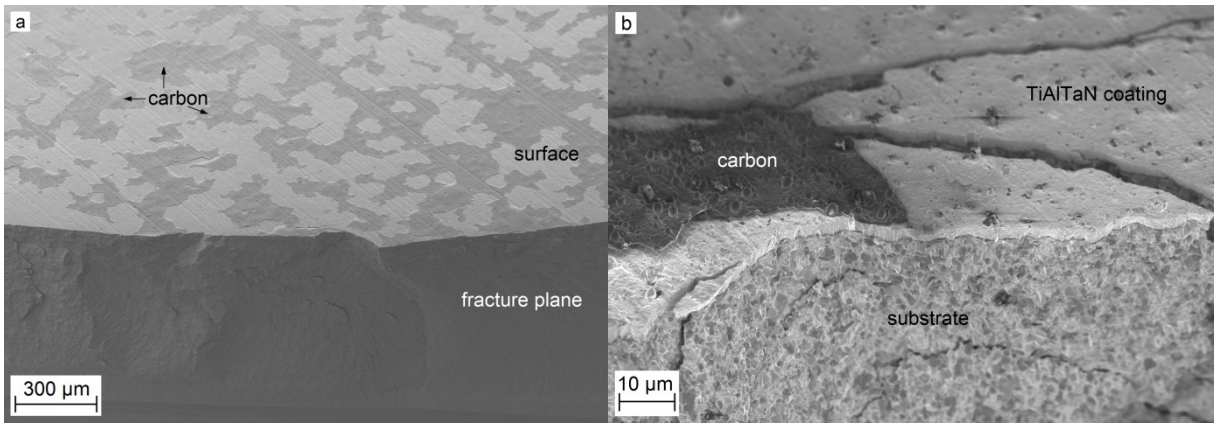

Fig. 1: SEM micrographs showing the fracture cross-sections and surfaces of a sample thermally treated in methane. (a) Overview, showing the discontinuous carbon islands on the coating surface. (b) Detail, were the substrate, the TiAlTaN coating and a part of the carbon layer can be identified.

In order to investigate the influence of the thermal treatment on the crystallographic structure of the coating, XRD measurements were performed on samples thermally treated in methane and for comparison also on as-deposited samples and samples annealed in argon. The corresponding gracing incidence XRD patterns in Fig. 2 show that in the as-deposited state the coating consists of a single-phase fcc TiAlTaN solid solution. The peak positions for fcc-AlN (ICDD 00-025-1495), wurtzite AlN (ICDD 01-076-0702) and fcc-TiN (ICDD 00-038-1420) are plotted as dashed lines. After annealing in argon, a peak broadening and a shoulder on the right hand side of the TiAlTaN peak can be identified, which indicates the onset of spinodal decomposition of the metastable solid solution [34]. The small peaks which are not marked (e.g. at diffraction angles of ~32° and ~48°) belong to the cemented carbide substrate. After annealing in methane, the pattern looks similar to that after annealing in argon with the exception of the broad peak at low diffraction angles, which indicates deposition of carbon.

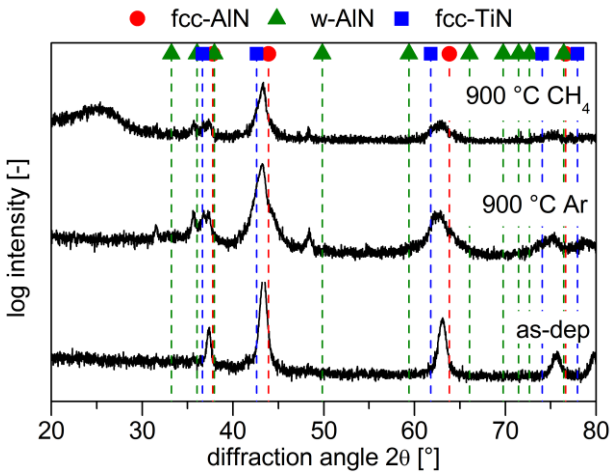

Fig. 2: Comparison of gracing incidence XRD patterns of an as-deposited sample, a sample annealed for 1 hour at 900 °C in argon and a sample annealed for 1 hour at 900 °C in methane.

The bonding structure of the carbon layer was determined using Raman spectroscopy (Fig. 3). Two pronounced peaks at ~1350 and ~1590 cm^{-1} are identified, which can be related to the so-called D and G peak of disordered graphite. The G peak results from stretching vibration of sp^2 sites, whether in chains or in six-fold aromatic rings, while the D peak is related to the breathing mode of the aromatic rings. Existing sp^3 sites influence the disorder of sp^2 sites; thus, the peak intensity ratio of D peak to G peak (I_D/I_G) corresponds roughly to the sp^2/sp^3 bonding ratio [10, 35]. The I_D/I_G ratio determined from the heights of the respective peaks in Fig. 3 is 1.09. The quite high intensity between the two peaks can be attributed to the so-called D3 peak at ~1500 cm^{-1}, which is due to an amorphous carbon fraction [30]. Additionally, a broad peak between 2300 and 3300 cm^{-1} can be observed, which might also be divided into two peaks at ~2700 and ~2900 cm^{-1}, respectively. These are second order peaks of graphitic lattice vibrations [30].

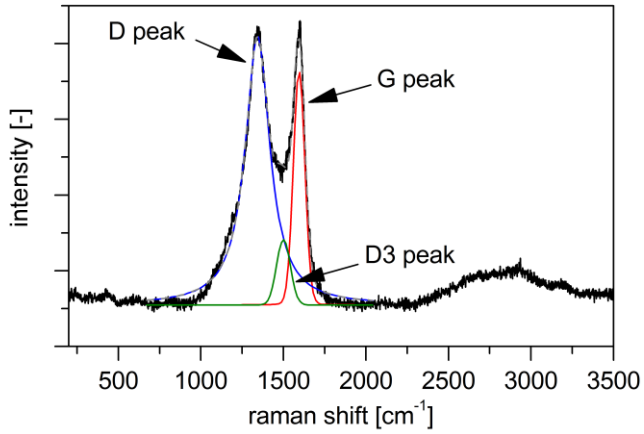

Fig. 3: Raman signal gained from the surface of a sample thermally treated in methane including Gaussian peak fits.

For a more thorough analysis of the coating and the carbon layer after the thermal treatment in methane, TEM investigations were performed. Fig. 4a shows an overview of a TEM lamella. At the bottom of the micrograph the substrate can be identified, followed by the ~300 nm thick TiN bonding layer, the ~3 µm thick TiAlTaN layer, the ~500 nm thick carbon layer and finally a platinum layer on top. The platinum layer is necessary for an accurate FIB preparation, in order to protect the top region of the lamella. There are many light spots visible in the TiAlTaN layer, which are mainly located at column boundaries (Fig. 4a). These light spots are pores, which are due to the onset of spinodal decomposition (Fig. 2). The formation of fcc-AlN domains occurs faster at column or grain boundaries compared to the bulk. In addition, the fcc-AlN domains are smaller than the TiAlTaN matrix, leading to pores [34, 36, 37]. EELS measurements in the coating region near the carbon layer and also at grain boundaries and pores indicated no carbon diffusion into the coating. The detail of the TEM lamella presented in Fig. 4b allows to distinguish two different layers within the carbon deposit.

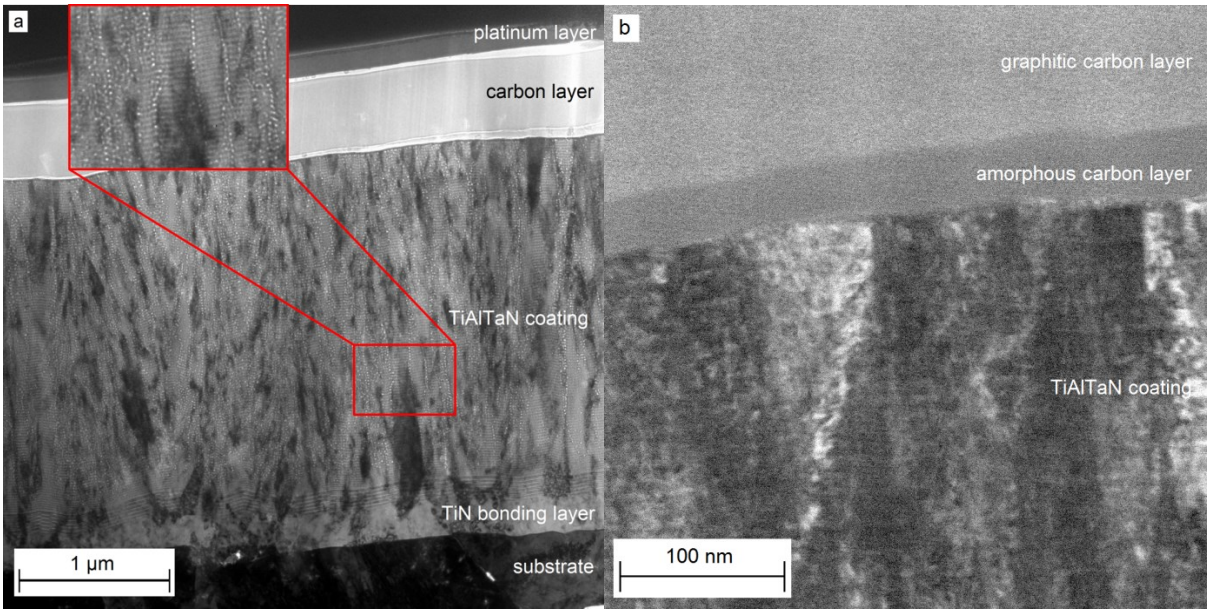

Fig. 4: TEM micrographs of a sample thermally treated in methane. (a) Overview, showing the substrate, the TiAlTaN coating, the carbon layer and the platinum layer on top. In the enlarged detail bright spots indicating pores are visible at column boundaries. (b) Detail, indicating that the carbon deposit consists of two differently structured layers.

The high-resolution TEM micrograph in Fig. 5a shows an amorphous carbon layer adjacent to the TiAlTaN coating and a graphitic structure on top. This is also corroborated by EELS measurements (Fig. 5b) on both layers, which show the typical K-edge for amorphous and graphitic carbon, respectively [38]. Further, the EELS measurements in the amorphous carbon layer revealed the presence of cobalt and oxygen. It can be assumed that the incorporation of these elements is responsible for the amorphous structure of the layer, as they prevent a wide-range order of the carbon atoms. Obviously, the argon flushing at atmospheric pressure during heating-up is not sufficient to remove all oxygen from the tube-furnace. The origin of the cobalt has to be found in the cemented carbide substrate. EDX depth profiles measured on FIB cross-sections of coatings annealed for comparison at 900 °C for 3 hours showed a slight diffusion gradient of cobalt (with a plateau at ~0.8 at. % above a distance of 1 µm from the interface) and also of tungsten (~1.9 at. %). Hörling *et al.* [39] reported on the diffusion of cobalt from cemented carbide substrates (6 % cobalt) through ~3 µm thick arc evaporated TiAlN coatings. They propose that the presence of droplets is responsible for cobalt diffusion. These droplets disturb coating growth, result in shadowing processes and represent re-nucleation sites. Consequently, voids surrounding them and/or growth of coarse-grained areas above them are formed, which provide high-diffusivity paths. In the high-resolution TEM micrograph of the amorphous layer shown in Fig. 5c, dark crystalline areas are visible, where slight enrichment in cobalt and also in tungsten could be determined

by EDX. Iwamura *et al.* [40] observed similar Co-rich clusters in sputter deposited Co:a-C coatings. With increasing distance from the coating surface the presence of out-diffused cobalt becomes less likely and after a certain time the residual oxygen available within the furnace is consumed. From that point, the carbon layer is assumed to be essentially free of impurities. Thus, the wide-range order is no longer disturbed and a graphitic structure develops.

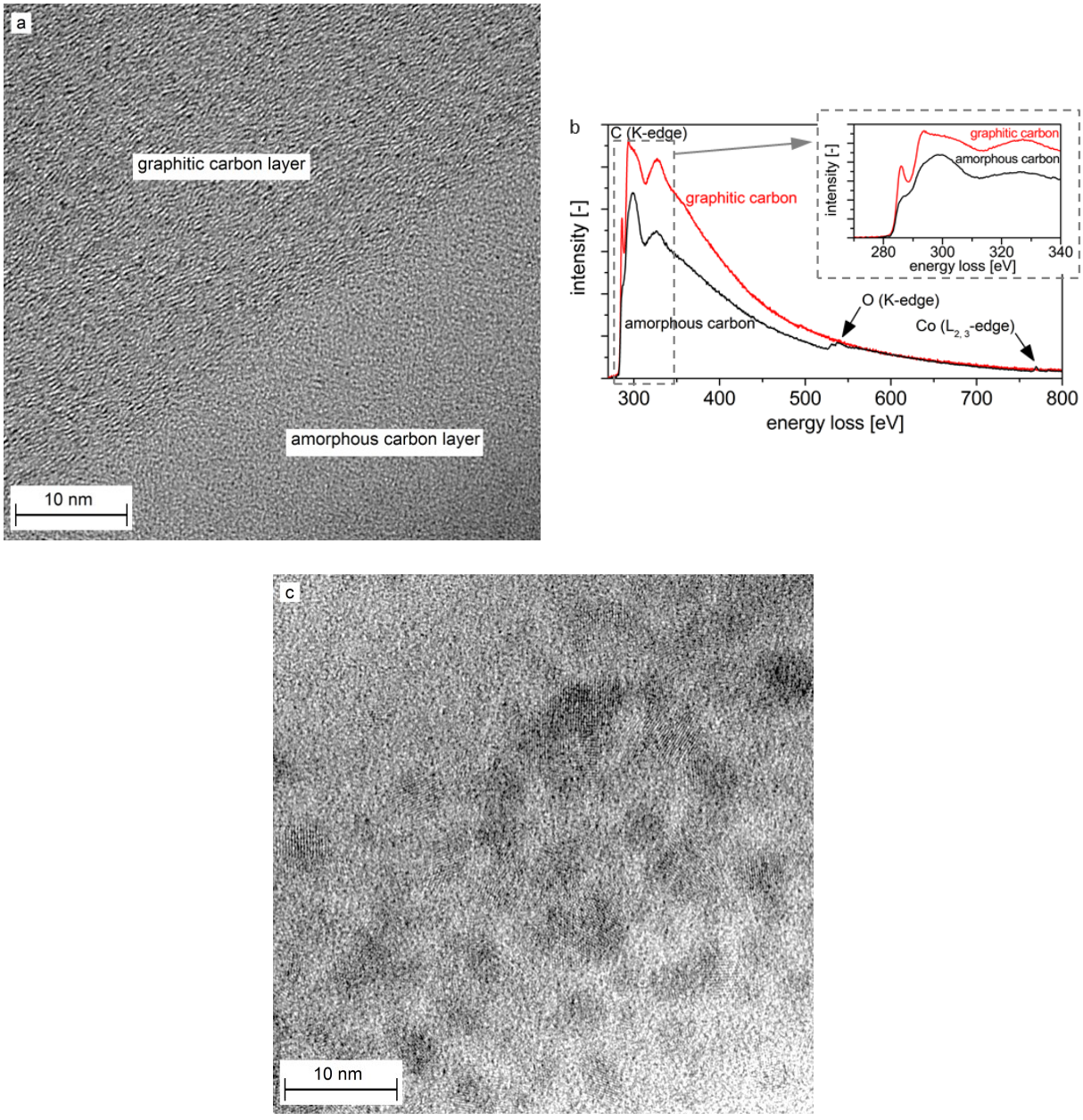

Fig. 5: (a) High-resolution TEM micrograph of the carbon layer, showing an amorphous structure adjacent to the TiAlTaN coating and a graphitic structure on top. (b) Comparison of EELS spectra for the amorphous and the graphitic layer, including a detail of the K-edge of carbon. (c) High-resolution TEM micrograph of the amorphous carbon layer showing dark crystalline areas.

In Fig. 6 the friction coefficient as a function of the sliding distance for an as-deposited coating and a sample treated in methane is shown. After a short running-in period, the friction coefficient of the as-deposited sample reaches a value of ~0.66 and shows quite high scattering. Nevertheless, it stays constant over the whole sliding distance with slightly decreasing scattering. The friction coefficient of the methane treated sample shows also a short running-in period and levels off at a value of ~0.22. The scattering is much lower and the friction coefficient stays constant over a sliding distance of ~700 m. Then, the scattering increases and finally at ~900 m also the friction coefficient increases slightly. However, the methane treated sample shows a significantly lower friction coefficient over the whole sliding distance than the as-deposited sample. It should be noted that the observed friction coefficients are comparable with literature values for DLC and MoS_2 coatings tested under similar conditions [21, 41-43].

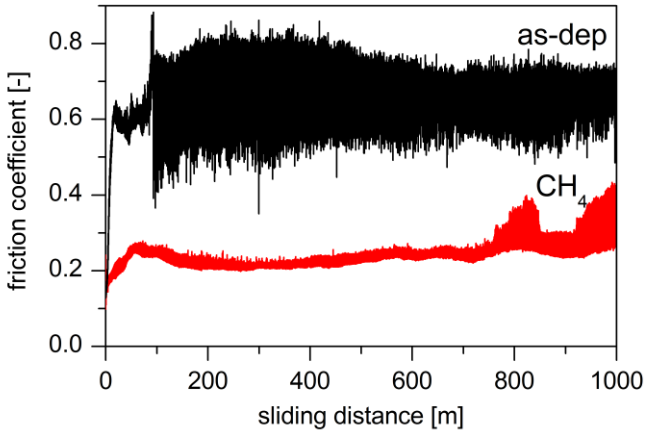

Fig. 6: Friction coefficient as a function of the sliding distance for an as-deposited sample and a sample thermally treated in methane.

Back-scattered electron SEM micrographs of the wear tracks after ball-on-disc tests over a sliding distance of 300 and 1000 m are shown in Figs. 7a and b, respectively. The parallel grooves visible across the wear tracks are due to the grinding process prior deposition. EDX measurements were performed on different positions of the wear tracks, marked in Fig. 7. Within bright areas, no carbon could be detected (EDX 1); however, since the surface sensitivity of EDX is limited, the presence of a very thin (nm range) carbon film cannot be excluded. Carbon was found in scratches appearing grey and dark (EDX 2 and 3) and high carbon concentrations have been found at the border of the wear tracks (EDX 4). The comparison of the two micrographs in Fig. 7 indicates that there is more carbon (i.e. more dark areas) present after a sliding distance of 300 m (Fig. 7a). Nevertheless, even after 1000 m there is still carbon present in the wear track, which is mainly located in the scratches (Fig. 7b).

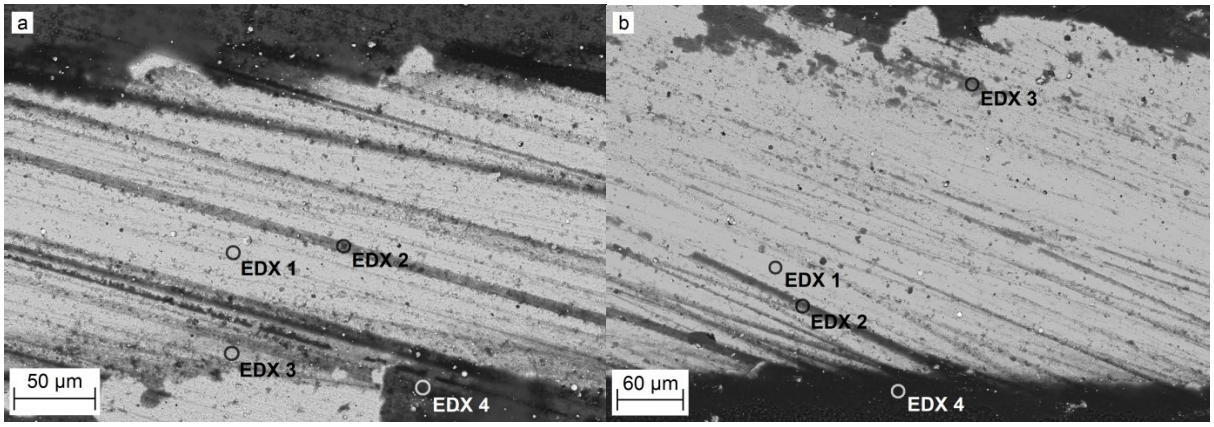

Fig. 7: Back-scattered SEM micrographs of the wear track after ball-on-disc tests of samples thermally treated in methane. EDX measurements were performed in the areas marked EDX 1 to EDX 4. (a) Sliding distance of 300 m and a load of 5 N. (b) Sliding distance of 1000 m and a load of 10 N.

The presence of carbon within these scratches was confirmed by a FIB cross-section through the wear track after the 300 m ball-on-disc test (see Fig. 8). This suggests a mechanism similar to that of surface texturing. There, reservoirs are incorporated into the coating structure, e.g. using a focused laser beam, which are filled with solid lubricants. In the process of wear, the stored lubricants are released, consequently leading to lower friction coefficients [44].

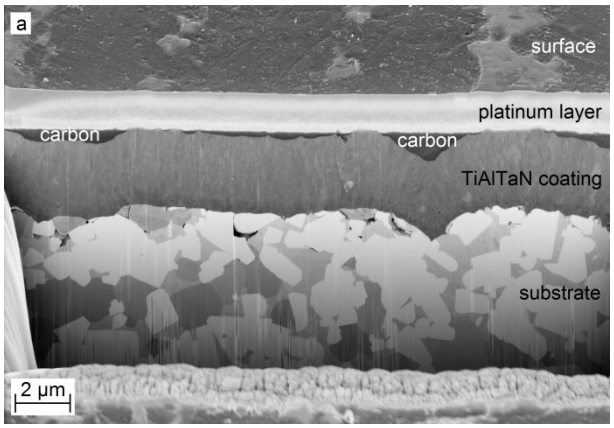

Fig. 8: SEM micrograph of a FIB cross-section through the wear track after a ball-on-disc test with a sliding distance of 300 m.

In Fig. 9, the Raman signals obtained from the wear tracks after ball-on-disc tests with the different sliding distances are compared. The signals look similar to that obtained for the unaffected surface shown in Fig. 3. Again two pronounced peaks at the respective positions of the D and G peak of disordered graphite can be identified. The high intensity between the two peaks corresponds again to the D3 peak and is due to an amorphous carbon fraction. The I_D/I_G ratio after 300 m ball-on-disc test was determined to 1.09 (Fig. 9a), which is the

same value as for the unaffected surface (see Fig. 3). After the 1000 m ball-on-disc test (Fig. 9b), an I_D/I_G ratio of 1.33 was obtained. Thus, a slight graphitization of the remaining carbon has occurred [45]. In Fig. 9b, an additional broad but small peak below 500 cm^{-1} can be identified, which stems from the TiAlTaN coating [46].

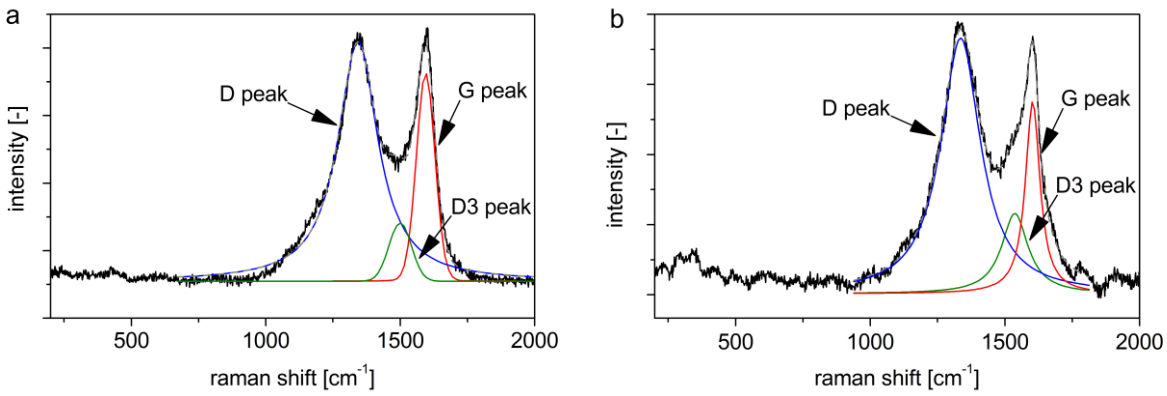

Fig. 9: Raman signal gained from the wear track of samples thermally treated in methane after ball-on-disc tests with (a) a sliding distance of 300 m and a load of 5 N and (b) a sliding distance of 1000 m and a load of 10 N, including Gaussian fits.

4. Conclusion

An alternative to sophisticated and thus expensive deposition techniques for low-friction coatings is presented. Annealing of TiAlTaN coated cemented carbide samples in methane for one hour at 900 °C resulted in formation of a two-layered carbon deposit; an amorphous layer adjacent to the TiAlTaN coating and a graphitic layer on top. Ball-on-disc tests showed a significantly lower friction coefficient of ~0.25 over a sliding distance of 1000 m for the sample thermally treated in methane compared to the as-deposited sample, which showed a friction coefficient of ~0.66. The obtained friction coefficient is comparable to values for DLC tested under similar conditions. The presented thermal post-deposition treatment has the potential to be applied to other hard coating materials as well.

Acknowledgments

The authors are grateful to Oliver Jantschner for helpful discussions on carbon related topics. Financial support by the Austrian Federal Government (in particular from the Bundesministerium für Verkehr, Innovation und Technologie and the Bundesministerium für Wirtschaft, Familie und Jugend) and the Styrian Provincial Government, represented by Österreichische

Forschungsförderungsgesellschaft mbH and by Steirische Wirtschaftsförderungsgesellschaft mbH, within the research activities of the K2 Competence Centre on “Integrated Research in Materials, Processing and Product Engineering”, operated by the Materials Center Leoben Forschung GmbH in the framework of the Austrian COMET Competence Centre Programme, is gratefully acknowledged.

References

[1] V. Derflinger, H. Brändle, H. Zimmermann. New hard/lubricant coating for dry machining. Surf. Coat. Technol. 1999; 113: 286-292.

[2] M. Pfeiler, C. Scheu, H. Hutter, J. Schnöller, C. Michotte, C. Mitterer, M. Kathrein. On the effect of Ta on improved oxidation resistance of Ti-Al-Ta-N coatings. J. Vac. Sci. Technol. 2009; A 27: 554-560.

[3] M. Kathrein, C. Michotte, M. Penoy, P. Polcik, C. Mitterer. Multifunctional multicomponent PVD coatings for cutting tools. Surf. Coat. Technol. 2005; 200: 1867-1871.

[4] A.A. Voevodin, J.M. Schneider, C. Rebholz, A. Matthews. Multilayer composite ceramic metal-DLC coatings for sliding wear applications. Tribol. Int. 1996; 29 7: 559-570.

[5] M. Pfeiler, G.A. Fontalvo, J. Wagner, K. Kutschej, M. Penoy, C. Michotte, C. Mitterer, M. Kathrein. Arc evaporation of Ti-Al-Ta-N coatings: The effect of bias voltage and Ta on high-temperature tribological properties. Tribol. Lett. 2008; 30 (2): 91-97.

[6] K. Kutschej, P.H. Mayrhofer, M. Kathrein, C. Michotte, P. Polcik, C. Mitterer. Multifunctional multi-component $Ti_{1-x}Al_xN$ based coatings. In: G. Kneringer, P. Roedhammer, H. Wildner, editors. Proceeding of the 16th International Plansee Seminar 2005, vol. 2, Reutte, Tyrol, Austria: Plansee Holding AG; 2005, p. 774-488.

[7] K. Kutschej, P.H. Mayrhofer, M. Kathrein, P. Polcik, C. Mitterer. A new low-friction concept for $Ti_{1-x}Al_xN$ based coatings in high-temperature applications. Surf. Coat. Technol. 2004; 188-189: 358-363.

[8] F. Vaz, L. Rebouta, M. Andritschky, M.F. da Silva, J.C. Soares. Oxidation resistance of (Ti, Al, Si)N coatings in air. Surf. Coat. Technol. 1998; 98: 912-917.

[9] K. Kutschej, N. Fateh, P.H. Mayrhofer, M. Kathrein, P. Polcik, C. Mitterer. Comparative study of $Ti_{1-x}Al_xN$ coatings alloyed with Hf, Nb, and B. Surf. Coat. Technol. 2005; 200: 113-117.

[10] J. Robertson. Diamond-like amorphous carbon. Mat. Sci. Eng. 2002; R 37: 129-281.

[11] D.S Kim, T.E. Fischer, B. Gallois. The effects of oxygen and humidity on friction and wear of diamond-like carbon films. Surf. Coat. Technol. 1991; 49: 537-542.

[12] C. Donnet, A. Grill. Friction control of diamond-like carbon coatings. Surf. Coat. Technol. 1997; 94-94: 456-462.

[13] H. Ronkainen, S. Varjus, J. Koskinen, K. Holmberg. Differentiating the tribological performance of hydrogenated and hydrogen-free DLC coatings. Wear 2001; 249: 260-266.

[14] M. Grischke, K. Bewilogua, K. Trojan, H. Dimigen. Application-oriented modifications of deposition processes for diamond-like-carbon-based coatings. Surf. Coat. Technol. 1995; 74-75: 739-745.

[15] K. Bewilogua, C.V. Cooper, C. Specht, J. Schröder, R. Wittorf, M. Grischke. Effect of target material on deposition and properties of metal-containing DLC (Me-DLC) coatings. Surf. Coat. Technol. 2000; 127: 224-232.

[16] J. Rechberger, P. Brunner, R. Dubach. High performance cutting tools with a solid lubricant physically vapour-deposited coating. Surf. Coat. Technol. 1993; 62: 393-398.

[17] R. Gilmore, M.A. Baker, P.N Gibson, W. Gissler, M. Stoiber, P. Losbichler, C. Mitterer. Low-friction TiN-MoS_2 coatings produced by dc magnetron co-deposition. Surf. Coat. Technol. 1998; 108-109: 345-351.

[18] R. Dubach, H. Curtins, R. Rechberger. Improved tool performance through metastability in hard coatings. Surf. Coat. Technol. 1997; 94-95: 622-626.

[19] Y.W. Bae, W.Y. Lee, T.M. Besmann, C.S. Yust, P.J. Blau. Preparation and friction characteristics of self-lubricating TiN-MoS_2 composite coatings. Mater. Sci. Eng. 1996; A209: 372-376.

[20] R. Gilmore, M.A. Baker, P.N. Gibson, W. Gissler. Preparation and characterisation of low-friction TiB_2-based coatings by incorporation of C or MoS_2. Surf. Coat. Technol. 1998; 105: 45-50.

[21] R. Goller, P. Torri, M.A. Baker, R. Gilmore, W. Gissler. The deposition of low-friction TiN-MoS_x hard coatings by a combined arc evaporation and magnetron sputter process. Surf. Coat. Technol. 1999; 120-121: 453-457.

[22] Da-Yung Wang, Chi-Lung Chang, Zie-Yih Chen, Wei-Yu Ho. Microstructural and tribological characterization of MoS_2-Ti composite solid lubriacating films. Surf. Coat. Technol. 1999; 120-121: 629-635.

[23] S. Carrera, O. Salas, J.J. Moore, A. Woolverton, E. Sutter. Performance of CrN/MoS_2(Ti) coatings for high wear low friction applications. Surf. Coat. Technol. 2003; 167: 25-32.

[24] A.A. Voevodin, J.S. Zabinski. Load-adaptive crystalline-amorphous nanocomposites. J. Mater. Sci. 1998; 33: 319-327.

[25] K. Polychronopoulou, C. Rebholz, M.A. Baker, L. Theodorou, N. G. Demas, S.J. Hinder, A.A. Polycarpou, C.C. Doumanidis, K. Böbel. Nanostructure, mechanical and tribological properties of reactive magnetron sputtered TiC_x coatings. Diam. Relat. Mater. 2008; 17: 2054-2061.

[26] C. Tsotsos, K. Polychronopoulou, N.G. Demas, G. Constantinides, S. Gravani, K. Böbel, M.A. Baker, A.A. Polycarpou, C. Rebholz. Mechanical and high pressure tribological properties of nanocrystalline Ti(N,C) and amorphous C:H nanocomposite coatings. Diam. Relat. Mater. 2010; 19: 960-963.

[27] A.E. Reiter, C. Mitterer, M. Rebelo de Figueiredo, R. Franz. Abrasive and adhesive wear behavior of arc-evaporated $Al_{1-X}Cr_XN$ hard coatings. Tribol. Lett. 2010; 37: 605-611.

[28] J. Neidhardt, M. O'Sullivan, A.E. Reiter, W. Rechberger, W. Grogger, C. Mitterer. Structure-property-performance relations of high-rate reactive arc-evaporated Ti-B-N nanocomposite coatings. Surf. Coat. Technol. 2006; 201: 2553-2559.

[29] R. Rachbauer, D. Holec, P.H. Mayrhofer. Increased thermal stability of Ti-Al-N thin films by Ta allyoing. Surf. Coat. Technol. 2012; 211: 98-103.

[30] A. Sadezky, H. Muckenhuber, H. Grothe, R. Niesser, U. Pöschl. Raman microspectroscopy of soot and related carbonaceous materials: Spectral analysis and structural information. Carbon 2005; 43: 1731-1742.

[31] P. Jana, V.A. de la Pena O'Shea, J.M. Coronado, D.P. Serrano. Cobalt based catalysts prepared by Pechini method for CO_2-free hydrogen production by methane decomposition. Int. J. Hydrogen Energ. 2010; 35: 10285-10294.

[32] J.A. Thornton. Coating deposition by sputtering. In: R.F. Bunshah, editor. Deposition technologies for films and coatings, New. Jersey: Noyes Publications; 1982, p. 170-243.

[33] T.K. Schmidt, T.J. Balk, G. Dehm, E. Arzt. Influence of tantalum and silver interlayers on thermal stress evolution in copper thin films on silicon substrates. Scripta Mater. 2004; 50: 733-737.

[34] P.H. Mayrhofer, A. Hörling, L. Karlsson, J. Sjölén, T. Larsson, C. Mitterer, L. Hultman. Self-organized nanostructures in the Ti-Al-N system. Appl. Phys. Lett. 2003; 83 (10): 2049-2051.

[35] S. Zhang, X.T. Zeng, H. Xie, P. Hing. A phenomenological approach for the I_d/I_g ratio and sp^3 fraction of magnetron sputtered a-C films. Surf. Coat. Technol. 2000; 123: 256-260.

[36] R. Rachbauer, J.J. Gengler, A.A. Voevodin, K. Resch, P.H. Mayrhofer. Temperature driven evolution of thermal, electrical, and optical properties of Ti-Al-N coatings. Acta Mater. 2012; 60: 2091-2096.

[37] R.F. Zhang, S. Veprek. Metastable phases and spinodal decomposition in $Ti_{1-x}Al_xN$ system studied by ab initio and thermodynamic modelling, a comparison with the TiN-Si_3N_4 system. Mater. Sci. Eng. 2007; A 448: 111-119.

[38] L. Ponsonnet, C. Donnet, K. Varlot, J.M. Martin, A. Grill, V. Patel. EELS analysis of hydrogenated diamond-like carbon films. Thin Solid Films 1998; 319: 97-100.

[39] A. Hörling. L. Hultman, M. Odén, J. Sjölén, L. Karlsson. Thermal stability of arc evaporated high aluminum-content $Ti_{1-x}Al_xN$ thin films. J. Vac. Sci. Technol. 2002; A20: 1815-1822.

[40] E. Iwamura. Structural ordering of metal-containing amorphous carbon thin films induced by low-energy electron beam projection. Rev. Adv. Mater. Sci. 2003; 5: 166-170.

[41] A. Grill. Tribology of diamondlike carbon and related materials: an updated review. Surf. Coat. Technol. 1997; 94-95: 507-513.

[42] C. Donnet. Recent progress on the tribology of doped diamond-like and carbon alloy coatings: a review. Surf. Coat. Technol. 1998; 100-101: 180-186.

[43] G. Gassner, P.H. Mayrhofer, J. Patscheider, C. Mitterer. Thermal stability of nanocomposite CrC/a-C:H thin films. Thin Solid Films 2007; 515: 5411-5417.

[44] A.A. Voevodin, J.S. Zabinski. Laser surface texturing for adaptive solid lubrication. Wear 2006; 261: 1285-1292.

[45] F. Rabbani. Phenomenological evidence for the wear-induced graphitization model of amorphous hydrogenated carbon coatings. Surf. Coat. Technol. 2004; 184: 194-207.

[46] C.P. Constable, J. Yarwood, W.-D. Münz. Raman microscopic studies of PVD hard coatings. Surf. Coat. Technol. 1999; 116-119: 155-159.

Publication IV

Dry-blasting of α- and κ-Al_2O_3 CVD hard coatings: Friction behavior and thermal stress relaxation

N. Schalk, C. Mitterer, C. Czettl, B. Sartory, M. Penoy, C. Michotte

Submitted for publication.

Dry-blasting of α- and κ-Al_2O_3 CVD hard coatings: Friction behavior and thermal stress relaxation

N. Schalk[1], C. Mitterer[2], C. Czettl[3], B. Sartory[1], M. Penoy[4], C. Michotte[4]

[1] *Materials Center Leoben Forschung GmbH, Roseggerstraße 12, A-8700 Leoben, Austria*

[2] *Department of Physical Metallurgy and Materials Testing, Montanuniversität, Franz-Josef-Straße 18, A-8700 Leoben, Austria*

[3] *CERATIZIT Austria GmbH, Metallwerk-Plansee-Straße 71, A-6600 Reutte, Austria*

[4] *CERATIZIT Luxembourg S.àr.l., Route de Holzem, B.P.51, L-8201 Mamer, Luxembourg*

Abstract

Post-deposition blasting treatments of cemented carbide cutting tools coated by chemical vapor deposition have gained increasing interest. Within the present work, α- and κ-Al_2O_3 coatings dry-blasted using different pressures as well as globular and edged blasting materials were investigated. A higher pressure resulted in an increase of the compressive residual stresses, as determined by X-ray diffraction. Both blasting materials had a minor influence on the roughness of α-Al_2O_3, while the edged material caused a significant roughness increase for κ-Al_2O_3. For α-Al_2O_3 dry-blasted using the globular material, complete stress relaxation could be observed after annealing at 500 °C, whereas for α-Al_2O_3 dry-blasted using the edged material as well as for the κ-Al_2O_3 an annealing temperature of 900 °C was necessary for stress relaxation. The friction coefficient of the dry-blasted samples first increases with increasing temperature, due to increasing plastic deformation of the blasting material transferred onto the coating surface, until it decreases again above 700 °C, due to softening of the transferred material.

Keywords: Al_2O_3, CVD, post-treatment, blasting, stress relaxation, ball-on-disc test

1. Introduction

Due to its high hardness, chemical inertness and low thermal conductivity, Al_2O_3 is widely used as wear protective hard coating for cemented carbide cutting tools. Al_2O_3 coatings are mainly synthesized using chemical vapor deposition (CVD). They exist in several crystallographic modifications, where the stable α-phase (rhombohedral) and the metastable κ-phase (orthorhombic) are prevalent. At elevated temperatures, the metastable κ-Al_2O_3 transforms into the stable α-Al_2O_3, which is accompanied by a volume shrinkage of 7 %, consequently deteriorating coating performance [1-5]. If the $\kappa \rightarrow \alpha$ transformation during application can be avoided, the κ-phase exhibits several advantages compared to the α-phase, e.g. lower thermal conductivity resulting in a more efficient thermal barrier during high-speed cutting [1]. Consequently, both modifications are commercially applied for cemented carbide cutting tools [1, 5, 6].

Further potential for improvement of these hard coatings is achieved by post-deposition treatments like wet- or dry-blasting. The influence of both, wet- as well as dry-blasting on the wear during milling and on the mechanical properties of coatings grown by physical vapor deposition was comprehensively investigated by Bouzakis *et al.* [7-10]. Barbatti *et al.* [11] reported on the effect of wet-blasting using Al_2O_3 particles on the microstructure and residual stresses of CVD κ-Al_2O_3 coatings. Riedl *et al.* [12] discussed the tribological properties of CVD α- and κ-Al_2O_3 coatings modified by blasting using AlSi particles. Additionally, there are a few reports available dealing with the depth-resolved determination of the compressive stresses introduced by blasting treatments [13, 14]. However, a comprehensive understanding of the effect of blasting on coating surface topography, friction performance and the relaxation of the introduced stresses during high-temperature exposure is not available in literature.

Thus, the aim of the present work is to investigate (*i*) the relaxation of the compressive stresses, introduced by dry-blasting using different blasting materials and pressures, at elevated temperatures and (*ii*) the effects of these dry-blasting treatments on the friction behavior. α- and κ-Al_2O_3 coated cemented carbide samples were dry-blasted using three different blasting pressures and two different blasting materials; i.e. a globular and an edged one. The dry-blasted samples were annealed in a vacuum furnace and subsequently the stresses were determined and compared to the stresses prior to the thermal treatment. In addition, ball-on-disc tests were performed at different temperatures to illuminate the effect of surface topography modified by blasting.

2. Experimental Methods

The coatings were deposited using a SuCoTec SCT600TH industrial-scale CVD plant. α- and κ-Al_2O_3 coatings with a thickness of ~8 µm were synthesized from $AlCl_3$-CO_2-H_2-H_2S precursors at a temperature of 1000 °C and a pressure of 75 mbar [5, 6]. The TiCN base-layer, with a thickness of ~9 and ~11 µm beneath the α- and κ-Al_2O_3, respectively, was grown using medium-temperature CVD from $TiCl_4$-CH_3CN-H_2-N_2-CO precursors at 900 °C and 100 mbar [15]. Prior, a ~400 nm thick TiN bonding layer was deposited to improve the adhesion to the substrate. The coatings were grown on cemented carbide substrates, containing 11 wt.-% cobalt, 12 wt.-% mixed carbides and 77 wt.-% tungsten carbide, in SNUN 120412 (according to ISO 1832) and disc (Ø 30 x 4 mm) geometry. Additionally, small cemented carbide discs (Ø 14 x 2 mm) with a composition of 9 wt.-% cobalt, 0.75 wt.-% mixed carbides and 90.25 wt.-% tungsten carbide were coated for X-ray diffraction (XRD).

After deposition, the samples were dry-blasted using two different blasting materials; (*i*) globular particles (see Fig. 1a, type Keramikperlen supplied by Kuhmichel Abrasiv GmbH, composition: ~62.0 % ZrO_2, ~27.8 % SiO_2, ~4.6 % Al_2O_3, remaining fraction ceramic impurities) and (*ii*) sharp-edged (in the following called edged) particles (see Fig. 1b, type Alodur ZK40 supplied by Treibacher Schleifmittel GmbH, composition: ~54.5 % Al_2O_3, ~41.5 % ZrO_2, remaining fraction ceramic impurities). The globular medium has an average particle diameter d_{50} of 125 – 250 µm and a hardness of ~700 HV, while the mesh grit size of the edged medium is 180/220 and the hardness ~2000 HV. Three different blasting pressures (0.8, 1.2 and 1.5 bar) were used. The blasting time was 14 s and the working angle 15°.

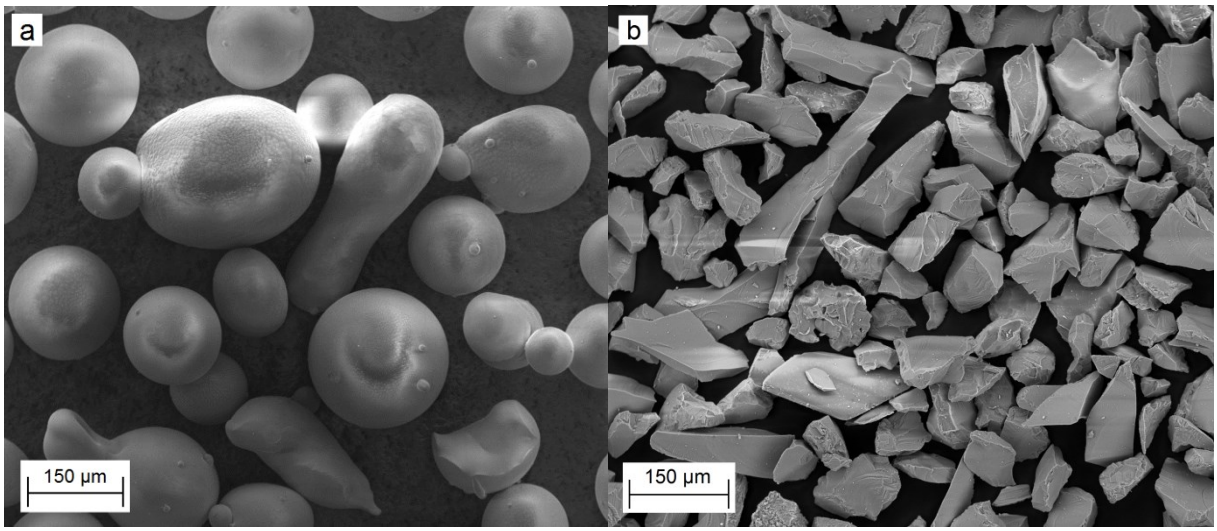

Fig. 1: SEM micrographs of (a) the globular and (b) the edged blasting material.

The average arithmetical surface roughness S_a of the as-deposited as well as the dry-blasted samples was determined using a Leica DCM3D dual-core profilometer. A Zeiss Auriga Cross-beam field emission gun - scanning electron microscope (FEG-SEM) equipped with an Apollo 40+ extension for energy-dispersive X-ray emission spectroscopy (EDX) was used to investigate the coating surfaces and fracture cross-sections. As-deposited as well as dry-blasted samples were annealed in a vacuum furnace (HTM Reetz, base pressure $<5x10^{-4}$ Pa) at 500, 700 and 900 °C, using a heating rate of 20 K/min, a holding time of 15 min and a cooling rate of 60 K/min. The residual in-plane stresses of as-deposited, dry-blasted and annealed samples were determined using the $\sin^2\psi$ method [16] utilizing a Panalytical Empyrean X-ray-diffractometer. A CSM ball-on-disc tribometer was used to investigate the friction behavior at room temperature (RT), 500, 700 and 900 °C. The sliding distance was 300 m, the normal load 5 N and the linear speed 10 cm/s. A wear track radius of 7 mm was chosen for the tests performed at RT, 500 and 700 °C, while the tests at 900 °C were done at a radius of 4.5 mm. Al_2O_3 balls with a diameter of 6 mm were used as counterparts. Cross-sections through the coating within the wear track were prepared by the means of an Orsay Physics Cobra Z-05 focused ion beam (FIB) system.

3. Results and Discussion

In Figs. 2a and b, SEM micrographs of the fracture cross-sections of as-deposited α- and κ-Al_2O_3 coatings, respectively, are shown. The substrate, the TiN bonding layer, the TiCN base-layer and the Al_2O_3 top-layer can clearly be distinguished.

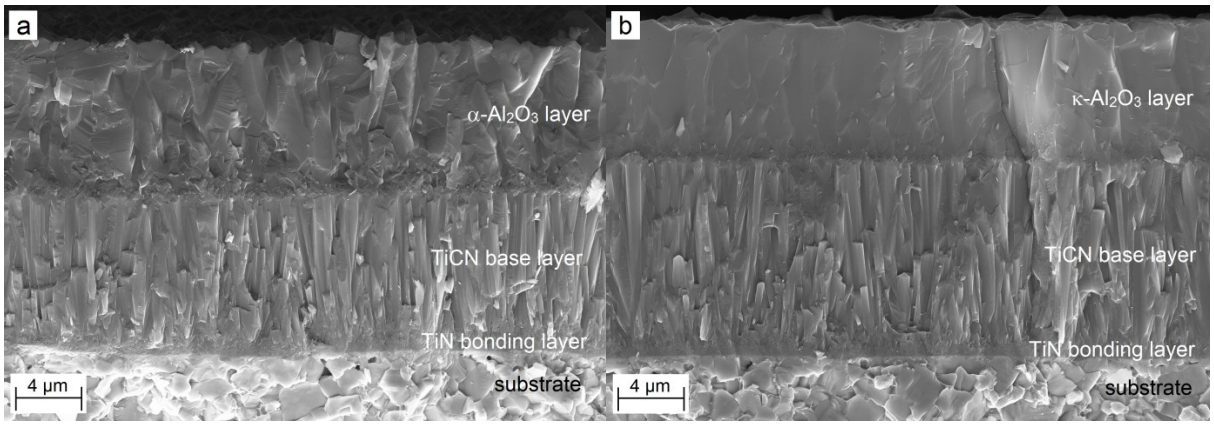

Fig. 2: SEM micrographs of the fracture cross-sections of as-deposited (a) α-Al_2O_3 and (b) κ-Al_2O_3.

The average arithmetical surface roughness S_a for α- and κ-Al_2O_3 in as-deposited state and after dry-blasting with the different blasting materials and pressures is compared in Fig. 3. In the as-deposited state, the roughness of α-Al_2O_3 (Fig. 3a) is with a value of 0.13 µm slightly lower than that of κ-Al_2O_3 with 0.15 µm (Fig. 3b). No significant roughness changes have been observed for α-Al_2O_3 after blasting with the globular medium, while blasting with the edged material leads to a slightly decreased surface roughness. The different blasting pressures did not yield in a significant influence. However, a much more pronounced effect was found for the roughness of κ-Al_2O_3 (see Fig. 3b), where rising Sa values are found for increasing blasting pressures. This evolution is even more distinct for the edged blasting material.

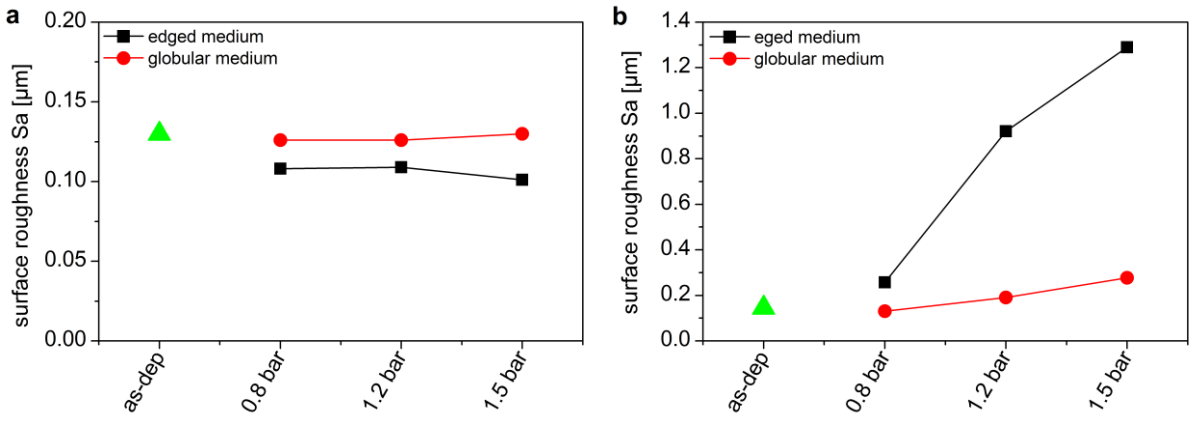

Fig. 3: Arithmetical average surface roughness S_a of as-deposited samples and after dry-blasting with different blasting materials and pressures. (a) α-Al_2O_3 and (b) κ-Al_2O_3.

In Fig. 4, SEM micrographs of the surface of α- and κ-Al_2O_3 coatings in the as-deposited state and after dry-blasting with the globular as well as the edged blasting material at 1.5 bar are compared. After blasting with these materials, extended areas covered with transferred blasting material are seen and the original surface structure is no longer visible. Blasting of κ-Al_2O_3 with the edged material at 1.5 bar results in split-offs of coating material. By comparing the micrographs in Fig. 4 it can be stated that the higher the blasting pressure is, the more transferred blasting material is present on the surface and the less of the original surface structure is visible.

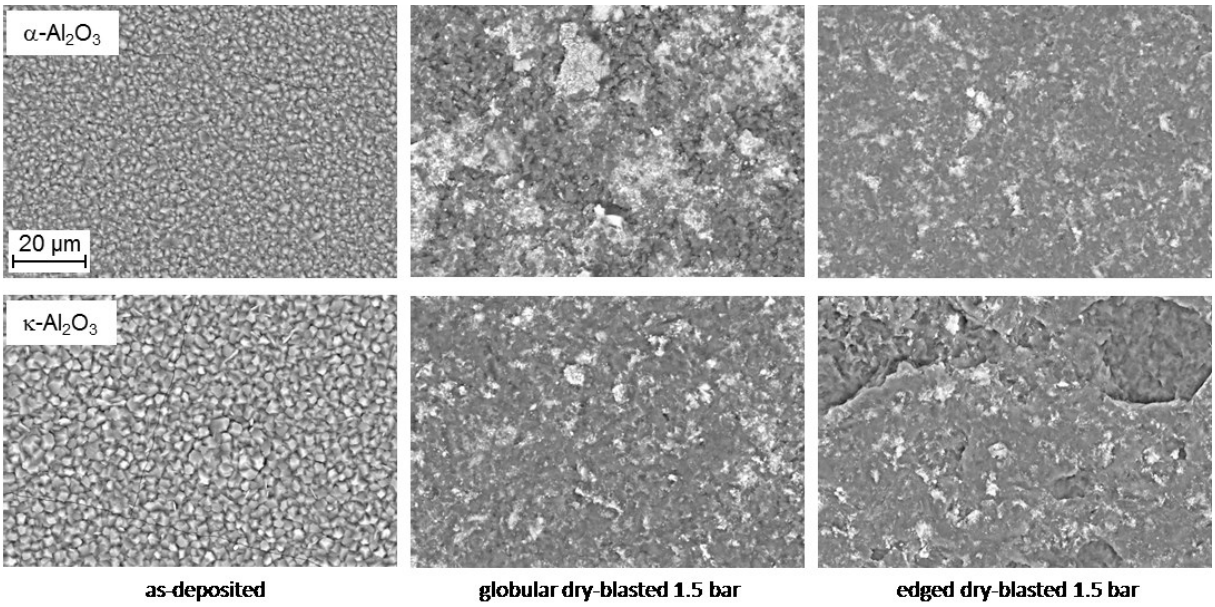

Fig. 4: SEM micrographs of the surface of as-deposited and dry-blasted α-Al_2O_3 and κ-Al_2O_3.

To illustrate the effect of different blasting pressures, Fig. 5 presents micrographs of the surface of α-Al_2O_3 dry-blasted with the globular material at 0.8, 1.2 and 1.5 bar, indicating increasing fractions of the surface covered by transferred blasting material.

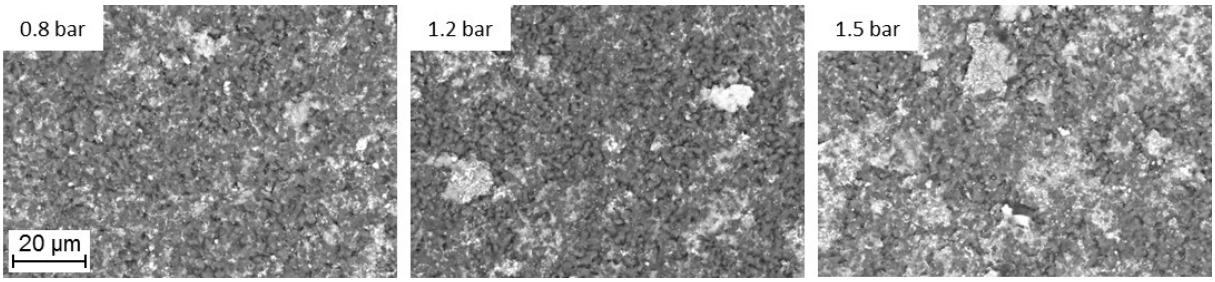

Fig. 5: SEM micrographs of the surface of α-Al_2O_3 dry-blasted with the globular material and different blasting pressures.

The effect of different blasting pressures on the residual stresses in α-Al_2O_3 is shown in Fig. 6a for both blasting materials. The tensile stresses in the as-deposited state turn into compressive after blasting. The higher the blasting pressure is, the higher are the introduced compressive stresses, where the edged blasting material has a more pronounced influence. In Fig. 6b, the effect of increasing annealing temperatures on the residual stresses of α-Al_2O_3 is shown for the as-deposited state and after blasting with different pressures and materials. For the as-deposited sample, only a slight relaxation of the tensile stress can be observed after annealing. Although first stress relaxation was already observed after annealing at 500 °C, no complete relaxation took place up to 900 °C, which can be explained by the still higher deposition temperature of 1000 °C. For the samples blasted with the globular materi-

al, a complete relaxation of the introduced compressive stresses can already be observed after annealing at 500 °C, independent of the blasting pressure. In contrast, for the edged material only the onset of stress relaxation was observed after annealing at 500 °C for the sample blasted at 1.5 bar. For a complete stress relaxation of the samples blasted with the edged material annealing up to 900 °C was necessary.

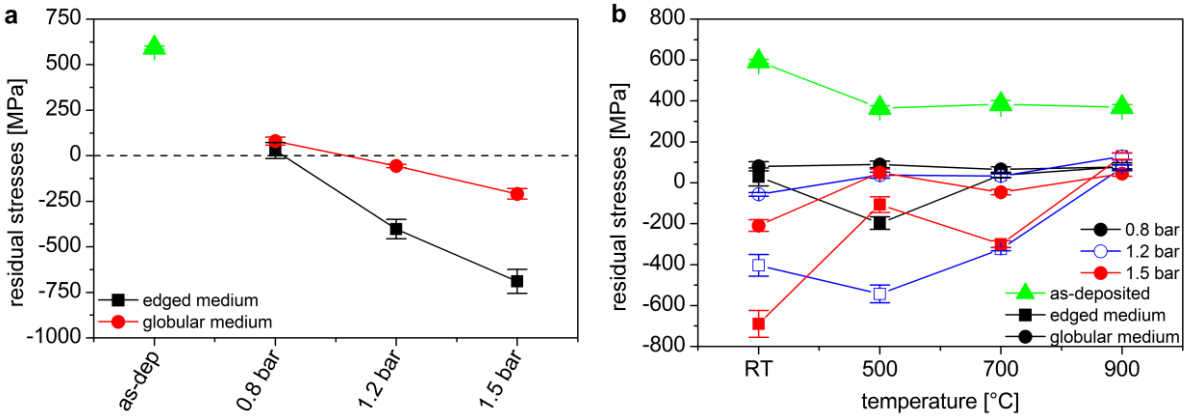

Fig. 6: Residual stresses in α-Al_2O_3 coatings. (a) Comparison of the as-deposited coating and the coatings dry-blasted at different pressures with the edged and the globular medium. (b) Evolution of the residual stresses with increasing annealing temperature.

A comparison of the residual stresses determined for κ-Al_2O_3 in the as-deposited state and after blasting with different pressures and materials is shown in Fig. 7a. In the as-deposited state, κ-Al_2O_3 samples are almost free of stresses. Increasing blasting pressures result in rising compressive stresses, where again the edged material has a more pronounced influence. Fig. 7b shows the effect of increasing annealing temperatures on the residual stresses of κ-Al_2O_3 in the as-deposited state and after blasting with different pressures and materials. While annealing did not significantly affect the (almost zero) stresses in the as-deposited sample, a slight relaxation can already be observed for the dry-blasted samples at 500°C. After annealing to 900 °C, the stresses in all samples are completely relaxed.

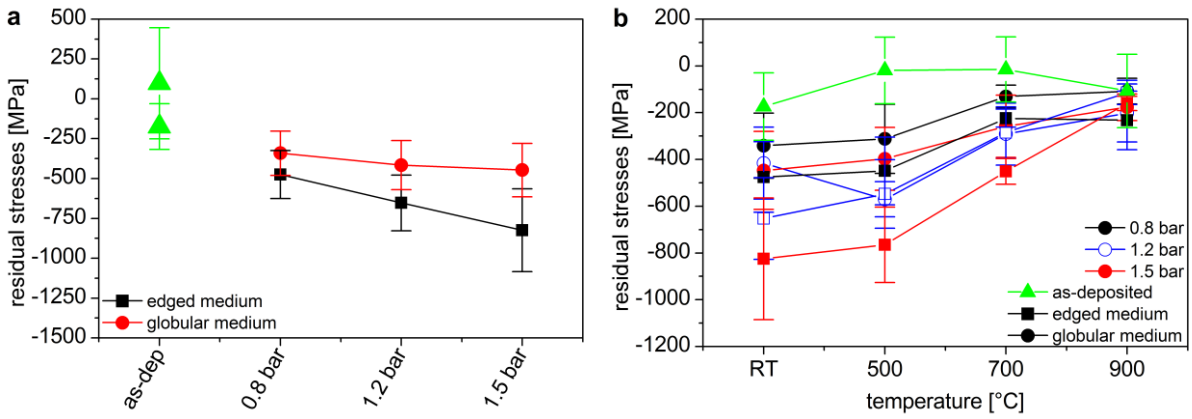

Fig. 7: Residual stresses of κ-Al_2O_3 coatings. (a) Comparison of the as-deposited coating and the coatings dry-blasted at different pressures with the edged and the globular medium, respectively. The stresses measured for the as-deposited state origin from two different samples. (b) Evolution of the residual stresses with increasing annealing temperature.

The friction coefficient as a function of the ball-on-disc testing temperature for α- and κ-Al_2O_3 in the as-deposited state and after blasting with the edged and the globular material using different pressures is shown in Figs. 8a to d. For the as-deposited α-Al_2O_3 sample (Fig. 8a), the friction coefficient increases with increasing temperature, most probably due to promoted plastic deformation of the softening coating and counterpart material [12]. However, at 900 °C a slight decrease was observed. Fig. 9a presents a FIB cross-section through the wear track of this sample after ball-on-disc test at 900 °C. There, a crack crossing the whole Al_2O_3 layer is visible. The bright rim corresponds to TiO_2, as determined by EDX. In the top region of the crack, the bright rim becomes wider; and also in the area of the coating surface surrounding the crack, TiO_2 can be found. This observation is in good agreement with Hochauer *et al.* [17], who reported on the diffusion of titanium from the TiCN base-layer through the thermal crack network of the α-Al_2O_3 layer. Oxidation during high-temperature exposure leads to formation of rutile TiO_2 [17], which explains the reduction of the friction coefficient at 900 °C.

For the α-Al_2O_3 samples dry-blasted with the edged and the globular material (Figs. 8a and b), the friction coefficient also increases with increasing temperature, but it drops already at 700 °C. This drop is related to the blasting material transferred to the coating surface. SEM and EDX investigations of the wear tracks indicated that there is still transferred blasting material present after the ball-on-disc tests. The initially already softer globular blasting material (hardness 700 HV), which is expected to soften considerably at 700 °C and even higher temperatures, can be assumed to be more efficiently smeared over the surface than the harder edged material (hardness 2000 HV). This is confirmed by the nearly mirror-polished

surface of the wear track shown in Fig. 9b, consequently leading to lower friction coefficients compared to the as-deposited sample and to the samples blasted with the edged material (see Figs. 8a and b). At 900 °C, the friction coefficients of the samples blasted with both, the globular and the edged material, decrease further, indicating further thermal softening of the blasting material. Additionally, TiO_2 was found on the surfaces surrounding thermal cracks through the Al_2O_3 top-layer, similar to the as-deposited samples. It has to be noted that at 900 °C the friction coefficient shows a dependence on the blasting pressure, which is contrary for the different blasting materials. For the samples blasted with the globular material, the friction coefficient is the lower the higher the blasting pressure is (Fig. 8a). This can be explained by the increasing fraction of areas covered by transferred blasting material with increasing pressure (see Fig. 5), which means that there is more softened material available to fill up surface irregularities (Fig. 9b). In contrast, for the samples blasted with the edged material, the friction coefficient is the higher the higher the blasting pressure is (Fig. 8b). This can be explained by the higher surface damage caused by blasting with the edged material compared to the globular one, fostering formation of wear debris acting as abrasive particles in the sliding contact. This interpretation is corroborated by the SEM micrograph of the rough and flaky wear track on α-Al_2O_3 dry-blasted with the edged material at 1.5 bar after ball-on-disc testing at 900 °C in Fig. 9c.

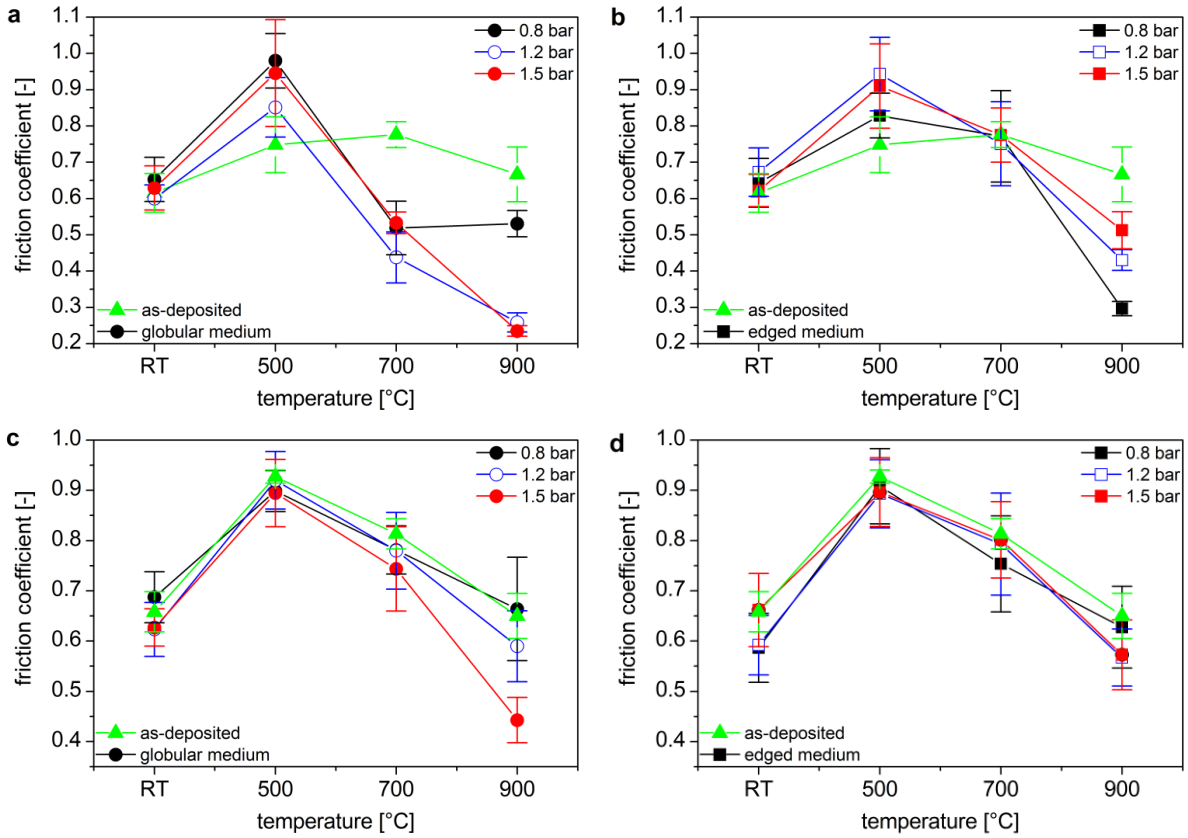

Fig. 8: Friction coefficient as a function of the ball-on-disc testing temperature. (a) α-Al_2O_3 dry-blasted with the globular and (b) with the edged material. (c) κ-Al_2O_3 dry-blasted with the globular and (d) with the edged material.

Similar to the as-deposited α-Al_2O_3, the friction coefficient of the as-deposited κ-Al_2O_3 also first increases with increasing testing temperature, due to promoted plastic deformation of the softened coating material [12], but decreases again above 700 °C. SEM investigations after the ball-on-disc test at 700 °C showed extended areas of TiO_2 coverage on the wear track surface (Fig. 9d), which are responsible for the decrease of the friction coefficient [17]. It has to be mentioned that the κ-Al_2O_3 shows already in the as-deposited state small fractions of α-Al_2O_3, as determined by XRD. Since the κ→α transformation occurs by a nucleation and growth process [4] and since there is already α-Al_2O_3 present, only minor thermal activation is required for further κ→α transformation. This transformation is accompanied by a volume shrinkage, leading to new secondary cracks, in addition to the already existing thermal cracks in CVD coatings [3, 4]. Since oxidation of the TiCN base-layer starts at temperatures in the range of 500 – 600 °C [18], this additional secondary crack network accelerates oxidation, leading to the TiO_2 found on the surface. At 900 °C, the friction coefficient is further decreased (see Fig. 8c), which is due to promoted diffusion of titanium through the κ-Al_2O_3 top-layer and formation of rutile [17].

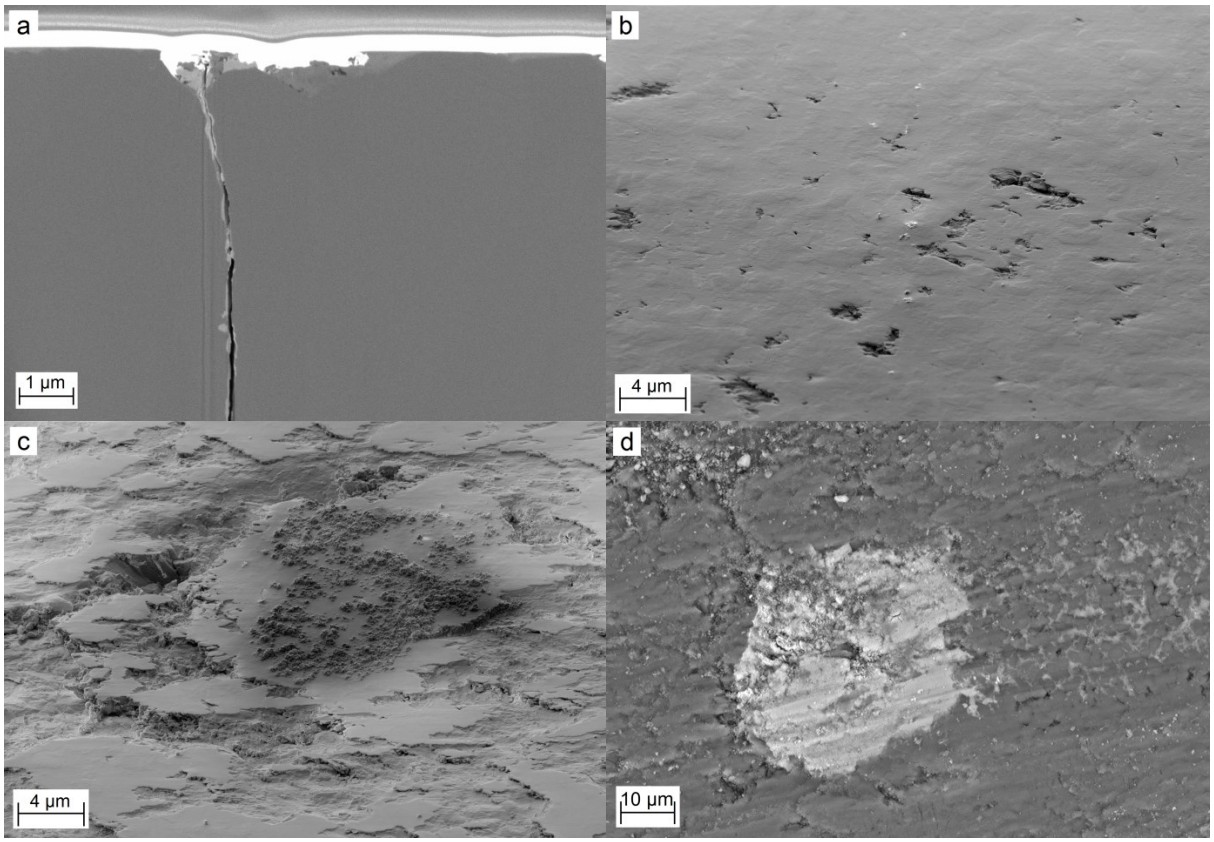

Fig. 9: (a) Back scattered SEM micrograph of a FIB cross-section trough the wear track of as-deposited α-Al_2O_3 after a ball-on-disc test at 900 °C showing a thermal crack with a bright TiO_2 rim. Secondary electron SEM micrographs of the wear tracks of (b) α-Al_2O_3 dry-blasted with the globular material at 1.5 bar and (c) α-Al_2O_3 dry-blasted with the edged material at 1.5 bar, after a ball-on-disc test at 900 °C. (d) Back scattered SEM micrograph of the wear track of as-deposited κ-Al_2O_3 after a ball-on-disc test at 700 °C, showing a large bright area consisting of TiO_2.

Similar to α-Al_2O_3, the friction coefficient of κ-Al_2O_3 dry-blasted with the globular material increases with increasing temperature, due to promoted plastic deformation of the transferred blasting material (Fig. 8c). Likewise, the decrease observed at temperatures of 700 and 900 °C can be related to softening of this transferred material. However, it should be noted that the drop at 700 °C is not as pronounced as it is for the α-Al_2O_3 dry-blasted with the globular material (compare Figs. 8a and c). This can be related to the increased surface roughness generated by dry-blasting of κ-Al_2O_3 (see Fig. 3b), which cannot easily be filled up by the softened transferred blasting material. The dependence of the friction coefficient on the blasting pressure at 900 °C is similar to the α-Al_2O_3 dry-blasted with the globular material. The higher the blasting pressure, the more transferred material is present on the coating surface, providing more material to soften and to be smeared over surface irregularities, resulting in lower friction coefficients. The friction behavior of κ-Al_2O_3 dry-blasted with the

edged material is comparable to that of the samples blasted with the globular material. Also TiO_2 could be found on the surface surrounding the thermal cracks after high-temperature ball-on-disc testing. However, differences have been found for the dependence of the friction coefficient on the blasting pressure for ball-on-disc testing at 900 °C compared to globular material. Blasting with the edged material causes already at low blasting pressures split-offs (see Fig. 4), leading to formation of wear debris, an increased surface roughness (see Fig. 3b) and consequently also higher friction coefficients.

4. Conclusion

α- and κ-Al_2O_3 coated cemented carbide samples were dry-blasted using globular as well as edged blasting materials and three different blasting pressures and the effects on surface topography, stresses, stress relaxation and friction behavior were explored. In general, a higher pressure resulted in higher compressive residual stresses. Vacuum annealing of the dry-blasted samples showed a complete relaxation of the introduced compressive stresses of α-Al_2O_3 dry-blasted with the globular material already at 500 °C. For α-Al_2O_3 dry-blasted using the edged material as well as for the κ-Al_2O_3, a complete stress relaxation could only be observed at 900 °C, independent of the blasting pressure. Ball-on-disc tests showed a decrease of the friction coefficient of the dry-blasted samples at ~700 °C, due to softening of the blasting material transferred onto the coating surface.

Acknowledgments

Financial support by the Austrian Federal Government (in particular from the Bundesministerium für Verkehr, Innovation und Technologie and the Bundesministerium für Wirtschaft, Familie und Jugend) and the Styrian Provincial Government, represented by Österreichische Forschungsförderungsgesellschaft mbH and by Steirische Wirtschaftsförderungsgesellschaft mbH, within the research activities of the K2 Competence Centre on “Integrated Research in Materials, Processing and Product Engineering”, operated by the Materials Center Leoben Forschung GmbH in the framework of the Austrian COMET Competence Centre Programme, is gratefully acknowledged.

References

[1] Ruppi, S.: Advances in chemically vapour deposited wear resistant coatings. J. Phys. IV France 11, 847-859 (2001)

[2] Osada, A., Nakamura, E., Homma, H., Hayahi, T., Oshika, T.: Wear mechanism of thermally transformed CVD Al_2O_3 layer. Int. J. Refract. Met. H. 24, 387-391 (2006)

[3] Skogsmo, J., Halvarsson, M., Vuorinen, S.: Microstructural study of the κ-Al_2O_3 → α-Al_2O_3 transformation in CVD κ-Al_2O_3. Surf. Coat. Technol. 54/55, 186-192 (1992)

[4] Vuorinen S., Karlsson, L.: Phase transformation in chemically vapor-deposited κ-alumina. Thin Solid Films 214, 132-143 (1992)

[5] Hochauer, D., Mitterer, C., Penoy, M., Michotte, C., Martinz, H.P., Kathrein, M.: Thermal stability of doped CVD κ-Al_2O_3 coatings. Surf. Coat. Technol. 204, 3713-3722 (2010)

[6] Hochauer, D., Mitterer, C., Penoy, M., Michotte, C., Martinz, H.P., Kathrein, M.: Titanium doped CVD alumina coatings. Surf. Coat. Technol. 203 350-356 (2008)

[7] Bouzakis, K.-D., Skordaris, G., Mirisidis, I., Michailidis, N., Mesomeris, G., Pavlidou, E., Erkens, G.: Cutting performance improvement through micro-blasting on well-adherent PVD films on cemented carbide inserts. Surf. Coat. Technol. 200 1879-1884 (2005)

[8] Bouzakis, K.-D., Gerardis, S., Skordaris, G., Katirtzoglou, G., Makrimallakis, S., Klocke, F., Bouzakis, E.: Effect of dry micro-blasting on PVD-film properties, cutting edge geometry and tool life in milling. Surf. Coat. Technol. 204, 1081-1086 (2009)

[9] Bouzakis, K.-D., Bouzakis, E., Skordaris, G., Makrimallakis, S., Tsouknidas, A., Katirtzoglou, G., Gerardis, S.: Effect of PVD films wet micro-blasted by various Al_2O_3 grain sizes on the wear behavior of coated tools. Surf. Coat. Technol. 205, S128-S132 (2011)

[10] Bouzakis, K.-D., Klocke, F., Skordaris, G., Bouzakis, E., Gerardis, S., Katirtzoglou, G., Makrimallakis, S.: Influence of dry micro-blasting grain quality on wear behavior of TiAlN coated tools. Wear 271, 783-791 (2011)

[11] Barbatti, C., Garcia, J., Pitonak, R., Pinto, H., Kostka, A., Di Prinzio, A., Staia, M.H., Pyzalla, A.R.: Influence of micro-blasting on the microstructure and residual stresses of CVD κ-Al_2O_3 coatings. Surf. Coat. Technol. 203, 3708-3717 (2009)

[12] Riedl, A., Schalk, N., Czettl, C., Sartory, B., Mitterer, C.: Tribological properties of Al_2O_3 hard coatings modified by mechanical blasting and polishing post-treatment. Wear 289, 9-16 (2012)

[13] Klaus, M., Genzel, Ch., Holzschuh, H.: Residual stress depth profiling in complex hard coating systems by X-ray diffraction. Thin Solid Films 517, 1172-1176 (2008)

[14] Klaus, M., Genzel, Ch.: Multilayer systems for cutting tools: On the relationship between coating design, surface processing, and residual stress. Adv. Eng. Mater. 8, 845-850 (2011)

[15] Czettl, C., Mitterer, C., Mühle, U., Rafaja, D., Puchner, S., Hutter, H., Penoy, M., Michotte, C., Kathrein, M.: CO addition in low-pressure chemical vapour deposition of medium temperature TiC_xN_{1-x} based hard coatings. Surf. Coat. Technol. 206, 1691-1697 (2011)

[16] Noyan, I.C., Cohen, J.B.: Residual Stress: Measurement by Diffraction and Interpretation, Springer, New York (1987)

[17] Hochauer, D., Mitterer, C., Penoy, M., Puchner, S., Michotte, C., Martinz, H.P., Hutter, H., Kathrein, M.: Carbon doped α-Al_2O_3 coatings grown by chemical vapor deposition. Surf. Coat. Technol. 206, 4771-4777 (2012)

[18] Wagner, J., Mitterer, C., Penoy, M., Michotte, C., Wallgram, W., Kathrein, M.: Structure and properties of CVD TiC_xN_{1-x} coatings. In: G. Kneringer, P. Roedhammer, H. Wildner, (eds.) Proceeding of the 16th International Plansee Seminar 2005, vol. 2, pp. 917-931 Plansee Holding AG, Reutte (2005).